Marlies Hofer, BSc.

Simulation of fluid dynamics in the gas processing unit of a mobile fuel cell system

Master's Thesis

submitted in fulfillment of the requirements for the degree of

Diplom-Ingenieur

Master's programme Mechanical Engineering

to

Graz University of Technology

Supervisor

Ao.Univ.-Prof. Dipl.-Ing. Dr.techn. Wolfgang Sanz
Institute of Thermal Turbomachinery and Machine Dynamics

Adviser

Dr. Robert Pöschl
Bernd Reiter, BSc.
AVL List GmbH

Graz, May 2018

Institute of Thermal Turbomachinery and Machine Dynamics
Head of Institute: Univ.-Prof. Dr.-Ing. Franz Heitmeir

Acknowledgments

First of all, I would like to thank DI Michael Reissig from the AVL List GmbH Fuel Cell departement for giving me the opportunity to work on such an interesting topic.
I would like to thank my academic supervisor Ao.Univ.-Prof. Dipl.-Ing. Dr.techn. Wolfgang Sanz for the constructive work, the time he took to read, correct and generally supervise this whole work.
Special thanks also goes to Dr. Robert Pöschl because of his hard effort, patience and help whether technical or organizational. He has a large share on success of this work.
A big thank goes to BSc Bernd Reiter who granted much time for supervising and to read and comment the whole performed work. He always had an ear for my questions. I want to mention also DI Joerg Mathe and DI Thomas Krauss from the Fuel Cell team who supported me in technical issues, especially BSc Markus Goll for providing his 1D simulation skills.
The practical part ot the thesis was performed in the DAC departement of the AVL List GmbH. Therefore, I would like to thank DI Andreas Ennemoser for giving me the chance to gain a deep insight into the CFD world.
DI Karl-Heinz Schaefer helped me a lot with geometry preparation, meshing and besides he had much time and patience with introducing me into FIRE, he always had good tips.
I thank DI Alexander Ruth for sharing his good understanding about theoretical background of CFD, especially relating to aftertreatment applications.
Furthermore, I would like to thank Dr.techn. Susanna Kattnig for her help regarding chemistrry issues, DI Sepp Steiner, DI Peter Cartellieri, Dr. Peter Priesching and Dr. Peter Sampl.
I would like to thank all my colleagues from the SOFC as well as from the DAC team for the kind and exciting time that I spent throughout this thesis.

Last but not least, thanks to my family for financial support as well as for the constant encouragement during the whole time of my studies.

Thank you all,

Marlies Hofer
05.04.2018

Affidavit
Eidesstattliche Erklärung

I declare that I have authored this thesis independently, that I have not used other than the declared sources/resources, and that I have explicitly indicated all material which has been quoted either literally or by content from the sources used. The text document uploaded to TUGRAZonline is identical to the present master's thesis.

Ich erkläre an Eides statt, dass ich die vorliegende Arbeit selbstständig verfasst, andere als die angegebenen Quellen/Hilfsmittel nicht benutzt, und die den benutzten Quellen wörtlich und inhaltlich entnommenen Stellen als solche kenntlich gemacht habe. Das in TUGRAZonline hochgeladene Textdokument ist mit der vorliegenden Masterarbeit identisch.

Graz, am 05.04.2018 Marlies Hofer

Abstract

Fuel cells are representing a promising technology in order to generate energy without being limited to the Carnot efficiency (as is the case for combustion engines), which results in high efficiencies. Especially high-temperature fuel cells like Solide Oxide Fuel Cells (SOFC) have the advantage of being operated with conventional hydrocarbon fuels like diesel or ethanol. SOFC systems are, for instance, applicable for power generation on board of heavy duty trucks or for range extension of electric vehicles. Such mobile SOFC systems, also called Auxiliary Power Units (APU), are therefore an important approach during the transition towards renewable and CO_2-free energy sources. The introduced liquid hydrocarbon fuel must be converted into a fuel cell compatible reformate gas before entering the fuel cell stack which is done by an upstream Gas Processing Unit (GPU).
This thesis deals with an analysis of a Gas Processing Unit for a SOFC system consisting of an evaporator and a reformer in flow path 1 and an oxidation catalyst for exhaust gas aftertreatment in flow path 2 by using Computational Fluid Dynamics (CFD) tools. The solid body between the two flow domains was included in the modelling, so that the heat transfer between the two flow paths could be investigated. After the multidomain calculation grid generation, some plausibility check calculations on a simplified model were performed. The gained insights were applied to the overall Gas Processing Unit model.
Energy balance calculations performed on the simplified model revealed a reasonable heat transfer also of the interface of porous media and solid body despite previous concerns, and some interesting effects could be observed. The results of the overall gas processing unit suggest possibilities for a geometry improvement. The high temperatures observed in measurements of the exhaust line indicate a possible pre-combustion already before the oxidation catalyst. This effect could be confirmed by the CFD results.

Kurzfassung

Brennstoffzellen stellen eine zukunftsträchtige Technologie zur Energiegewinnung dar, ohne dass der maximal ereichbare Wirkungsgrad auf den Carnot-Prozess limitiert ist. Mobile Bordstromaggregate (APUs) können unter anderem zur Reichweitenerhöhung von Elektrofahrzeugen oder zur Stromgenerierung an Bord von Lastkraftwagen dienen. Das SOFC-System kann auch mit konventionellen Brennstoffen betrieben werden und ist deshalb ein wichtiger Beitrag zu einer Zukunft mit erneuerbaren bzw. CO_2-freien Energiequellen. Die flüssigen Kohlenwasserstoffe müssen, bevor sie in den Brennstoffzellenstack gelangen, in einer Gasaufbereitungseinheit in ein brennstoffzellenkompatibles Gasgemisch umgewandelt werden. In dieser Arbeit wurde eine Gasaufbereitungseinheit eines SOFC Systems, bestehend aus einem Verdampfer und einem Reformer (Strömungspfad 1), sowie einem Oxidationskatalysator zur Abgasnachbehandlung (Strömungspfad 2) mit Hilfe einer dreidimensionalen Strömungssimulation analysiert. Der Festkörper zwischen den beiden betrachteten Strömungspfaden wurde mitmodelliert, um auch die Wärmeübertragung zwischen beiden Pfaden zu ermitteln. Nach der Netzgittergenerierung wurde eine Methodenevaluierung an einem vereinfachten Modell durchgeführt, wessen Erkenntnisse im Gesamtsystem Gasaufbereitungseinheit berücksichtigt wurden.
Die anfängliche Skepsis gegenüber der Fähigkeit, den Wärmeübergang zwischen porösen Medien und einem Festkörper zu simulieren, hat sich nicht bestätigt. Verschiedene Berechnungen und Energiebilanzen haben gezeigt, dass die Methode stimmig ist. Am Gesamtmodell wurden dann Verbesserungspotenziale ermittelt. Die in der Messung auffällig hohen Temperaturen im Abgasnachbehandlungspfad, bereits vor dem Oxidationskatalysator, weisen auf eine vorzeitige Verbrennung von Restbrennstoff und Oxidationsmittel hin, die durch die CFD Simulation bestätigt wurde.

Contents

Symbols and Abbreviations

Latin Symbols

a_{ik}	$-$	fitting coefficient
A	m^2	area
A	$-$	pre-exponential factor
b	$-$	temperature exponent
c_p	J/kg K	specific heat capacity at p = const.
$cpsi$	$1/inch^2$	cell density
C_{mp}	J/mol K	molar heat capacity at p = const.
C_μ	div	empirical constant
C_{poro}	m	turbulent length scale of porous media
d	mm	diameter
d_a	mm	outer diameter
d_h	mm	hydraulic diameter
d_i	mm	inner diameter
D	m^2/s	diffusion coefficient
E	J	activation energy
E_a	J	outer energy
$\Delta_R G_m$	J/mol	molar free energy of reaction

GSA	m^2/m^3	geometric surface area per catalyst volume
h	J/kg	specific enthalpy
H	J	enthalpy
H_m	J/mol	molar enthalpy
$\Delta_R H_m$	J/mol	molar enthalpy of reaction
I	A	current
k	m^2/s^2	turbulent kinetic energy
K_c	$-$	equilibrium constant in concentration units
k	$kmol/m^3s$	reaction rate constant
l	m,mm	length
m_{Cat}	g/cm^3	catalyst loading
$\dot{m}$	kg/s	massflow
M	g/mol	molecular weight
n	-	number of electrons
n_{cells}	-	number of cells
$\dot{n}$	(k)mol/s	mole flow
OFA	%	open frontal area
O/C	$-$	oxygen to carbon ratio
Pr	-	Prandtl number
Δp	bar, Pa	pressure drop
p_k	bar, Pa	partial pressure of component k
P_{el}	W	electrical power
$\dot{q}$	W/m^2	heat flux density
Q	J	heat

$\dot{Q}$	W	heat flux
Re	-	Reynolds number
r_{rec}	-	recirculation rate
$\dot{r}$	kmol/m³s	reaction rate
$\vec{r}$	-	location vector
S_{c}	-	Schmidt number
S_{m}	J/mol K	molar entropy
S/C	$-$	steam to carbon ratio
t	°C, K	temperature
Δt	s	timestep
T	K	temperature
t_{w}	mm, mil	wall thickness
u_τ	m/s	friction velocity
u^+	-	dimensionless near wall velocity
U_{c}	V	cell voltage
U_{H}	V	thermoneutral voltage
U_{N}	V	cell voltage according Nernst equation
U	J	inner energy
U	V	voltage
V	m³	volume
V_{gas}	m³	gaseous volume
$\dot{V}$	Nl/h	volume flow
V_{m}	m³/kmol	mole volume
w_i	m/s	local velocity in porous medium

W_{el}	J	electrical energy
x	m	coordinate
y	m	coordinate
y^+	-	dimensionless wall distance
z	m	coordinate

Greek Symbols

α	$W/m^2\,K$	heat transfer coefficient
α_i	$1/m^2$	viscous loss coefficient
γ	-	uniformity index
Γ	m^2/s	diffusion coefficient
δ	mm	boundary layer thickness
δ_{wc}	mm	washcoat thickness
ε	$-$	porosity
ε_t	$-$	dissipation rate
ζ_i	$1/m$	inertial loss coefficient
η	$-$	efficiency
η_{au}	-	air utilization
η_{fu}	-	fuel utilization
η_{th}	$-$	thermal efficiency
η_C	$-$	cell efficiency
λ	$W/m\,K$	thermal conductivity
λ_l	$-$	laminar tube friction coefficient
λ_t	$-$	turbulent tube friction coefficient
μ	Ns/m^2	dynamic viscosity
μ_k	kg/kg	mass fraction of component k
μ_t	m^2/s	turbulent viscosity
ν_k	mol/mol	mole fraction of component k
ν_{st_k}	$-$	stochiometric coefficient of component k
ρ	kg/m^3	density
τ	N/m^2	shear stress
Θ	-	centricity index
ϕ	-	arbitrary quantity

φ	-	shape factor

Constants

F	96458	C/mol	Faraday constant
κ	0.41	–	Von Karman constant

Abbreviations

0D	zero-dimensional	FAME^{TM}M	AVL polymesher
1D	one-dimensional	GPU	Gas Processing Unit
3D	three-dimensional	HEX	Heat Exchanger
1.4767	X8CrAl20-5-21	H_2	hydrogen
1.4841	X15CrNiSi25-21	H_2O	water
AFC	Akaline Fuel Cell	HO_2	hydroperoxyl
Al_2O_3	Aluminium Oxide	LSM	Lanthanum Strontium
APU	Auxiliary Power Unit		Manganite
ATR	Autothermal Reforming	MCFC	Molten Carbonate Fuel
AVL	Anstalt für		Cell
	Verbrennungsmotoren	Mg2Al4Si5O18	Cordierite
	List GmbH	NASA	National Aeronautics
ACCI	AVL Code Coupling		and Space
	Interface		Administration
BoP	Balance of Plant	Ni	Nickel
CAD	Computer-aided Design	N_2	nitrogen
		O_2	oxygen
CFD	Computational Fluid	OSR	Oxidative Steam
	Dynamics		Reforming
CH_4	methane	OH	hydroxyl
CO	carbon monoxide	PAFC	Phosphoric Acid Fuel
CO_2	carbon dioxide		Cell
CPOX	Catalytic Partial	PEM	Proton Exchange
	Oxidation		Membrane
FIRE^{TM}	AVL CFD Simulation	Pd	Palladium
	program	Pt	Platinum

Rh	Rhodium	SR	Steam Reforming
SOFC	Solide Oxide Fuel Cell	WGS	Water Gas Shift
STL	Standard Tessellation Language	YSZ	Yttrium stabilized zirconium dioxide

Indices

r	backwards	k	index of chemical species
c	center		
f	forwards	l	cell index
i	index of direction (x, y, z)	ref	reference
		t	turbulent
j	index of chemical reaction	w	wall

1 Introduction

1.1 Fuel Cell Technology

Fuel Cells are continuously operating batteries which are able to convert the chemical energy of a fuel directly into electrical energy without being limited to the lower efficiency of the Carnot process which governs in case of combustion engines [21]. The generation of electrical energy results from a fuel, such as hydrogen, and an oxidant, such as air [29].
The following Table 1.1 shows an overview of the different fuel cell types including the Solide Oxide Fuel Cell (SOFC) investigated in this work.

Table 1.1: Types of fuel cells[10], [12]

Type	Electrolyte	Operating Temperature	Fuel	Charge Carrier	Efficiency cell/system
PEM	proton exchange membrane	40-80°C	H_2	H^+	50-70/30-50%
AFC	potassium hydroxide	65-220°C	H_2	OH^-	60-70/60%
PAFC	phosphoric acid	205°C	H_2	H^+	55/40%
MCFC	molten carbonate	650°C	H_2, CO, CH_4	CO_3^-	55/40%
SOFC	solide oxide ceramics	750-1000°C	H_2, CO, CH_4	O^-	60-65/55-60%

Each fuel cell type is used in different application fields. The Proton Exchange Membrane (PEM) fuel cell is mainly used as power unit for transport applications because of its low operating temperature and transient response behaviour. PEM fuel cells require very pure hydrogen fuel due to the fact that even a small quantity of CO can cause a cell poisoning [30].
SOFCs were developed for stationary and mobile applications and, at lower power

levels, for portable generators. A big advantange of the SOFC is that it can be operated by a wide range of fuels using internal reforming directly at the anode of the fuel cell. The main reaction occuring at the anode is with hydrogen fuel, but depending on the anode material, also other fuels can directly react, i.e. carbon monoxide (CO) on Ni/YSZ materials and methane (CH_4) on Ceria or others [30].

1.2 SOFC Auxiliary Power Unit

In the mobile sector, the SOFC Auxiliary Power Unit (APU) has been developed for the purpose of producing electrical power on board of passenger cars and trucks. The power results from electrochemical reactions which occur in the electrolyte of the fuel cell under supply of fuel to the anode and of an oxidant to the cathode.
Especially on board of heavy duty trucks, a SOFC APU has many advantages. Thereby it is possible to decouple the stationary mode from the driving mode in a way that the SOFC APU is able to deliver the electrical power for all other purposes besides driving. Simultaneously, the thermal capacity, which is set free from a high temperature fuel cell like an SOFC, can be used for heating the driver cabin. Diesel fuel can directly be diverted from the fuel tank and is therefully well suited as fuel for the APU. Besides that, with regard to the current small hydrogen infrastructure it seems also a good solution to extend the range of an electrical vehicle by adding an APU to the electric drive train which is fuelled by, for instance, a bio fuel like bio ethanol.

1.3 Gas processing

The more efficient the introduced liquid fuel from the fuel tank can be converted into a SOFC compatible gas mixture, the lower are fuel consumption and CO_2 emmisions. The goal is to increase this efficiency with regard to economic and environmental reasons.
A widespread method to convert the hydrocarbon fuel into a hydrogen rich gas mixture is to use a catalytic reformer which operates best in a certain temperature range which depends on the catalytic material, mostly around a temperature of 500 to 800°C [10]. Reforming can take place in various forms, whether this can

be via endothermic or exothermic reactions or a combination without mentionable external heat exchange. In any case, the heat which is required to reach the operation temperature of the reformer can be taken from the hot exhaust gas which the fuel cell emitts. Therefore, an efficient thermal management has to be ensured for optimisation of the process.

1.4 AVL SOFC APU program

The company AVL (Anstalt für Verbrennungsmotoren List GmbH) is involved in fuel cell development since 2002. The AVL Fuel Cell department is divided into separate skill teams for PEM and SOFC. A part of the AVL SOFC team deals with SOFC APUs and within this framework, already several generations of a power unit which have an electrical power output from 3kW up to 5 kW, running on different fuels like ethanol or diesel, were developed. At the test bench there were carried out component tests as well as full APU system tests and research as well as customer projects were performed successfully.
The GPU, which is part of the SOFC APU, developed by AVL, contains a fuel evaporator, a catalytic reformer and an off-gas burner to burn the fuel cell exhaust gases. The fuel cell stack module is fed with the gas mixture produced in the gas processing unit and provides thermal energy which is guided back into the exhaust path of the GPU.

1.5 Analysis Objective

This thesis deals with a flow and thermal analysis of the GPU from AVL. The objective was to analyze the existing design and to point out where there is potential for improvement.
The simulation was performed with APU system test results of a typical 3kW operating point and by using three-dimensional (3D) CFD with the simulation program FIRE^{TM}, a software developed by AVL based on the Finite Volume method. CFD methods provide the possibility to visualize spatially resolved flow characterisics by solving physical and chemical equations.

The thesis includes

- an analysis of APU test results,
- calculation of required boundary conditions for the CFD simulation,
- the generation of a calculation grid and
- the evaluation of the analysis results.

The CFD method used to analyze the GPU was proved by a plausibility study which was performed on a simplified model.

2 Basics of SOFC Fuel Cells and Gas Processing

2.1 Solide Oxide Fuel Cells

2.1.1 Principle

A SOFC is a high temperature fuel cell whose operating temperature extends from 750°C to 1000°C [12]. A fuel cell consists of two electrodes, namely anode and cathode, and an electrolyte being in between. In a SOFC the material used for the electrolyte is usually made out of a solid ceramic like Yttrium stabilized zirconium dioxide (YSZ). Due to its special material properties, YSZ is capable to conduct oxide ions at temperatures above 750°C. At the same time it is impermeable to gas and electrons [12].
The working principle of an SOFC is illustrated in Figure 2.1 and the occuring chemical processes are listed in Table 2.1.

Table 2.1: Chemical reactions in fuel cells [10]

Type	**Chemical Equation**	**Process**
anode reaction	$H_2 + O^{2-} \rightarrow H_2O + 2e^-$ $(CO + O^{2-} \rightarrow CO_2 + 2e^-)$	oxidation/ release of electrons
cathode reaction	$\frac{1}{2}O_2 + 2e^- \rightarrow O^{2-}$	reduction/ acceptance of electrons
overall reaction	$H_2 + \frac{1}{2}O_2 \rightarrow H_2O$ $(CO + \frac{1}{2}O_2 \rightarrow CO_2)$	redox reaction

A SOFC can be operated with fuels like hydrogen (H_2), CO but also CH_4. The fuel

is led to the anode for which a ceramic-metallic cermet material is used, consisting of Nickel (Ni) in order to conduct electrons and YSZ to conduct oxide ions [30]. The cathode side of the fuel cell is fed with an oxidant such as air which will be reduced to oxygen ions. The cathode consists of Lanthanum Strontium Manganite (LSM) which is electron and ion conducting and has the task to catalyze the oxygen reaction [19]. The oxygen ions generated at the cathode then migrate through the electrolyte to the anode side where the fuel will be oxidized and forms water vapour (and CO_2 in case of carbon-containing fuel). The electrons, which are released at the anode during this electrochemical reaction, move along an electric circuit to the cathode, where the process starts from the beginning [33]. Fuel or oxidant has to be applied to the whole electrode in order to prevent losses or cell damages. Therefore, some unused fuel and oxidant remain in the exhaust gas of the fuel cell, which will be removed together with the products of the chemical reactions [21].

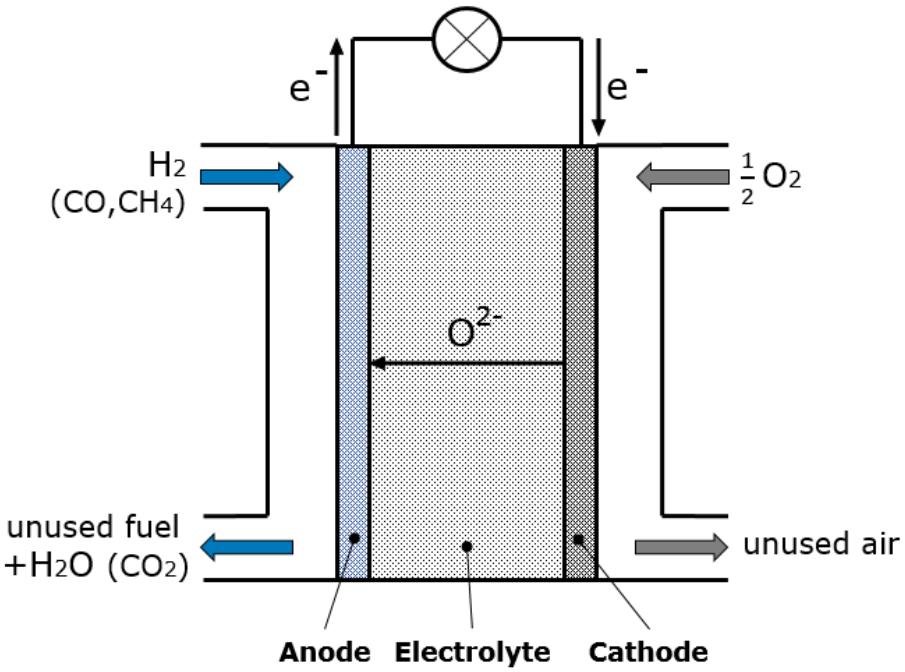

Figure 2.1: Working Principle of a Solide Oxide Fuel Cell [10]

2.1.2 Parameters

Cell voltage

To specify a fuel cell, some characteristic parameters like thermoneutral voltage (U_H), electrical energy (W_{el}) and efficiency (η) are used, describing electrochemical conditions which depend on the molar free energy of reaction ($\Delta_R G_m$) and the molar enthalpy of reaction ($\Delta_R H_m$) [12].
The maximum electrical work W_{el} delivered by a fuel cell is equivalent to the change of the molar free energy of reaction ($\Delta_R G_m$) which correlates to the product of the Faraday constant (F), the number of electrons (n) participating in the reaction and the cell voltage (U_c), as shown in equation 2.1 [12].

$$W_{el} = \Delta_R G_m(T,\, p) = -n \cdot F \cdot U_c \tag{2.1}$$

The theoretically maximum voltage of a fuel cell is U_H, described by following formula 2.2 which contains the molar enthalpy of reaction $\Delta_R H_m$ at standard conditions.

$$U_H^0 = -\frac{\Delta_R H_m^0(T_0,\, p_0)}{n \cdot F} \tag{2.2}$$

Values for standard conditions ($T_0 = 25°C$, $p_0 = 1atm$) of a fuel cell operated with fuel H_2 and product liquid H_2O are listed in Table 2.2.

Table 2.2: Standard conditions for water production according to [12]

p_0	t_0	$\Delta_R H_m^0$	$\Delta_R G_m^0$	$\Delta_R S_m^0$
1 bar	25 °C	285 840 J/mol	237 144 J/mol	163,326 J/mol K

The same applies for U_c by accessing $\Delta_R G_m$ (equation 2.3).

$$U_c^0 = -\frac{\Delta_R G_m^0(T_0,\, p_0)}{n \cdot F} \tag{2.3}$$

The number of electrons involved at reaction $H_2 + \frac{1}{2}O_2 \rightarrow H_2O$ is 2, this leads to a cell voltage of 1,23V. Because of such low cell voltages, fuel cells will be connected serially and bundled to fuel cell stacks to gain an as high as possible voltage which is related to a higher electrical power output [12].
Is the condition in which the cell is operating not a standard condition, the actual

molar enthalpy of reaction at standard conditions has to be replaced by the molar enthalpy of reaction with the consequence that the value of the cell voltage can only achieve the cell voltage according Nernst equation (U_N). The Nernst equation considers the temperature (T) and, under the assumption of ideal gas, the partial pressure of component k (p_k) and the stochiometric coefficient of component k (ν_{st_k}) of all components involved (see equation 2.4) [12].

$$U_N = -\frac{\Delta_R G_m(T,\, p)}{2 \cdot F} = U_c^0 - \frac{R_m T}{n \cdot F} \cdot ln \prod_k \left(\frac{p_k}{p^0}\right)^{\nu_{st_k}} \tag{2.4}$$

For a fuel cell fuelled with hydrogen it can be written (equation 2.5):

$$U_N = U_c^0 - \frac{R_m T}{n \cdot F} \cdot ln \frac{p_{H_2O}}{p_{H_2} \sqrt{p_{O_2}}} \tag{2.5}$$

This cell voltage according Nernst equation U_N displays therefore the maximum achievable cell voltage at real conditions (not standard conditions) which is shown in Figure 2.2 [12].

Actual performance

In addition, in order to determine the real U_c that actually occurs in a fuel cell, there have to be considered several irreversible losses caused by the operation mode of the fuel cell. In sum, this total loss is decribed by the cell efficiency (η_C) in equation 2.6 [12].

$$\eta_c = \frac{U_c}{U_H^0} \tag{2.6}$$

The losses happening in a fuel cell during operation are listed below. The influence parameters of these losses are shown in the *U-I* curve in Figure2.2.

- activation related losses
- resistance losses (also: ohmic losses)
- gas transport losses

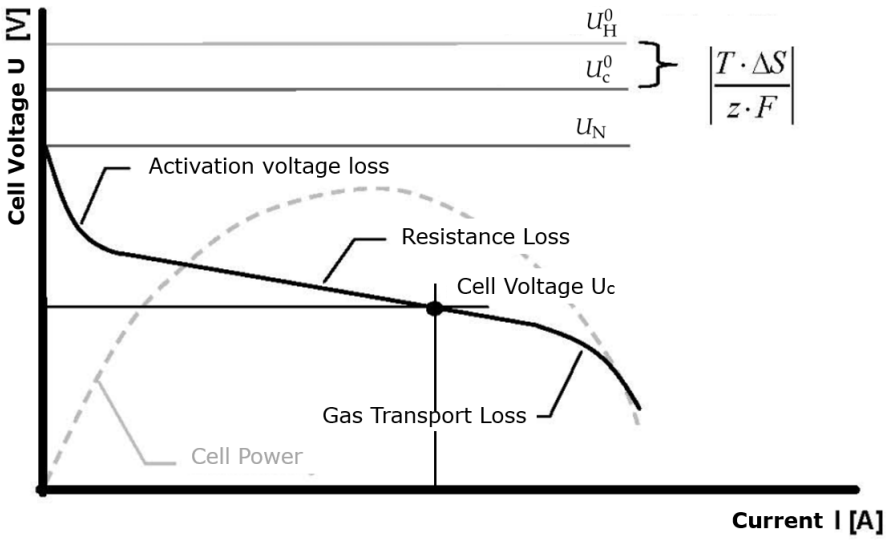

Figure 2.2: U-I-curve of a fuel cell [12]

Activation voltage losses: The activation voltage losses which are seen in the *U-I* characteristic curve at low current, are caused by the activation energy of the electrochemical reactions at the electrode and electrolyte interface. In SOFCs, these losses are negligible because of the high operation temperatures which are providing the necessary energy for activation [13].

Resistance losses: These losses show a linear behaviour in dependence of the electric current. They are governed by an ionic resistance in electrodes and electrolyte, by electronic resistances of electrodes and interconnectors and by contact resistances [12].

Gas transport losses: These are determined by too slow supply of gas to the fuel cell inlet and too slow removal of products at fuel fell outlet, which increasingly occurs at high currents [12].

Fuel utilization

The fuel utilization (η_{fu}) is the ratio of the fuel flow at fuel cell outlet to the fuel flow at fuel cell inlet. It shows how much of the supplied fuel $\dot{n}_{\mathrm{anode,in}}$ will be converted

during the electrochemical reaction into electrical current. Because of a relation between η_{fu} and gas composition, it has also influence on U_{N} and, therefore, the efficiency of the fuel cell.

$$\eta_{\mathrm{fu}} = 1 - \frac{\dot{m}_{\mathrm{fuel,anode,out}}}{\dot{m}_{\mathrm{fuel,anode,in}}} \tag{2.7}$$

For the fuel utilization limit values are given by the stack supplier. At low η_{fu}, U_{N} becomes higher but not η_{C}. This is because of the fact that then a higher fuel ratio would leave the fuel cell unused and would not be converted into electrical energy. Above η_{fu} limits the fuel cell should not be operated because an oxidation at the anode due to fuel empowerishment can happen . The empowerishment leads then to an increase of the gas transport loss and to a high voltage drop. Common values for η_{fu} are from 80 to 85% [33].

2.2 SOFC System

To increase the power output of a fuel cell, the cells were arranged sequentially to a fuel cell stack along with so called interconnectors as the binding element. Regarding SOFCs, the cell arrangement can be planar or tubular. In addition to that, practical fuel cell systems require also a Balance of Plant (BoP) which contains components for fuel preparation, air supply, thermal management, water management and electric power conditioning, in order to allow the operation with conventional fuels like hydrocarbons. Except when the system is fed with pure fuels like pure hydrogen, some fuel preparation is required, involving the removal of fuel impurities like sulfur, thermal conditioning and fuel processing such as reforming to gain a hydrogen rich anode feed gas [10]. The air supply includes components like air filters and air blowers.

2.2.1 Structure and Components

Figure 2.3 shows the components and their interactions of a typical APU system with anode off-gas recirculation and CH_4 fuel.
The system consists of three main paths, namely

- the anode line,

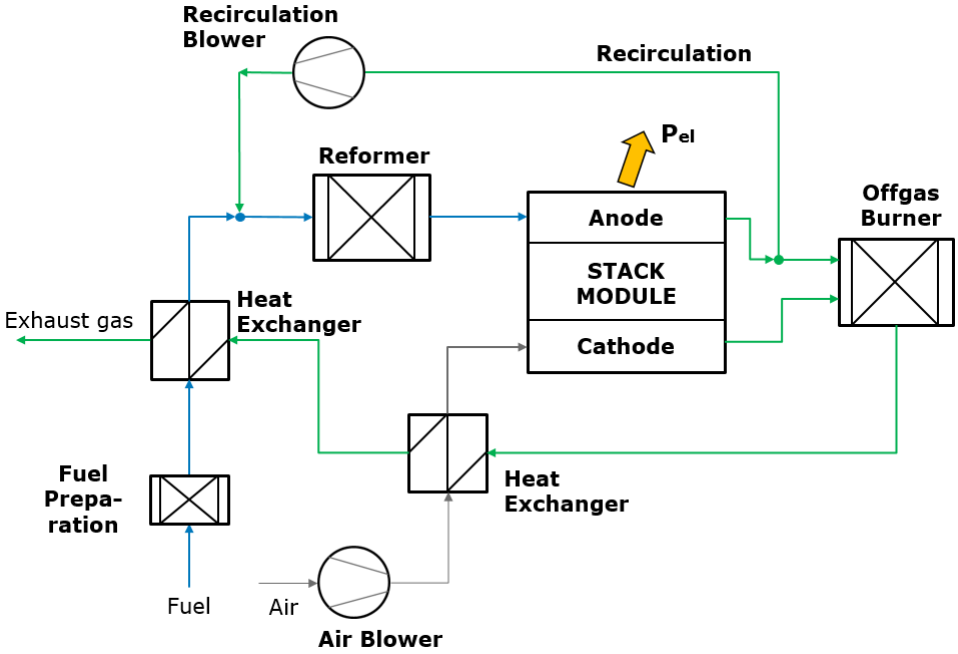

Figure 2.3: Schematic layout of a SOFC system [33]

- the cathode line and
- the exhaust line, where anode and cathode exhaust gases are merged.

The anode line contains the components for fuel processing like the reformer. Fuel from the fuel tank is led to the fuel preparation reactor (removal of harmful species for fuel cell and reformer) and afterwards led to a reformer reactor, typically a catalyst where catalytic reforming reactions occur with the goal to get a hydrogen-rich gas for the anode electrode of the fuel cell. Before reaching the reformer, a part of recirculated anode off-gas from the fuel cell stack is added.
At the cathode line, an air blower provides ambient air from outside for the cathode electrode of the fuel cell stack. To reach the cathode at process temperature level, the air is heated up by a heat exchanger that is fed with hot exhaust gas from the anode and cathode side of the fuel cell stack.
After the reduction and oxidation process in the fuel cell stack, the exhaust gases of the fuel cell were led to the off-gas burner where the exhaust gas aftertreatment occurs to ensure an as clean as possible exhaust gas. It is common to use the heat released by the off-gas burner in order to heat up other components like the re-

former.
A part of the anode off-gas will be extracted prior to the burner and will be recirculated which has the effect to support the heatup of the fuel and to reduce soot formation. Unused fuel components like CO and H_2 in the anode off-gas can increase the electrical efficiency and introduced water vapour supports steam reforming. The anode off-gas recirculation is technically solved by a recirculation blower.

2.2.2 Performance Characteristics of SOFC Systems

Electrical efficiency

At the expense of the introduced fuel energy, the fuel cell stack is able to produce electrical power (P_{el}) (2.8).

$$\eta_{el} = \frac{P_{el}}{\dot{m}_{fuel} \cdot H_u} \tag{2.8}$$

System efficiency

In a fuel cell system the required blower for air supply and off-gas recirculation as well as voltage inverter need power which results in an efficiency decrease. For comparing fuel cell systems to each other, the system efficiency η_{system} can be written as in equation 2.9 [33]. Fuel cells can reach a cell efficiency around 60%, efficiencies for a cell stack can be values up to 50% and system efficiencies around 40% [12].

$$\eta_{system} = \frac{P_{el} - P_{bl} - P_{inv}}{\dot{m}_{fuel} \cdot H_u} \tag{2.9}$$

Thermal efficiency

The heat produced out of of the introduced fuel energy leads to the thermal efficiency (η_{th}), shown in equation 2.10 [33].

$$\eta_{th} = \frac{\dot{Q}}{\dot{m}_{fuel} \cdot H_u} \tag{2.10}$$

Steam to carbon ratio

The prescription of a minimum steam to carbon ratio (S/C) in the process gas leads to an inhibitation of carbon deposition on catalytic surfaces and the anode of the fuel cell. The higher the S/C, the more H_2 can be gained out of the steam reformer [19].

$$\frac{S}{C} = \frac{\dot{n}_{H_2O}}{\dot{n}_C} \tag{2.11}$$

Oxygen to carbon ratio

The minimum oxygen to carbon ratio (O/C) allowed for the Catalytic Partial Oxidation (CPOX) reforming process is 1 to avoid carbon deposition. This leads to a high heat release resulting in high temperatures. The steam reformer allows lower O/C [10]. As a result of the transport of oxygen ions from cathode to anode, the O/C at the anode increases. Therefore, the critical component for carbon deposition is the reformer catalyst. It can cause an increase of the pressure drop due to blocking the pores as well as catalyst deactivation [33]. The relations for O/C can be seen in equation 2.12.

$$\frac{O}{C} = \frac{\dot{n}_O}{\dot{n}_C} \tag{2.12}$$

Air utilization

In analogy to the fuel utilization for the fuel there exists an air utilization regarding the air supply at the cathode (equation 2.13). In the cell of a SOFC consumption of oxygen occurs during the electrochemical reaction.

$$\eta_{\text{au}} = 1 - \frac{\dot{m}_{\text{air,cathode,out}}}{\dot{m}_{\text{air,cathode,in}}} \tag{2.13}$$

The bigger the value of air utilization (η_{au}) is, the less cooling performance of the stack takes place. A low value of η_{au} results in a high cooling performance of the stack and therefore in a lower electrical efficiency [33].

Recirculation rate

In a SOFC system, water is needed for the steam reforming process and for the prevention of soot, especially in the reformer catalyst and in the anode line of the fuel

cell stack. By recirculation of H_2O rich anode exhaust gas, a water management system can be avoided. Therefore, in many SOFC systems containing steam reformers and/or running on hydrocarbon fuels, there are recirculation blowers to bring in again a part of the anode exhaust gas. The recirculation rate (r_{rec}) represents the ratio of reintroduced anode gas into the reformer line and overall anode off-gas as shown in equation 2.14 [33].

$$r_{\text{rec}} = \frac{\dot{n}_{\text{rec}}}{\dot{n}_{\text{fuel,anode,out}}} \tag{2.14}$$

A high value of r_{rec} implies a higher fuel utilization but also a higher dilution of the fuel.

Uniformity Index

The uniformity index (γ) is an indicator in order to evaluate the flow field of a porous medium like a catalyst and it is directly linked to its efficiency. The more uniform the distribution at the inlet is, the better is the species conversion and the heatup and the lower the pressure losses and temperature gradients. The uniformity index can be written as in equation 2.15 which contains an arbitrary quantity (ϕ) like mass flow or velocity, the cross section area (A) wherein indizes l represents the cell index and A the overall cross section area.

$$\gamma = 1 - \frac{1}{2} \sum_{l=1}^{n} \frac{A_l |\overline{\phi_l} - \overline{\phi}|}{\overline{\phi} \cdot A} \tag{2.15}$$

In other words, γ is the deviation from the mean value and ranges from 0 to 1 wherein 1 stands for the ideal case of complete homogenuous flow. AVLs recommendation for γ in the field of catalytic converters is of at least 0.95 for optimised flow [17].

Centricity Index

In addition to the uniformity index, the centricity index (Θ) of a flow is a value for indicating the offset of a flow's barycenter from the center of gravity of, for instance, the catalyst cross section. The value of Θ ranges from 0 to 1 and should

be above 0.85 according to AVL guidelines to grant reasonable flow conditions without remarkable deficits. Equation 2.16 shows the relations containing the cell (index l) and total massflow $\dot{m}$, the cell and total cross section area and the location vector ($\vec{r}$) of a specific cell l. A value of 1 for Θ indicates a completely centered flow [17].

$$\Theta = 1 - \left| \sum_{l=1}^{n} \vec{r}_l \frac{\dot{m}_l}{\dot{m}} - \sum_{l=1}^{n} \vec{r}_i \frac{A_l}{A} \right| \cdot \sqrt{\frac{\pi}{A}} \tag{2.16}$$

Tangential pressure gradient

Due to shear forces resulting out of a tangential flow towards the catalyst inlet, the catalyst channel walls can be overstressed and the walls could collapse. To characterize the risk for the catalyst, there is another value introduced for evaluating the flow into the catalytic converter. The tangential pressure gradient grad(p) is defined as in equation 2.17.

$$grad(p) = \frac{\partial p}{\partial x}\vec{x} + \frac{\partial p}{\partial y}\vec{y} + \frac{\partial p}{\partial z}\vec{z} \tag{2.17}$$

$\vec{x}$, $\vec{y}$ and $\vec{z}$ represent the unit vectors along the respective coordinate axes. Maximum acceptable tangential pressure gradients are 25 bar/m for ceramic substrates and 15 bar/m for metal substrates [17].

2.3 Gas Processing

To ensure that the APU can run with commonly available fuels like diesel or ethanol, a fuel processor is needed which converts the liquid fuel into gas, containing mainly the compounds required for the fuel cell to produce electricity. The fuel which is led into the SOFC stack should be a hydrogen rich gas stream. The major challenge of the GPU is to ensure a complete evaporation of the liquid hydrocarbons, providing a homogenuous gas mixture of evaporated fuel, air and, in most applications, recirculated gas at reformer inlet to make sure a stable operation within the reformer [29].

2.3.1 Fuel Evaporation and Mixing

The fuel evaporation should be completed before reaching the reformer catalyst. Liquid fuel drops on the catalytic surface can lead immediately to undesired coke formation as well as fluctuating S/C and O/C ratios, which can lead to an unstable reformer operation and therefore an unstable hydrogen output. The fuel should be atomized very finely and desired temperatures have to be provided for the endothermic evaporation process. The homogenity of the gas mixture upstream the reformer has to be ensured also in regard to avoid zones with high O/C ratios that could cause an autoignition. The evaporation of longer chained hydrocarbons like gasoline or diesel needs high temperatures, for example, diesel requires vaporization temperatures from 350°C to 400°C [10]. In case of Steam Reforming (SR) and Oxidative Steam Reforming (OSR), it has to be ensured that the introduced water is evaporated, too [29].

2.3.2 Catalytic Reforming

Depending on the reforming type, the fuel and catalyst characteristics, catalytic system temperatures from 500 to 800°C are common. Without catalytic components, higher temperatures and/or pressures would be required for the reforming process which could lead to a formation of unwanted oxides of nitrogen [29] [10]. There are three main methods of catalytic reforming which are

- Steam Reforming (SR),
- Catalytic Partial Oxidation (CPOX) and
- Oxidative Steam Reforming (OSR).

Steam Reforming produces the highest concentration of hydrogen, Catalytic Partial Oxidation has a fast response and Oxidative Steam Reforming represents a combination.

Steam Reforming (SR)

Steam Reforming is the reaction of hydrocarbons with steam to form a mixture of hydrogen and CO which is reversible for methane and irreversible for higher

hydrocarbons. In 2.18 the chemical reaction is shown.

$$C_nH_m + nH_2O \rightleftharpoons (n + \frac{m}{2})H_2 + nCO; \quad \Delta_R H^0_m > 0 \tag{2.18}$$

The SR reaction is endothermic which means that the reformer requires a heat input from outside to operate efficiently [29]. Besides that, the reaction is slow and this means, a larger catalyst volume is needed. Benefits of the endothermic SR are a high hydrogen yield and a higher efficiency. In contrast to this, a complex thermal management is required to gain the necessary heat for the endothermic reaction. Typically, steam to carbon ratios from 2 to 3 are used in steam reformers, depending on the operating conditions [21]. Typical S/C ratios for diesel are between 3.6 and 4.0 at temperatures around 973 K to obtain good conversions [29].
SR conditions favor the fast and close to equilibrium water gas shift as an important side reaction. Other side reactions like methanation and carbon dioxide reforming are possible. SR of hydrocarbons, especially methane, is well established in industry. SR can occur with or without a catalyst, in most applications a catalyst is implemented to enhance reaction rates at lower temperatures. When reforming higher chains of hydrocarbons like gasoline or diesel, it is common to use Rhodium (Rh) as noble material for SR processes because Rh has, different to Ni, good characteristics regarding coking resistance and conversion [29].

Catalytic Partial Oxidation (CPOX)

The Catalytic Partial Oxidation (CPOX) represents an alternative to the SR in order to produce hydrogen rich gas out of hydrocarbons. Here, hydrocarbons are reacting with O_2 which is added substochiometric to avoid a total oxidation (equation 2.19).

$$C_nH_m + \frac{n}{2}O_2 \rightleftharpoons (\frac{m}{2})H_2 + nCO; \quad \Delta_R H^0_m < 0 \tag{2.19}$$

During the strongly exothermic reaction, a gas mixture is produced, containing H_2 and CO. Similar to SR, partial oxidation can be carried out without or with catalyst. Without catalyst, a much higher temperature (about 1400°C) is required because of the higher activation energy. If using a catalyst, it is possible to raise the selectivity of reaction [29] [10].
CPOX has the advantage of rapid reforming kinetics (faster than SR reaction) and

quick light-off characteristics followed by a quick response to transients. There is no need to feed water as in SR or OSR reactors, they are smaller and can be easier applied to on-board reforming systems. Because of the exothermic nature of the CPOX, there is no need of external heat supply. However, CPOX has to challenge with problems regarding catalyst deactivation caused by high temperature sintering, coke formation, poisoning from sulfur and other contaminants. The reactions which occur in a CPOX reformer are complex, the overall reaction is shown in equation 2.19, but there can take place several side reactions, where the most significant one is the water gas shift. Typical operating conditions are temperatures from 700 to 1000°C and a O/C about 1.2 [29]. Temperature-dependent and O/C dependent conversions for CPOX of n-tetradecane can be seen in Figure 2.4.

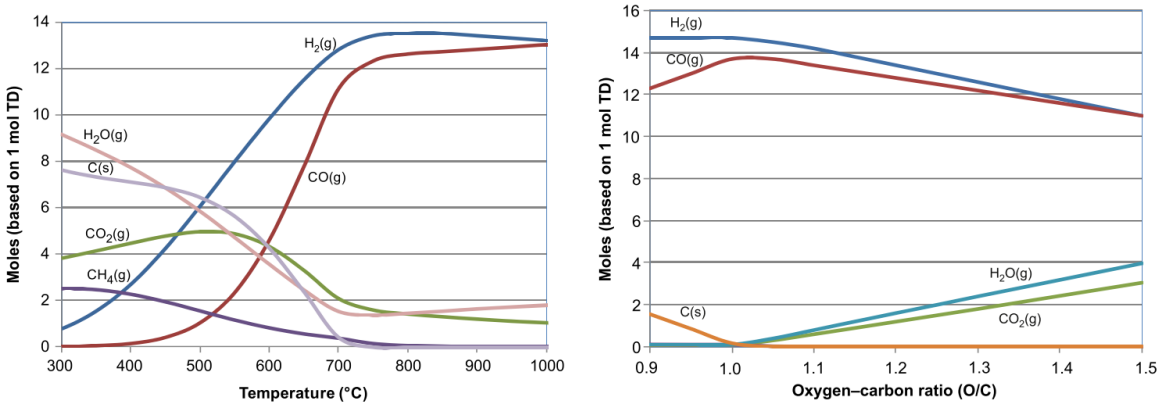

Figure 2.4: Equilibrium product distribution for CPOX of n-tetradecane (TD, similar to diesel) depending on temperature (left) and O/C ratio (right)[29]

Oxidative Steam Reforming (OSR)

A third reforming option is Oxidative Steam Reforming (OSR) in which both steam and oxygen are fed together and were led to the reformer catalyst. This feeding utilizes the heat generated from exothermic oxidation reactions for endothermic reactions like Steam Reforming. Autothermal Reforming (ATR) is a special case of OSR in which the ratio of oxygen and steam is such that the overall heat of reaction is zero at the reformer temperature [29]. The SR reaction absorbs part of the heat released by the CPOX. The net result can be a slightly endothermic process [10].

However, the realization of an autothermal reforming operation in which the reformer is independent of external heat supply and thermally balanced, is difficult to achieve. Gas concentrations in dependency of the S/C in the case of autothermal diesel reforming can be seen in Figure 2.5.

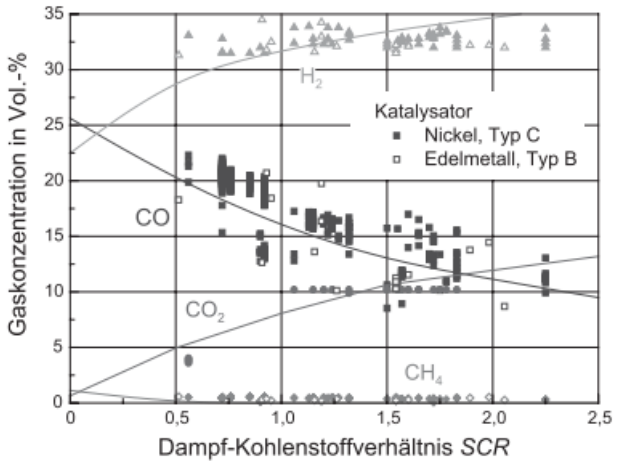

Figure 2.5: Measured and calculated gas composition at ATR with diesel fuel [15]

By increasing S/C the hydrogen yield is increasing, too. In contrast, the CO output decreases which results in a CO_2 increase according to the Water Gas Shift. Picture 2.6 shows the equilibrium amount of the gas components by variation of the temperature for the OSR of surrogate diesel. The maximum hydrogen output is at temperatures around 700°C.
Optimal operating conditions for OSR have been determined at an O/C between 0.7 and 1.0, a S/C between 1.5 and 2.0 and temperatures from 700 to 800°C. Without a catalyst, the reaction kinetics for OSR would be too slow for an equilibrium in the gas phase, therefore it must be catalyzed over noble metals like Rh, Pt, Ru and also Ni [29]. Literature like [1] refer to the practical advantage of OSR for transport applications due to the fast kinetics of CPOX but at a higher H_2/CO ratio because of the prescence of steam.
The reactions occuring during an OSR are not that simple as shown in equation 2.20. The intermediate reactions can be partial, complete and incomplete oxidation, steam and dry reforming and water gas shift.

$$C_nH_m + kH_2O + \frac{n-k}{2}O_2 \rightleftharpoons (k + \frac{1}{2}m)H_2 + nCO; \quad \Delta_R H^0_m \approx 0 \tag{2.20}$$

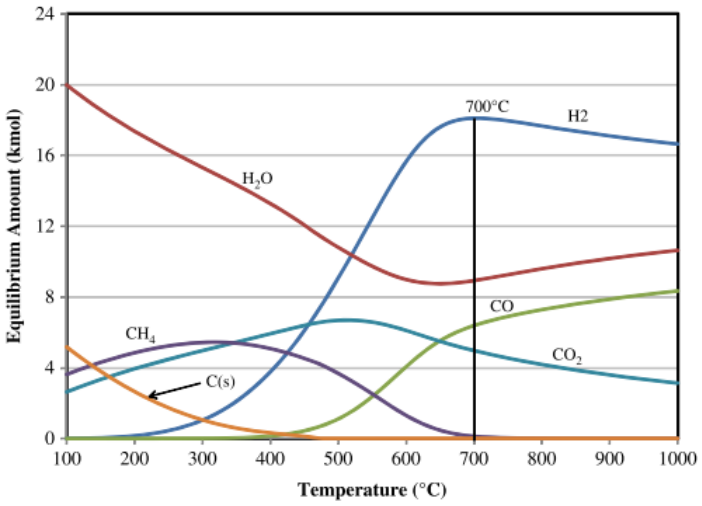

Figure 2.6: Effect of operating temperature on gas composition for OSR of surrogate diesel at O/C=0.7 and S/C=1.5 [29]

According to [22], Catalytic Partial Oxidation and Water Gas Shift mainly occurs on the noble material Pt, Steam Reforming mainly on Rh materials.

Water gas shift

Depending on the temperatures in the system and the gas composition, Water Gas Shift (WGS) can occur as a side reaction of prior named reforming methods when the reactants are present in the gas mixture. Equation 2.21 shows the chemical reaction and the molar enthalpy of reaction.

$$CO + H_2O \rightleftharpoons CO_2 + H_2; \quad \Delta_R H^0_m = -41.2 kJ/mol \tag{2.21}$$

2.3.3 Combustion of Exhaust Gases

The purpose of exhaust gas aftertreatment is the conversion of remaining fuel components in the gas mixture in order to minimize emissions of pollutants. The exhaust gas of a SOFC system fuelled with conventional hydrocarbons, consists of the exhaust gas of the fuel cell and the gas processing unit which can be depleted fuel H_2 and CO, depleted oxidant O_2, products like CO_2 and H_2O but also not fully converted hydrocarbons. The prescence of inert components CO_2, H_2O, N_2 leads

to a reduction of the heating value and therefore to a lower temperature rise compared to a combustion of CH_4 or hydrocarbons which have higher heating values [27].
The exhaust gas aftertreatment is generally performed in an off-gas burner which can be catalytic converters, flame burners or combinations.

Gas phase and catalytic combustion

It can be distinguished between combustion in the gas phase which results in a diffusion flame shown in 2.7 and the combustion in porous media. The main difference lies in the different heat transfer within the combustion zone.
In laminar flames, the heat transfer in the reaction zone is dependent on the heat conduction, radiation and diffusion and the reaction zone is relatively small. Turbulent flames contain vortices which are affecting the heat transfer which results in an increase of the flame front and the burning speed [27].

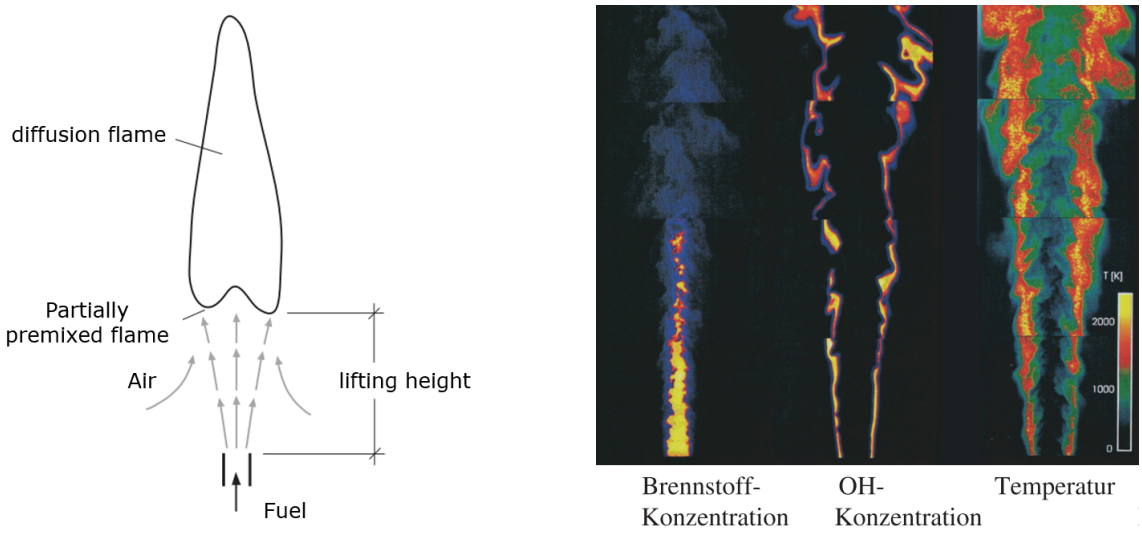

Figure 2.7: Topology of laminar partially premixed (left) and turbulent (right) diffusion flame [23]

In contrast to the laminar combustion in the gas phase, the heat and mass transfer is increased when the combustion is happening in a porous medium which comes from the vortex formation and flow deflection in the inside of the catalyst channels

and lead to a thickening of the reaction zone and an increase of the burning velocity. Additionally, heat will be transported within the solid component of the porous medium through conduction and radiation. Solid bodies have a much higher emissivity and thermal conductivity than gases and so the temperature distribution is much more uniform compared to a combustion in the gas phase.
Combustion processes occur via chain reactions and the reaction scheme is very complex. At low temperatures the reactions in the gas phase are very slow, especially when the chain termination processes outweigh chain formation [23]. When exceeding the fuel ignition temperature, the ignition and flame propagation including several oxidation and decomposition reactions will take place which is recognizable in the released heat. In this chain reaction phase, the chain branching outweighs the chain termination.

Ignition conditions

As soon as the ignition conditions are fulfilled, an autoignition can start, considering that the gas mixture is on the ignition temperature level and the concentrations of the components involved in the ignition process are within certain limits. Table 2.3 shows necessary conditions for ignition of species hydrogen, carbon monoxide and CH_4 [33]. Especially H_2 ignites at a lower temperature and at already very

Table 2.3: Ignition Conditions for fuels H_2, CO and CH_4 in air

Component k	Ignition Temperature [°C]	ν_k [mol/mol]
H_2	560	0.04-0.75
CO	605	0.125-0.742
CH_4	610	0.05-0.15

low concentrations. The ignition temperature of CO is slightly higher at 605°C and starts to ignite at an ignition limit of 12.5%. [28] for instance, refers to a temperature dependency of the concentration ignition limits of H_2. By increased temperature, an enlargement of the limits can be seen acording to Figure 2.8.
At higher temperatures there is, in comparison to lower temperature levels, less fuel or oxidant necessary to heat up the gas mixture to flame temperature. Therefore,

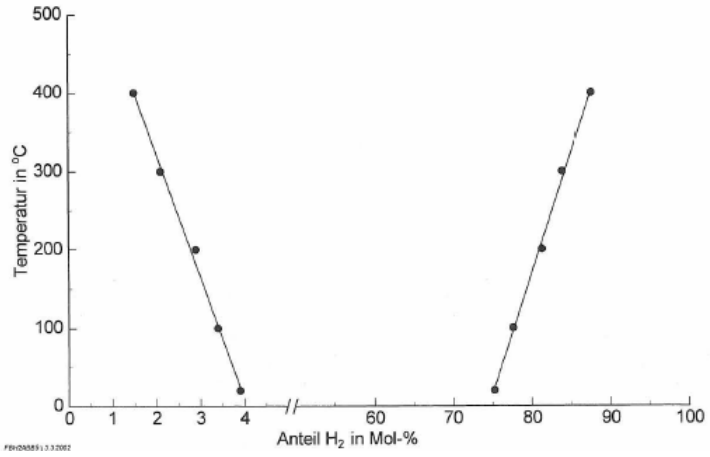

Figure 2.8: Temperature dependency of the ignition limits of H_2 in air at athospheric pressure [28]

at temperatures near the ignition temperature limits, it is not reasonable anymore to use concentration limits for ignition.

Oxidation of hydrogen

Most important intermediate reactions regarding the oxidation of H_2 with oxygen (O_2) are listed in the following chemical formulas, containing arbitrary neutral molecules M and radicals.
The chain initiation 2.22 occurs with the stable molecules H_2 and O_2 forming two radicals of hydroxyl (OH) which proceeds slowly because of the stable initial products. As a result, an autoignition can take place only at high temperatures like 858K [12]. Other literature such as [26] tells about a potential energy surface calculation leading to the conclusion that reaction 2.22 is highly unlikely and leaving 2.23 for initiation, and, in addition, [14] tells about higher importance of 2.23 after performed flow reactor studies for a range of temperatures and pressures.

$$H_2 + O_2 \rightleftharpoons OH + OH \tag{2.22}$$

$$H_2 + O_2 \rightleftharpoons HO_2 + H \tag{2.23}$$

The chain initiation follows chain branching as well as chain propagation. The chain reaction shown in 2.24 represents the most important reaction of the hydrogen-oxygen-system. Out of a stable oxygen molecule and a hydrogen as a radical,

two radicals are formed, namely H and OH. Also in equation 2.25 two radicals are built by one radical and a molecule, which is characteristic for chain branching reactions. Further possible chain branching reactions are shown in equations 2.26 and 2.27 [23].

$$H + O_2 \rightleftharpoons O + OH \tag{2.24}$$

$$O + H_2 \rightleftharpoons H + OH \tag{2.25}$$

$$OH + H_2 \rightleftharpoons H + H_2O \tag{2.26}$$

$$OH + OH \rightleftharpoons O + H_2O \tag{2.27}$$

At the point where all radicals were used up, or more specifically have stabilized, the chain termination occurs. Primarily, reaction 2.28 occurs in prescence of oxygen. Also other chain termination reactions can occur, for example reactions 2.29 and 2.30.

$$H + O_2 + M \rightarrow HO_2 + M \tag{2.28}$$

$$H + H + M \rightarrow H_2 + M \tag{2.29}$$

$$H + OH + M \rightarrow H_2O + M \tag{2.30}$$

On the other hand the produced radical hydroperoxyl (HO_2) out of 2.28 can support chemical reactions that are able to maintain a chain propagation as shown in equation 2.31. The radicals built here can participate in other chain reactions shown above. However, in parallel other reactions happen like 2.32 and 2.33, which counteract and lead to a chain termination.

$$H + HO_2 \rightarrow OH + OH \tag{2.31}$$

$$H + HO_2 \rightarrow H_2 + O_2 \tag{2.32}$$

$$OH + HO_2 \rightarrow H_2O + O_2 \tag{2.33}$$

Oxidation of carbon monoxide

According to [23] there is just one important chemical reaction with which carbon monoxide will be oxidized to carbon dioxide in technical systems, this reaction is shown in 2.34. This means that clean CO can only combust in the prescence of the radical H.

$$CO + OH \rightleftharpoons CO_2 + H \tag{2.34}$$

In the absence of hydrogen, reactions 2.35 and 2.36 occur which produce CO_2 out of CO with a slow reaction speed, where as 2.34 occurs much faster and assumes control of the oxidation already at very low hydrogen concentrations [20].

$$CO + O2 \rightleftharpoons CO_2 + O \tag{2.35}$$

$$CO + O + M \rightarrow CO_2 + M \tag{2.36}$$

Reaction mechanisms for the gas phase

From these chemical equations an equation system can be set up, consisting of the fact that the sum of all mole fractions are equal to one. Then, out of the fact that each type of atom must be conserved several balance equations result. Such an equation system is very difficult to solve, especially when the number of components in the gas mixture is high. It is common that for the calculation of such extended reaction mechanisms special computer software will be used. For instance, GRI30 is such a reaction mechanism which is used for the combustion of H_2 or CH_4 consisting of 325 reactions with 53 species [12]. [26] worked out a small detailed chemical-kinetic mechanism for the combustion of hydrogen and carbon monoxide which has been tested for autoignition because of limitations on computer capabilities.

Catalytic conversion

The mechanism of the catalysis is based on the circumvention of chemical reactions of a high activation energy through the implementation of chemically active group metals which enable other reaction pathways [23].
A heterogenuous catalytic converter consists of a gas phase and a solid phase. The catalytic reactions occur on a solid catalyst like Pt which is mostly applied on a washcoat. Therefore the reactants which are located in the gas phase of a flow, have to be transported to the catalyst to react.
This process is divided into several steps including mass transport and chemical kinetic steps. First, the reactant will be transported to the gas/solid interface and diffuses into the porous catalyst, where it will be adsorbed onto the surface. Then the catalytic reactions occur. Afterwards, the products of the reaction are desorbed

again and diffuse back to the gas/solid interface, where the products will be transported into the gas phase back again.
For modelling of such a heterogenuous catalyst a lot of chemical reaction equations have to be solved. A common approach to combine the chemical kinetic steps to a single step is called Langmuir-Hinshelwood approach shown in Figure 2.9 which is commonly accepted for oxidation catalysts as well as three-way catalysts [3].

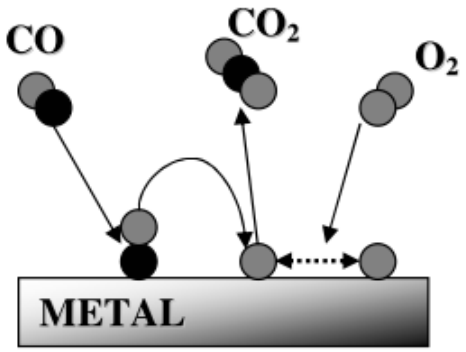

Figure 2.9: Schematic representation of the Langmuir-Hinshelwood mechanism for the catalytic oxication of CO [7]

According to Langmuir-Hinshelwood, two particles which were adsorbed onto the catalytic surface are reacting with each other right at the catalytic surface.
Also [7] tells about a good correlation of measured CO oxidation on Pt and Pd catalysts and the Langmuir-Hinshelwood approach.

3 AVL SOFC APU and Test Results

This chapter describes the AVL APU system, which contains the GPU, the object to be analyzed in this thesis. Furthermore, an APU sytem test at a typical APU operating point was used to establish the boundary conditions for the CFD simulation.

3.1 AVL SOFC APU

The SOFC APU system from AVL can be divided in three main modules which are shown in Figure 3.1, namely the stack module, the Gas Processing Unit (GPU) and the media supply for fuel and air.

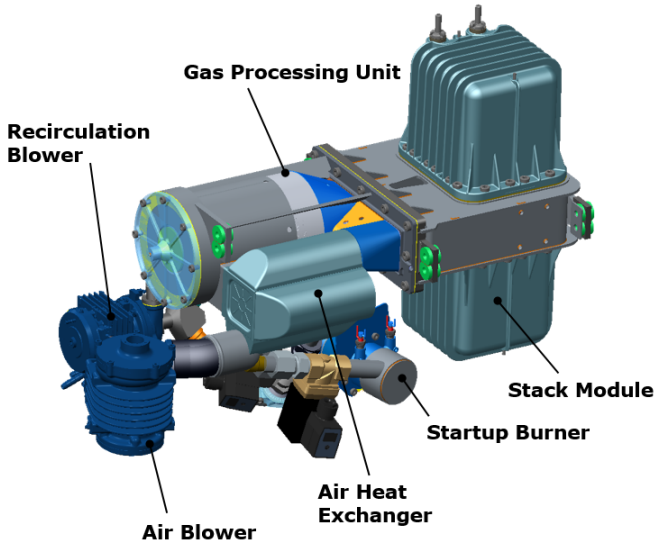

Figure 3.1: system overview of the AVL SOFC APU

The stack module is the module where the electrical power is generated, shown on the right side of Figure 3.1. To deliver the targeted output power, two stacks,

containing planar cells, are arranged in boxer design. The stacks are connected to the GPU by the stack manifold.
The second module is the GPU, wherein the

- reformer for fuel processing
- the off-gas burner for aftertreatment
- the fuel evaporator and
- the startup burner for heat up

are arranged.
The third part of the APU consists of the media supply to provide fuel and oxidant for the stack module via the GPU. The air blower provides the air for the cathode, which will be heated up before entering the stack through the cathode HEX that is also part of the GPU. The recirculation blower provides anode off-gas to the anode line to support fuel processing.
In Figure 3.2 a schematic layout of the APU system is shown. The components contained are described below.

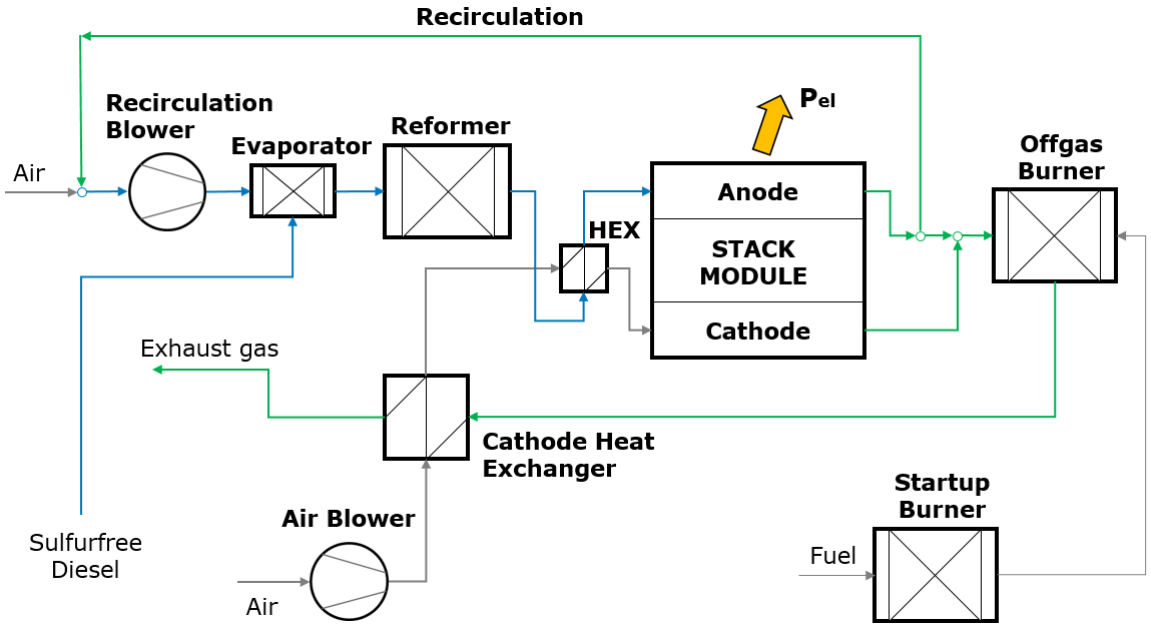

Figure 3.2: Schematic layout of the AVL SOFC APU system

Fuel and Evaporation

The APU is fuelled by sulfur-free diesel fuel what makes a fuel preparation module in form of a desulfurizer unnecessary. The fuel is pumped from the fuel tank into the evaporator. Technically, the evaporator is made of a fleece manufactured out of a high temperature material. The fuel reaches the fuel fleece due to four bores in the gas processing unit housing. The fuel which is pumped continuously during the operation mode, gets evaporated with the heat from hot recirculated fuel cell anode off-gas which is mixed with fresh air.

Reformer Pipe

After the evaporation, the gas mixture flows along the reformer pipe which is used as mixing chamber as well as for gas overheating. The reformer pipe should be long enough to enable uniform flow distribution at reformer inlet but also short enough to meet packaging restrictions. Due to the tangential alignement of the anode recirculation pipe a strong swirl flow is etablished in the reformer pipe.

Reformer

In the reformer catalyst, chemical reactions happen and deliver a hydrogen rich gas at fuel cell inlet. The reformer in the established system is a catalytically coated monolith and should enable OSR because of the prescence of H_2O as well as of O_2 in the gas mixture of the anode line.
The reformer catalyst used in the APU test consists of a square cell monolith made out of Cordierite (Mg2Al4Si5O18) and has a cell density (*cpsi*) of 400. The applied coating partly consists of Rh. For more detailed properties of the reformer catalyst see Table B.2 in the appendix chapter 7.3.

Stack Inlet Heat Exchanger

Upstream to the stack module a HEX is positioned, called HEX in picture 3.2. The purpose of this Heat Exchanger (HEX) is to adjust the temperatures of anode and cathode inlet and it is designed as an assembly of curved pipes.

Startup Burner

The startup burner is active in the startup mode only, to heat up the system to nominal temperature level. The stacks and the catalysts should be at operation temperature before the operation mode can start. Therefore, a combustion of fuel is done, the produced heat is led to the off-gas burner and to the other components. In the SOFC operation mode, the startup burner is not active which means that no fuel and no oxidant is added there.

Off-gas Burner

A part of the fuel cell anode exhaust gas will be recirculated, the other part and the whole cathode off-gas are merged in the mixing chamber before the off-gas burner. In the anode exhaust gas there is some depleted fuel like H_2 and CO and in the cathode off-gas depleted oxidant. This leads to an oxidation of H_2 and CO with O_2 in the off-gas burner. The off-gas burner is designed as an oxidation catalyst, which performs a complete combustion of carbon monoxide and hydrogen. The heat which results from the exothermic catalytic combustion in the off-gas burner will be used to support the fuel evaporation and gas reforming.
The oxidation catalyst has a s-shaped metallic carrier with a *cpsi* of 400. The precious metal applied on the carrier is a mixture of Platinum (Pt) and Palladium (Pd). Detailed properties and material properties of the metallic carrier, material 1.4767, are shown in Table B.2 in the appendix chapter 7.3.

Cathode Heat Exchanger

The cathode HEX has the purpose to utilize the heat coming from the off-gas burner for heating up the cathode line air before entering the cathode side of the stack module. The cathode HEX is designed as a plate heat exchanger and its properties can be seen in the appendix A.6. The channel shape is rectangular and the hydraulic channel diameter is 0.95 mm.

3.2 APU Test Bed and Configuration

Figure 3.3 gives an impression of the SOFC APU at the test bed. A system test was carried out at a total stack output power of 3 kW and a system efficiency of 32 %, which was analyzed in order to determine the boundary conditions for the CFD simulation. Test results were evaluated at a stationary SOFC operation point.

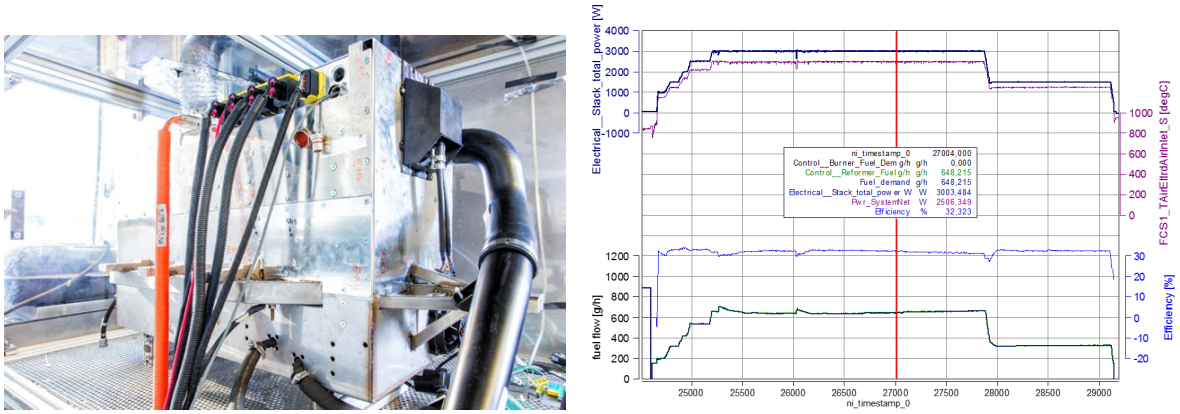

Figure 3.3: AVL SOFC APU on the test bed and test overview

Temperatures and pressures were measured at specified measurement points. A gas analysis was performed, the extraction point therefore was at reformer catalyst outlet. General test conditions can be read out from Table 3.1. Diesel was applied to the evaporator fleece with a fuel rate of 650 g/h. The cathode line was charged with air at 35500 Nl/h. Also to the anode line air was added with a volume flow of 2550 Nl/h. The recirculation rate was about 35% and the startup burner was not active in the operation mode.

3.3 Test Results

Test measurement points which affect the simulation of the gas processing unit are collected in Figure 3.4, containing temperature and pressure probes at specific points, volume flows of each line and a gas analysis was performed in the anode line.
In Figure 3.4

- the anode line is colored in blue,

Table 3.1: Main Test Conditions of APU test

Property	Unit	Value
Electrical Stack Total Power	kW	3
Stack Current	A	24.6
Fuel Type	-	Diesel
Fuel Rate	g/h	650
Fuel Utilization (η_{fu})	-	0.7
Recirculation Rate (r_{rec})	%	35
Reformer Air Supply	Nl/h	2550
Recirculation Gas	Nl/h	2800
Cathode Air Supply	Nl/h	35500
Startup Burner Air Supply	Nl/h	0

- the cathode line in grey and
- the exhaust line in green.

Stack Module: The stack module consists of 2 stacks containing 75 fuel cells each. The total power output was 3000 W and the stack current was 24.6 V. The fuel utilization was about 70%. According to the measured temperatures, the anode line of the stack produced heat which caused a temperature rise of about 100°C and a pressure loss of 12mbar. At the stack cathode line the temperature increased by about 120°C and the pressure loss is 37mbar which results from the much higher massflow in the cathode line. The temperatures of anode and cathode line at stack outlet seem to be well adjusted.

Evaporator: The measurement indicates that in the evaporator a heat adsorption of 12 K occurs from point (3) to (5) due to the endothermic enthalpy of evaporation of diesel fuel (4) coming from the tank. The numbers (1) to (12) represent measurement points shown in Figure 3.4. The measured temperature after the evaporation area (5) is located right next to the surface of the evaporation fleece. Due to the high temperature level at evaporator outlet above 400°C, it is assumed that the liquid fuel was completely evaporated before reaching the reformer pipe.

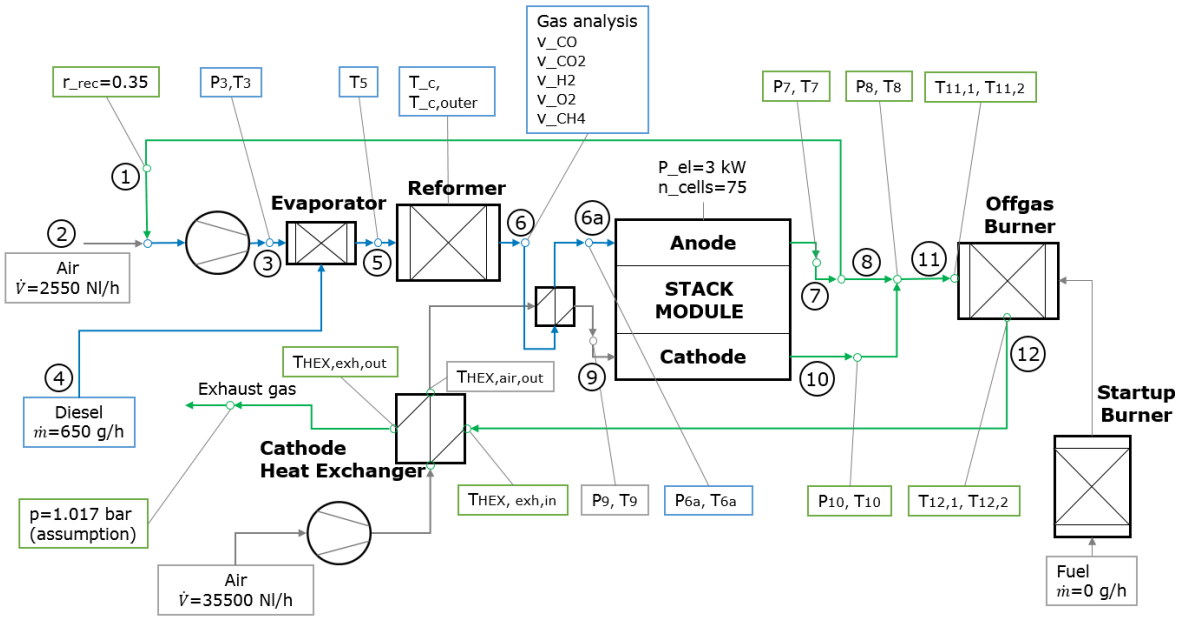

Figure 3.4: Extracted test results of APU Test

Reformer: The reformer catalyst shows a high heat release. The temperature measured in the mid center of the reformer is about 770°C, more outwards towards the outer wall the temperature measured is about 20 °C higher. This temperatures can be explained through a mostly exothermic reforming reaction happening in the reformer catalyst and heat conducted from radially surrounding oxidation catalyst. Due to the fact that in the examined SOFC APU system, a mixture of fuel (4), air (2) and recirculated anode off-gas (1) containing water vapour will reach the reformer (5), the reforming process can be described as Oxidative Steam Reforming (OSR). The oxygen to carbon ratio (O/C) of the reformer gas determined is 1.6 and the steam to carbon ratio (S/C) is 0.35. The higher O/C and lower S/C ratio than usual for OSR are an indicator of a predominance of a Catalytic Partial Oxidation (CPOX), which may be the reason of a strongly exothermic reaction in the reformer catalyst. The outer temperature measured in the reformer catalyst was about 20°C higher than the center temperature. This can be explained by heat transfer from the hotter exhaust line which is arranged in a counterflow to the anode line and connected via a solid wall.

Stack Inlet Heat Exchanger: The HEX is able to increase the temperature of the cathode line from cathode HEX outlet until stack cathode inlet by about 85°C by transferring heat from the anode line before stack inlet. Therefore, the temperatures of anode and cathode line seem to be well adjusted at SOFC stack inlet which can be traced back to the HEX located at stack inlet. It can be concluded that the implementation as well as the design of the stack inlet HEX is reasonable and serves its purpose.

Mixing chamber: H_2 and CO containing anode and O_2 containing cathode exhaust gas coming from the stack module, are mixed within the ring shaped mixing chamber (11) located before the off-gas burner. The high temperatures of around 850°C which were measured near the mixing point allow the assumption that there is an exothermic combustion already directly at the mixing location.

Off-gas Burner: At the off-gas burner inlet as well as at the outlet cross section, two temperature probes were arranged. Regarding the burner inlet, a temperature difference of 40°C between the probes indicates an unevenly distributed flow and temperature field. This effect can also result from an early combustion in the mixing chamber. The temperatures at the off-gas burner outlet are around 800 °C with a temperature difference between the two probes of 15°C. Comparing the temperatures at oxidation catalyst inlet to the temperatures measured at oxidation catalyst outlet, there is only a small difference. This can be explained by a nearly completed combustion already in the mixing chamber but also by heat transfer from the off-gas burner to the reformer which are coupled directly in order to exchange heat. The temperature decrease of about 80°C from off-gas burner outlet to cathode Heat Exchanger inlet is probably caused by the heat transfer from the exhaust line to the anode line in this section.

Cathode Heat Exchanger: The mixed and processed exhaust gas (12) then flows through the cathode HEX in order to heat up the cathode air for the SOFC stack then leaves to the environment. The performance of the HEX regarding the cathode line is satisfying due to the high temperature at stack inlet. Due to the fact that there is still a relatively high temperature of 360°C at cathode HEX outlet, the heat transfer in the exhaust line upstream the cathode HEX should be improved. The exhaust gas

pressure after the HEX was estimated based on a bended exhaust gas pipe, located downstream to the environement. Therefore, a pressure drop of 4mbar was taken into account.

3.4 Calculation of Boundary Conditions

The boundary conditions and other input data needed for the CFD simulation were extracted from different pre-calculations and 1D simulations. The transition between APU test results and boundary conditions for the 3D CFD investigation is described in this section.
As shown in the test results in Figure 3.4, the gas analysator was connected to the line after the reformer (6) and measured species like CO, CO_2, H_2, O_2 and CH_4. During the measurement, the H_2O is evaporated by the gas-phase chromatograph, so that it is just possible to get measurement results of dry gas composition. In reality, because of a water production which occurs in the anode line of the SOFC stack and a recirculation of anode off-gas, the prescence of H_2O can not be neglected. In order to obtain the wet gas composition at measuring point reformer outlet (6), a balance calculation was implemented. Also the mole fraction of N_2 had to be introduced in the calculation.

Balance Calculation: The system anode line happened and that the gas mixture consists of no other species than H_2, CO, H_2O, O_2, N_2 and CH_4. In Figure 3.5 the calculation system anode line including the defined system boundary is illustrated.

Constraints for the calculation were that N_2, an inert gas, should be conserved. The volume flow ($\dot{V}$) is measured in Nl/h what can be converted into mole flow ($\dot{n}$) using the mole volume (V_m) which is constant for gases with ideal gas characteristics. For the balance calculation, the mole flows of introduced air (2) and fuel (4) were split into its atomic components. Each atomic component has to fulfill the mass conservation in each point of the system (equation 3.1).

$$\sum \dot{m}_{in} - \sum \dot{m}_{out} = 0 \tag{3.1}$$

Besides that, the balance of the mole flows for the regarded system can be written as follows (equation 3.2) in which k is an arbitrary variable for an atomic component

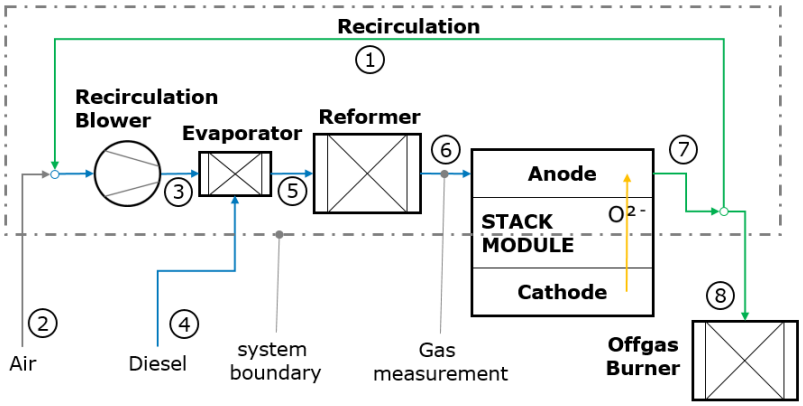

Figure 3.5: Schematic layout of anode line for calculation of boundary conditions

like C, H, O, N.

$$\dot{n}_{\mathrm{k,air}} + \dot{n}_{\mathrm{k,fuel}} + \dot{n}_{\mathrm{k,stack}} - \dot{n}_{\mathrm{k,anode,out}} = 0 \tag{3.2}$$

$$\dot{n}_{\mathrm{k,2}} + \dot{n}_{\mathrm{k,4}} + \dot{n}_{\mathrm{k,stack}} - \dot{n}_{\mathrm{k,8}} = 0 \tag{3.3}$$

As explained in section 2.1, in the SOFC stack during operation there is a flow of oxygen ions from cathode to anode. This increase of oxygen has to be considered in the calculation. Regarding to Faraday's law, the mole flow of these oxygen ions can be calculated from the overall stack current and the Faraday constant according to equation 3.4.

$$\dot{n}_{\mathrm{k,stack}} = \frac{(I_1 + I_2) \cdot n_{cells}}{F} \tag{3.4}$$

By using the recirculation rate (equation 2.14), the recirculation path composition (1) can be determined which will be introduced again before the recirculation blower, where the flow will be mixed with fresh air.
The balance calculations then resulted in a comparison of the atomic components measured during the APU test at reformer outlet. The mole fraction of H_2O was adjusted in such a way, that finally the deviation of (atomic component) mole fractions between measurement and calculation was kept to a minimum of 2.9%. An extract of the Microsoft Excel sheet used can be seen in the appendix A.5.

1D simulation: For the stack, which was treated as a blackbox in the CFD simulation, a 1D matlab simulation in order to obtain stack anode and cathode outlet

composition, was performed by AVL. The input data was

- the electrical stack power,
- the number of cells,
- the stack current,
- stack pressure loss coefficients for anode and cathode,
- the temperatures and pressure levels taken from the measurement,
- the gas composition of anode inlet gas, determined with balance calculations from measurement data as explained above, and
- cathode inlet gas composition (composition of air).

The input parameters and results of the matlab stack simulation can be found in A.1 and A.2 and an overview of the matlab stack model is shown in Figure 3.6.

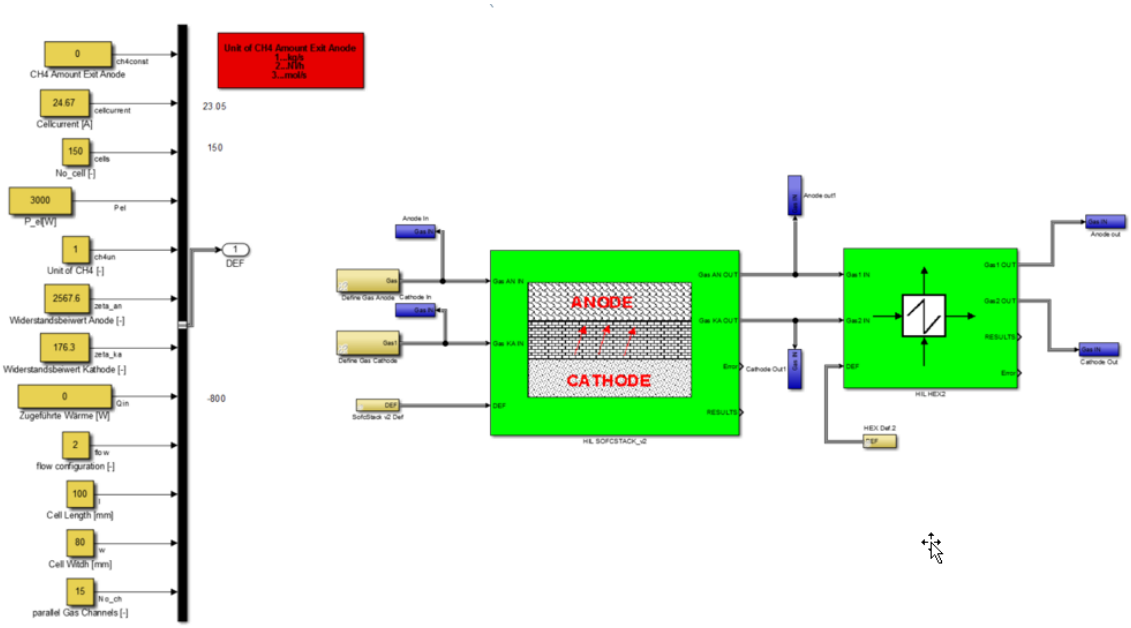

Figure 3.6: Overview of matlab stack model and general input data

In addition, an evaporator and a reformer module was added to the matlab layout

to consider the heat of reaction of the evaporation and the reforming process. The chemical reactions (SR, CPOX and WGS) happening in the reformer and the phase transition in the evaporator were calculated with the minimization of the free Gibbs energy. The complete matlab model can be seen in the appendix Figure A.3 and the outcome is illustrated in A.4. Right at the bottom of Figure A.4, the heat of reaction of evaporation and reforming process can be seen. The reforming process is, as expected from measurement, an exothermic process because of a heat release of 1009 W.

3.5 Boundary Conditions for CFD Simulation

Finally, in Figure 3.7 the results of measurement data extraction, boundary condition calculations and 1D simulations are summarized. These are the boundary conditions and the input data used for the CFD simulation.

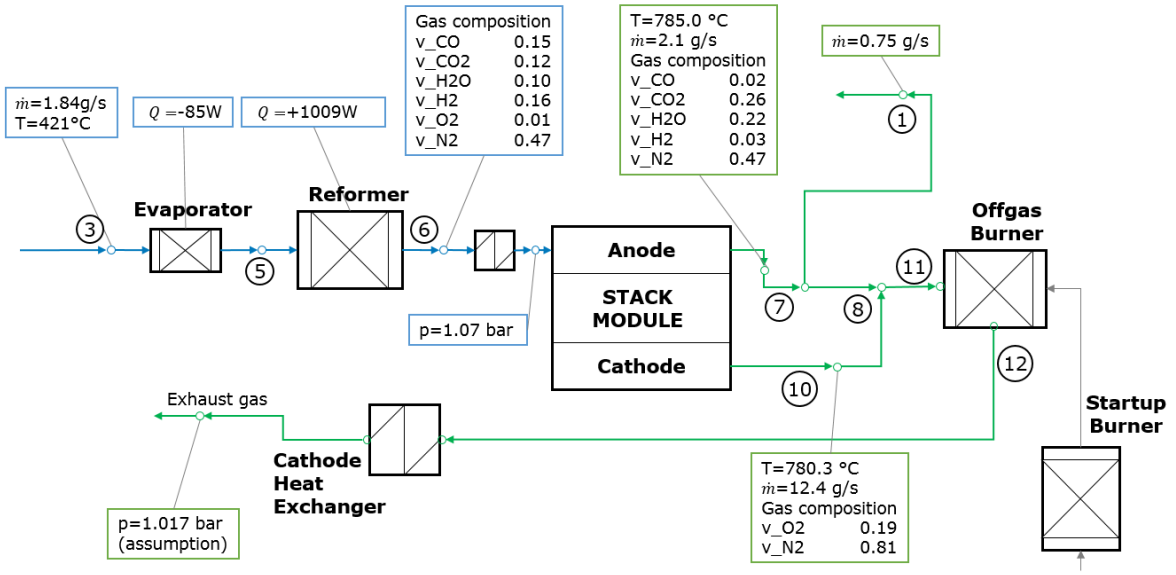

Figure 3.7: Boundary conditions of the analysis model of the GPU

The inlet of the anode line has a temperature of 421°C and a massflow of 1.84 g/s. The gas composition which was calculated from a dry gas measurement, was prescribed constant in the whole anode line. At the outlet of the anode line the

measured pressure of 1.07 bar is imposed.
The exhaust line contains a mixing chamber where anode and cathode outlet gases from the stack are mixed. The gas compositions of the inlet flows before the mixing chamber are shown in the Figure 3.7. At the outlet of the exhaust line a pressure of 1.017 bar was prescribed in order to take into account the pressure loss of the exhaust line which exits to ambient.

4 Basics of CFD and Modelling in FIRE

4.1 Conservation Laws

In solid domains (structure material) the transport of the energy is only taken into account by heat conduction. In the gas phase, the intensity of the flow is effecting the energy transport, too. To get the information about the temporal and spatial distribution of the physical quantities in a specific geometry, conservation laws for mass, momentum, energy and species distribution have to be solved. All these equations are in a similar form and show the conservation of a quantity. A general differential form of such a transport equation in the gas phase is shown in equation 4.1 where ϕ stands for an arbitrary quantity like the 1 for the equation of continuity, velocity for the equation of motion (Newton's second law), the specific enthalpy (h) for the energy equation, the mass fraction of component k (μ_k) or a turbulence parameter. Some possible values for ϕ are illustrated in Figure 4.1. i describes a control variable in the coordinate directions x, y and z.

$$\frac{\partial \rho \phi}{\partial t} + \frac{\partial \rho u_i \phi}{\partial x_i} = \frac{\partial}{\partial x_i}(\Gamma_\phi \frac{\partial \phi}{\partial x_i}) + S_\phi \tag{4.1}$$

Term 1 on the left in equation 4.1 is the transient term, which represents the temporal change of a quantity. Term 2 from the left to the right shows the convection term, which represents the convective transport caused by the flow, containing the flow velocity.
At the right side of the equal sign there is the diffusion term, which contains molecular material transport through the surface of a control volume, like heat conduction and momentum exchange through molecular viscosity. The very right term is a source term to represent, for example, a heat source or a gravity force [2].

Table 4.1: Values for ϕ and their equations [16]

ϕ	**Equation**
1	Continuity Equation
u	Navier-Stokes Momentum Equation in x-direction
v	Navier-Stokes Momentum Equation in y-direction
w	Navier-Stokes Momentum Equation in z-direction
h	Energy Equation

4.2 Boundary Layer Theory

A fluid stream developes a boundary layer in the contact area between fluid and wall, which consists of a laminar boundary sub-layer near the wall and a turbulent boundary layer with increasing distance to the wall. Directly at the wall, the no slip condition $u, v, w = 0m/s$ is valid. Figure 4.1 shows the structure of the boundary layer. The boundary layer can be divided into laminar sublayer, buffer layer and fully turbulent region. Between laminar and turbulent regions there is a transition region, which is at a certain distance from the begin of the boundary layer (at $x = 0$ in Figure 4.1) normal to the wall. The transition from laminar to turbulent flow happens at the critical Reynolds number (Re).

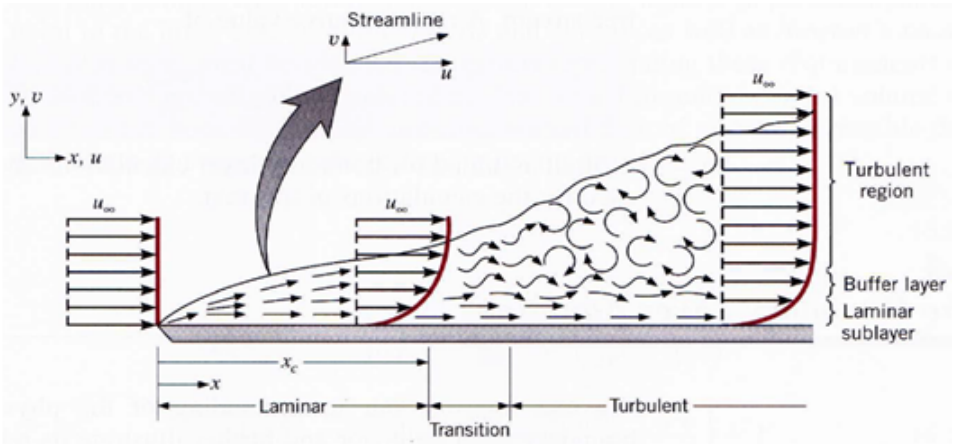

Figure 4.1: Structure of boundary layer containing laminar, turbulent and transition region [34]

Responsible for this effect is the dynamic viscosity (μ) which is a temperature and

pressure dependent fluid property. The viscosity is related to shear stress (τ) and the velocity gradient.

$$\tau = \mu \frac{du}{dy} \tag{4.2}$$

The boundary layer theory deals with a division of the flow into two regions, namely the core flow and the boundary layer where the friction, and therefore the shear stress, has to be taken into account.
To distinguish the boundary layer areas, the dimensionless near wall variables dimensionless near wall velocity (u^+) and dimensionless wall distance (y^+) were introduced. They are listed in equation 4.4 and 4.5 by use of friction velocity u_τ (equation 4.3).

$$u_\tau = \sqrt{\frac{\tau_w}{\rho}} \tag{4.3}$$

$$y^+ = \frac{u_\tau \cdot y}{\nu} = y \cdot \frac{\sqrt{\tau_w / \rho}}{\nu} \tag{4.4}$$

$$u^+ = \frac{u}{u_\tau} = u \cdot \sqrt{\frac{\rho}{\tau_w}} \tag{4.5}$$

y^+ is also an important measure of the distance between the wall and the first grid line which is next to the wall [25]. Therefore, the y^+ value of the first grid line is an indicator of the mesh resolution at the wall and is influencable by mesh modifications.
Figure 4.2 shows the relation between y^+ and u^+ for the different regions of the boundary layer.
According to the dimensionless wall distance, the flow is in the viscous sublayer when $y^+ < 5$. The transition zone means a value of y^+ between 5 and 60 and above, fully turbulent flow governs.

4.3 Heat Transfer

Heat Q is a thermal energy which is transferred between a system and its environment due to a temperature difference. The direction of the heat transport is always from higher to lower temperature level. The heat transferred within a specific time frame is called heat flux ($\dot{Q}$) (4.6) and the heat flux density ($\dot{q}$) is the heat flux which

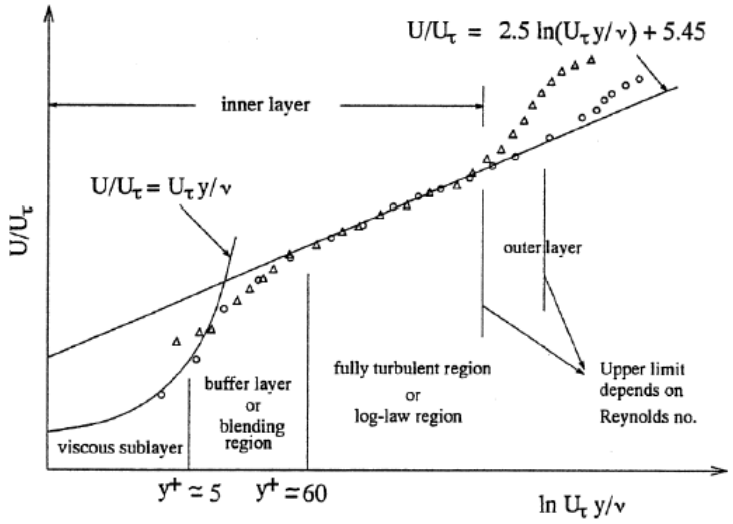

Figure 4.2: Subdivisions of near wall region [25]

is conducted through an area unit of an arbitrary surface (equation 4.7) [18].

$$\dot{Q} = \frac{dQ}{dt} \tag{4.6}$$

$$\dot{q} = \frac{d\dot{Q}}{dA} \tag{4.7}$$

A distinction of the heat transfer is made between heat conduction, convection and radiation.

Conduction

Heat conduction represents a transport of energy between adjacent molecules in a material which is driven by a temperature difference. Conduction can occur in all materials whether they are in solid, liquid or gaseous state. $\dot{q}$ is dependent on thermal conductivity (λ) when a certain tempature gradient dT/dx is given. Equation 4.8 is also called the Fourier's Law. The negative sign before λ results in a positive heat flux when a negative temperature gradient is observed. In general, thermal conductivity is high for solid materials, low for gases and for liquids it is in between [18].

$$\dot{q} = -\lambda \frac{dT}{dx} \tag{4.8}$$

Convection

Heat convection is the transport of energy within a fluid flow because of the transport of enthalpy and kinetic energy by the flow why it is also dependent on flow characterisitcs like flow velocity or turbulence. For the analysis of heat transfer for example in a heat exchanger, it is of special importance to analyze the convective heat transfer between wall and fully developed core flow. Picture 4.3 shows the behaviour of temperature and velocity in wall-normal direction in the boundary layer where high gradients can be seen.

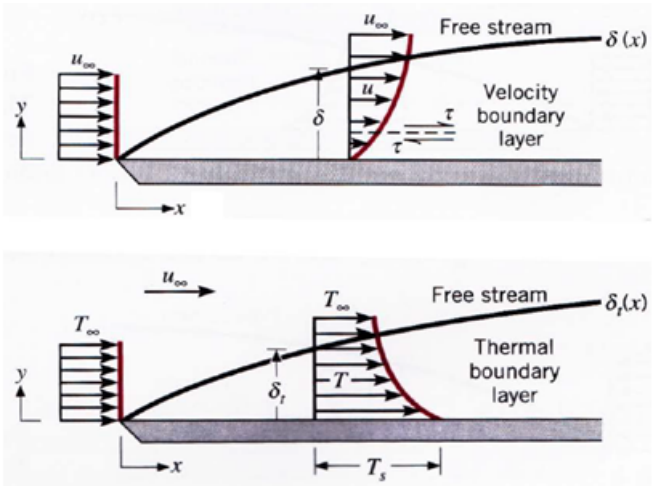

Figure 4.3: Temperature (below) ande velocity (above) profile in the boundary layer of a stream [34]

The convective heat flux density through which heat will be transferred from the wall with T_w to the core flow T_∞ can be expressed by equation 4.9 using the heat transfer coefficient (α). The heat transfer coefficient depends on many factors like temperature dependent flow properties, velocity and process parameters [18]

$$\dot{q} = \alpha(T_w - T_\infty) \tag{4.9}$$

Radiation

Radiation is the energy which is generated out of electromagnetic waves which an object emitts. The heat transport increases with increasing surface temperature of the object and smaller distance to neighbouring parts receiving the energy [18].

Energy balance in an open system

Due to the fact that this thesis deals with a Gas Processing Unit containing several gas streams, a definition of the energy balance is helpful.
According to the first law of thermodynamics for open systems, equation 4.10 is valid. The adoption of a stationary flow leads to the neglection of the change of inner energy (U) and outer energy (E_a) and without a generated or consumed power we can write equation 4.11 containing enthalpy flows through system boundaries [11].

$$dQ + dW + \sum dm_i \cdot (h_i + e_{a,i}) = dU + dE_a \tag{4.10}$$

$$dQ + \dot{m}_i \cdot (h_{out} - h_{in}) = 0 \tag{4.11}$$

The specific heat capacity at $p = \text{const.}$ (c_p) describes the amount of energy which is necessary to increase the temperature of a species and is usually dependent on temperature (4.12) [11].

$$c_p = \frac{\partial h}{\partial T} \tag{4.12}$$

4.4 Modelling in FIRE

4.4.1 Species Transport

The AVL CFD Simulation program (FIRE^{TM}) module Species Transport offers the possibility to calculate gas mixtures. Because of different gas compositions in the flow of the analysis model (GPU), the Species Transport Module is used for all CFD calculations investigated in this work.
The user can choose between two different options for Species Transport, namely

- General Species Transport and
- Standard Species Transport.

In the 'Standard' Species Transport module the system of chemical species is predefined and is used for combustion, spray and wall film applications. The polynomial evaluation directly delivers the integral values of c_p[24].

In the 'General' Species Transport module can treat gaseous but also liquid substances and an arbitrary number of chemical species with an arbitrary set of properties can be defined. It is used for multi-component mixing and catalyst applications. Therefore for the present investigations General Species Transport is used.
In the Species Transport module additional transport equations for each component k of the gas mixture are solved. This can be expressed in the form of equation 4.13 which is related to equation 4.1. μ_k represents the mass fraction of an individual chemical species k [6].

$$\frac{\partial \rho \mu_k}{\partial t} + \frac{\partial \rho u_i \mu_k}{\partial x_i} = \frac{\partial}{\partial x_i}(\Gamma_{\mu_k} \frac{\partial \mu_k}{\partial x_i}) + S_{\mu_k} \tag{4.13}$$

The diffusion coefficient (Γ) is calculated via the diffusion coefficient (D) of species k in the mixture, the turbulent viscosity (μ_t) (which is not a material property but a measure of turbulence) and the turbulent (t) Schmidt number (S_c).

$$\Gamma_{\mu_k} = (\rho D_k + \frac{\mu_t}{Sc_t}) \tag{4.14}$$

The source term in case of Species Transport consists of the reaction rate ($\dot{r}$) and the molecular weight (M) of species k.

$$S_{\mu_k} = \dot{r_k} \cdot M_k \tag{4.15}$$

Thermochemical quantities

In FIRE^{TM} General Species Transport, the molar enthalpy (H_m), molar entropy (S_m), molar heat capacity at $p = \mathrm{const.}$ ($C_{\mathrm{m}p}$) are calculated using polynomial approaches according to the National Aeronautics and Space Administration (NASA). Following formulas show the polynomials of $C_{\mathrm{m}p}$ (equation 4.16) and H_m (equation 4.17) containing the fitting coefficients a_ik. For the CFD calculation, the access to the database for the a_ik polynomials has to be ensured [6].

$$\frac{C_{mp}}{R} = a_{1k} + a_{2k} \cdot T + a_{3k} \cdot T^2 + a_{4k} \cdot T^3 + a_{5k} \cdot T^4 \tag{4.16}$$

$$\frac{H_k}{R} = a_{1k} + \frac{a_{2k}}{2} \cdot T + \frac{a_{3k}}{3} \cdot T^2 + \frac{a_{4k}}{4} \cdot T^3 + \frac{a_{5k}}{5} \cdot T^4 + \frac{a_{6k}}{T} \tag{4.17}$$

Specific heat and enthalpy

On basis of the definition of the specific heat capacity at $p = \text{const.}$ made in section 4.3, the difference of the specific enthalpy (h) within a certain temperature range can be written as in equation 4.18.

$$h\big|_{T_1}^{T_2} = \int_{T_1}^{T_2} c_p dT \tag{4.18}$$

In the FIRE^{TM} code the lower temperature limit is defined at 0K and the upper limit is the actual temperature Tp. Because of the fact that at lower temperatures a gas changes to a liquid aggregate state and that c_p is not defined until the 0K point, the equation will be split into two parts, shown in 4.19. The reference temperature T_{ref} therein can be chosen arbitrarily, it just determines the relative enthalpy level.

$$h\big|_0^{T_\text{p}} = \int_0^{T_\text{p}} c_p \mathrm{d}T = \int_0^{T_\text{ref}} c_p \mathrm{d}T + \int_{T_\text{ref}}^{T_\text{p}} c_p \mathrm{d}T = h_\text{ref} + \int_{T_\text{ref}}^{T_\text{p}} c_p \mathrm{d}T \tag{4.19}$$

In CFD a transport equation for the total enthalpy h_{tot} (equation 4.20) is solved but not for temperature. The temperature results out of equation 4.21 where the 'integral' c_p is included directly [24].

$$h_\text{tot} = h_\text{ref} + \int_{T_\text{ref}}^{T_\text{p}} c_p \mathrm{d}T + \frac{|\overline{u}|^2}{2} \tag{4.20}$$

$$T_p = \frac{h_\text{tot} - \frac{|\overline{u}|^2}{2} - h_\text{ref}}{\overline{c_p}} + T_\text{ref} \qquad \overline{c_p} = \frac{1}{T_\text{p} - T_\text{ref}} \cdot \int_{T_\text{ref}}^{T_\text{p}} c_p \mathrm{d}T \tag{4.21}$$

For FIRE^{TM} Standard Species Transport, the reference temperature is often 0 K, otherwise it might be 298.15 K or the initilization-temperature in FIRE.
When using General Species Transport in the simulation, it is important to take into account the reference temperature for the enthalpy equation. The reference temperature is then derived from an arbitrary initial temperature. In the case of including the aftertreatment module, this initial temperature is taken from the aftertreatment porosity.
The face-averaged heat flux based on the total enthalpy evaluated for an arbitrary flow cross section can be written as in formula C in the appendix.

4.4.2 Wall treatment

For modelling the near wall region, two approaches are common which are illustrated and described in Figure 4.4. First, at the right side, the calculation cells in the near wall area are very fine, in order to describe the high velocity and temperature gradients near the wall. The many computational cells lead to an increasing demand of computing power. In the other approach, the laminar sublayer and the buffer layer of the boundary layer are not resolved. As an alternative, semi-empirical wall functions enable a bridging between the wall and the fully turbulent region. This method with the purpose of reducing computing time enables an approximation of velocity and temperature distribution near the wall.
FIRE^{TM} provides several wall treatment models, the most commonly used are

- hybrid wall treatment for the velocity and
- standard wall function for the temperature.

Therein, there are implemented special adjustments for the transition zone between the wall boundary layer and the sublayer.

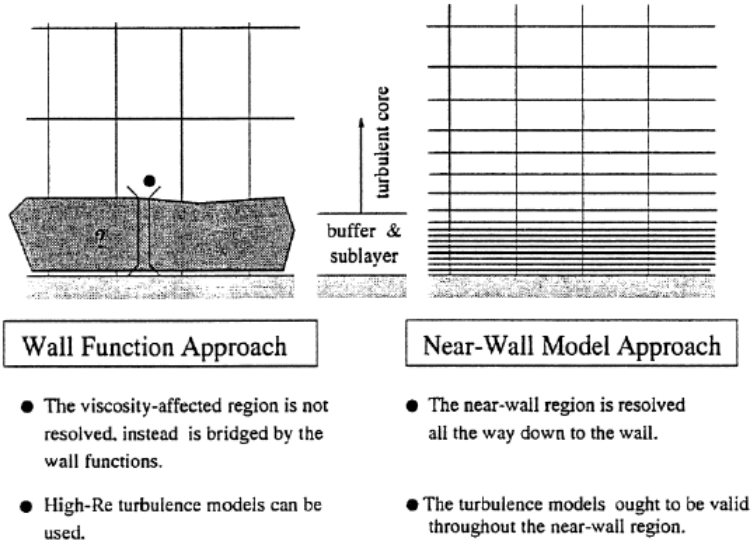

Figure 4.4: Two types of near wall treatments [25]

Hybrid wall treatment

The hybrid wall treatment model allows to find u^+ as function of y^+. Hybrid wall treatment ensures a gradual change between the turbulent and the laminar boundary layer near the wall using a switching function. Equations 4.22 and 4.23 show the relations between y^+, u^+ and the switching function Γ for hybrid wall treatment, wherein κ is the Von Karman constant.
If y^+ is very small (near the wall), Γ also becomes very small which results in a higher relevance of the left term of equation 4.22. On the other hand, the left term of equation 4.5 can be neglected if y^+ becomes higher. Γ (equation 4.23) regulates the transition, depending also on the Prandtl number (Pr) [4].

$$u^+ = y^+ e^{-\Gamma} + \left[\frac{1}{\kappa} ln(Ey^+)\right] e^{-\frac{1}{\Gamma}} \tag{4.22}$$

$$\Gamma = \frac{0.01(Pry^+)^4}{1 + 5Pr^3 y^+} \tag{4.23}$$

Standard wall function

As well as the velocity boundary layer also the temperature boundary layer follows a dimensionless temperature profile. Standard wall function is a set of semi-empirical functions regulating the heat transfer at walls. Similar expressions as explained before are used. For the dimensionless temperature difference T^* the following formula 4.24 applies with the use of an empirical constant C_μ:

$$\frac{1}{\alpha} \approx \underbrace{C_\mu{}^{\frac{1}{4}} k_c{}^{\frac{1}{2}} \frac{\rho c_p (T_c - T_w)}{\dot{q}_w}}_{T^*} = Pr_t \left[\frac{1}{\kappa} ln(Ey^+) + P\right] \tag{4.24}$$

where T_w is the wall temperature and T_c the center temperature of the wall nearest cell. $\dot{q}_w$ is the wall heat flux density and k_c the turbulent kinetic energy of the wall nearest cell. The dimensionless temperature difference T^* is equivalent to the reciprocal of the heat transfer coefficient (α). The P-function which models the resistance of the laminar thermal sub-layer is explained in equation 4.25 [4].

$$P = 9.24 \left[\left(\frac{Pr}{Pr_t}\right)^{\frac{3}{4}} - 1\right] \left[1 + 0.28 exp\left(-0.007 \frac{Pr}{Pr_t}\right)\right] \tag{4.25}$$

4.4.3 Aftertreatment porosity

The AVL FIRE^{TM} Module Aftertreatment offers simulation capabilities related to flow, heat transfer and catalytic surface reactions for various exhaust gas aftertreatment applications, for instance, regarding engines [3]. A porous material like a catalytic converter has fine-scale geometrical structures which require a lot of computational cells and, therefore, an immense demand of computing time. To overcome this issue, the material is modelled by a porosity (ε) containing gas phase and solid substrate at the same time. The ε is the ratio of gaseous volume (V_{gas}) to an overall volume V as shown in equation 4.26, which is identical to the open frontal area (OFA) of a monolith.

$$\varepsilon = \frac{V_{gas}}{V} \tag{4.26}$$

In CFD, the porosity block has to be composed of a block-structured grid and the distance between the porosity zone and other arbitrary interfaces in flow direction have to be at least two cell layers [5].

Pressure drop modelling

The porosity module simulates flow through a porous material by considering a pressure loss. For instance, this can be a pressure drop model

- according to **Forchheimer** or
- a **Tube Friction** model.

Forchheimer: Regarding the Forchheimer pressure drop model, equation 4.27 shows the pressure gradient within a porous material $\frac{\partial p}{\partial x_i}$ calculated by the viscous loss term which contains viscous loss coefficient (α_i), dynamic viscosity (μ), local velocity in porous medium (w_i) and the inertia loss term containing an inertial loss coefficient (ζ_i) and the density (ρ) of the gas phase [5].

$$\frac{\partial p}{\partial x_i} = -\alpha_i \cdot \mu \cdot w_i - \zeta_i \cdot \frac{\rho}{2} \cdot |w| \cdot w_i \tag{4.27}$$

Using the Forchheimer pressure drop model requires measurement data of the porous material. By extracting a pressure drop curve (dependent on the flow velocity) it is possible to gain the porosity parameters ζ_i and α_i needed as input

parameters for the CFD calculation.

Tube Friction: The Tube friction pressure drop model is especially applicable for flow through a directed porosity in case that no measurements are available. The pressure gradient within the porosity is based on the wall friction occuring in a porosity channel. The tube friction equation 4.28 contains λ which is the laminar tube friction coefficient (λ_l) for laminar flows and the turbulent tube friction coefficient (λ_t) for turbulent flows divided by the hydraulic diameter (d_h) of a channel [5].

$$\frac{\partial p}{\partial x_i} = -\frac{\lambda}{d_h} \cdot \frac{\rho}{2} \cdot |w| \cdot w_i \tag{4.28}$$

In equation 4.29 the tube friction coefficients are listed.

$$\lambda_l = \varphi \frac{64}{Re_d} \qquad \lambda_t = \frac{0.316}{Re_d^{1/4}} \tag{4.29}$$

The shape factor (φ) for laminar tube friction is considered to be

- 1 for circular channel shape,
- 0.89 for quadratic and
- 0.83 for equilateral triangle channel shape

of the cross section area [5] [3].

Anisotropic conduction factor

The anisotropic conduction factor corrects the diffusion coefficients of the heat transfer equation of the porosity normal to axial direction in the way that the radial thermal conductivity is linearly linked to the axial solid thermal conductivity. The FIRE^{TM} aftertreatment manual suggests an anisotropic conduction factor of 0.5 for monoliths [3].

Turbulence in porous media

In directed porosities like catalytic converters the turbulence inside of the porosity is calculated differently from the rest of the flow area. The turbulence in a directed porous medium has to be "fixed".
The turbulence model that governs in porosities is based on the $k-\varepsilon$ model which is a popular two equation turbulence model.
In the case of fixed turbulence, only the variable k is derived from the Navier Stokes equations under the neglection of a damping influence of solid walls and the turbulent dissipation rate (ε_t) is calculated by equation 4.30. This is also described as a one equation turbulence model.

$$\varepsilon_t = C_\mu^{3/4} \cdot \frac{k^{3/2}}{C_{poro}} \tag{4.30}$$

C_{poro} is a turbulent length scale which estimates the turbulence characteristics inside the porous medium. It is an indicator of the size of the turbulent vortices and is constant [5]. C_{poro} has to be supplied by the user (similar size as boundary layer thickness δ [2]). Goal of turbulence modelling is the description of the turbulent viscosity μ_t (equation 4.31), which only depends on k and the constant C_{poro} in the case of porous media.

$$\mu_t = C_\mu \cdot \rho \cdot \frac{k^2}{\varepsilon} = C_\mu^{1/4} \cdot k^{1/2} \cdot \rho \cdot C_{poro} \tag{4.31}$$

In all other flow regions besides the porosities, the $k-\zeta-f$ turbulence model is applied. It is based on the two equation $k-\varepsilon$ model but takes into account the damping behaviour in the near wall regions. Furthermore, the turbulence is not treated isotropic as in the $k-\varepsilon$ model [4].

4.4.4 General Gas Phase Reactions

This model enables the calculation of chemical reaction in the gas phase of a fluid. Using this module requires the Species Transport module, too.
The heat produced or extracted during a chemical reaction represents a change of the source term in the Species Transport equations 4.13 and 4.15 and in the gas phase energy equation, depending on reaction rates, calculated by species concentrations and temperature. In FIRE^{TM} at the beginning of each timestep (Δt) a 0D

reactor model for each computational cell is solved, based on which the source terms for the Species Transport and enthalpy equation will be calculated.
For forward (f) reactions the reaction rate constant (k) is calculated by the Arrhenius equation 4.32 with the pre-exponential factor (A), temperature exponent (b) and the activation energy (E) (of reaction j) which are the input parameters in FIRE^{TM}.

$$k_{f_j} = A_j \cdot T^{b_j} \cdot exp(\frac{-E_j}{R \cdot T}) \tag{4.32}$$

For reversible reactions the backwards reaction rate constant is applied as the ratio of the forward reaction rate to the equilibrium constant in concentration units (K_c) which is obtained from the Gibbs free energy of formation at standard state (equation 4.33)

$$k_{rj} = \frac{k_{f_j}}{K_{cj}} \tag{4.33}$$

The source terms which are used in the conservation equations are listed in equation 4.34 for Species Transport and in 4.35 for energy equation.

$$S_k = \frac{\rho^{n+1} {M_k}^{n+1} - \rho^n {M_k}^n}{\Delta t} \cdot V_{cell} \tag{4.34}$$

$$S_h = \sum_{k=1}^{k_{gas}} \frac{S_k \cdot \Delta_B H_m(T_{ref})}{M_k} \tag{4.35}$$

4.4.5 Coupling of Domains

The FIRE^{TM} AVL Code Coupling Interface (ACCI) model enables the possibility of coupling two or more calculation regions, for example a fluid and a solid domain along a coupling interface. Each calculation case that participates in the coupling is named a client. The coupling interface is the geometric location where a set of values is exchanged between the clients. If the topology of the interface meshes of the two clients is not identical, an area weighted interpolation is performed automatically which is called 'Mapping'. A specific coupling model specifies the type of interface and the set of exchanged values. In the simulations of this work the wall heat transfer model is used (illustrated in 4.5) in which the heat transfer at contact surface is based on convection. This heat transfer model requires a convective heat transfer boundary condition on first client (fluid domain) coupling interface and

a temperature boundary condition on the second client (solid domain). The data exchange, namely of boundary condition values at the coupling interface, is done at definable timesteps or iterations [4].

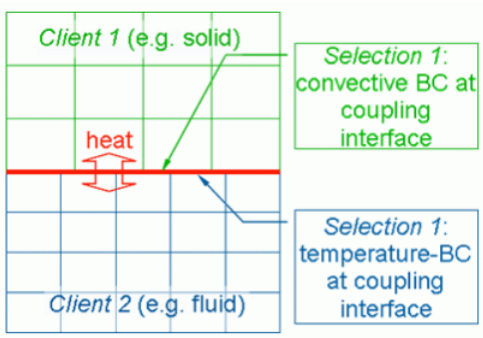

Figure 4.5: ACCI Coupling model wall heat transfer

5 Modelling of the System

5.1 Geometry

A cross section of the analyzed gas processing unit is illustrated in Figure 5.1.

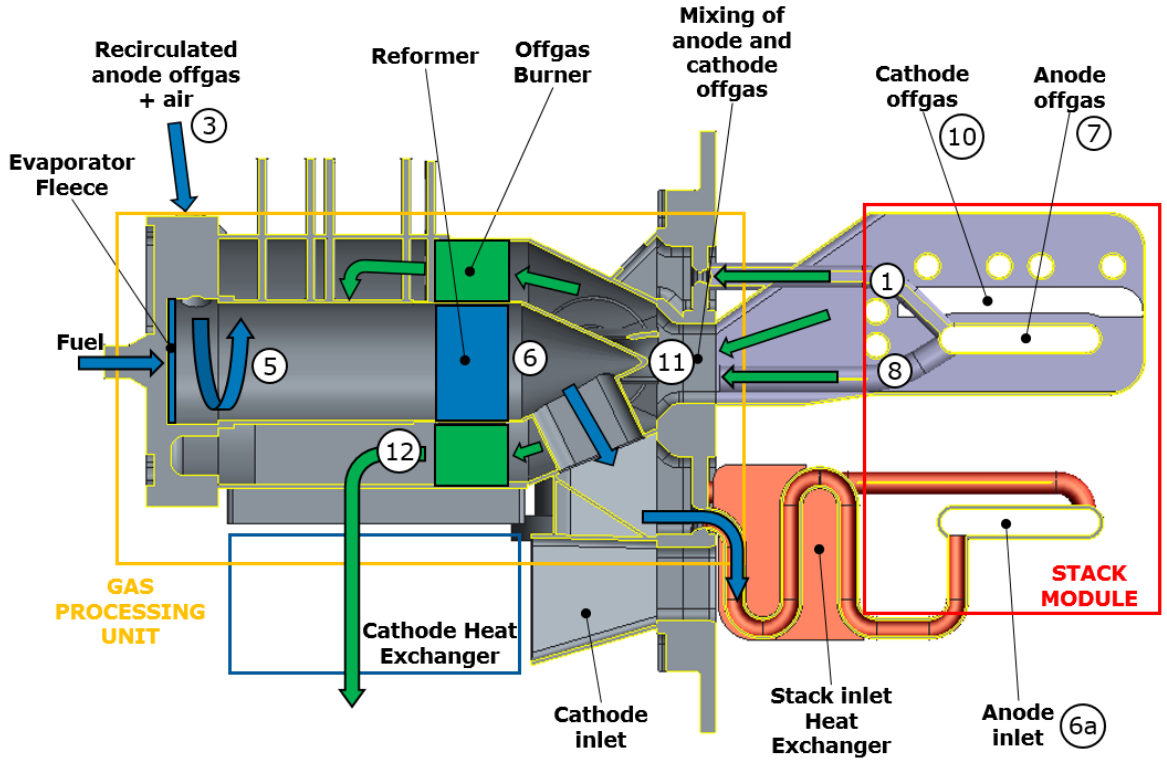

Figure 5.1: System setup of analysis model

The geometry includes the anode line containing the reformer and the evaporator and the exhaust line containing the mixing chamber where anode and cathode off-gas are merged, and the off-gas burner.
The evaporator fleece is located in the rear area of the geometry in the anode line.

Downstream the evaporator fleece, the introduced fuel gets in contact with recirculated anode off-gas, premixed with air (3), which enters the GPU through an eccentric inlet pipe. At point (5), which is the end of the evaporation area, the swirling gas mixture is heated by the exhaust line through the reformer pipe. A hydrogen-rich gas leaves the reformer catalyst at point (6) and enters the anode inlet of the stack module (6a) through the stack inlet HEX.
A part of the anode off-gas is recirculated (1) and the rest (8) is led into the mixing chamber (11) where the anode off-gas gets in contact with cathode off-gas (10). After the mixture, the exhaust gas enters the off-gas burner where it is purified by the oxidation catalyst (outlet point (12)). The heat from the hot exhaust gas is used for the air in the cathode line through the cathode HEX and to support evaporation and reforming in the anode line.
The starter burner pipe, which is connected to the mixing chamber, was also modelled to enable the possibility of simulating a startup operation which was not done in this thesis. The model was extended with the stack outlet pipes shown in Figure 5.1 at the right side in bright grey. This was done because the complex geometry of the 4 off-gas pipes (2 pipes lead to recirculation blower and 2 pipes into mixing chamber) may cause an uneven flowfield which may have an impact on the flow entering the the off-gas burner.
The cathode HEX was also modelled to describe the pressure drop in the exhaust path which has a major impact on flow uniformity. The solid housing was modelled to enable a heat transfer between hot exhaust line and cold anode line via ACCI coupling.

5.1.1 Preparatory Work

In order to facilitate the meshing process and to improve the convergence behaviour of the following calculations, the GPU assembly was cleaned from small edges and not needed contours. Transitions between different components were rounded with small radii. The reformer catalyst and the evaporator fleece in the anode line as well as the oxidation catalyst in the exhaust line were removed from the CAD model. After the polyhedron volume mesh was created, the cell topology in the areas of the catalysts and the cathode HEX was extruded in order to generate a structured mesh required for porous media. This extrusion is further described in 5.2.3.

5.2 Meshing

For flow and thermal calculation, the geometry has to be divided into a high number of control volumes which form a calculation grid (also: mesh). A 3D calculation grid can contain three main cell types: hexahedron, polyhedron and tetrahedron. In contrast to hexahedron cells, polyhedrons do not have a fixed topology, they have a more complex geometry consisting mostly of a higher number of corner points of each cell face. However, polyhedrons can be generated automatically and are flexible to use which is why they are applied especially to complex geometries. The number of computational cells should be as low as possible in order to reduce the calculation time and as high as necessary to get accurate results.
The mesh for the GPU was generated with AVL FAME^{TM}M polymesher (Version 2016©). It is an automated grid generator and enables simultaneous meshing of multiple domains like fluid and solid domain. In the present case, such a multidomain calculation grid is needed.
The workflow for meshing with a FAME^{TM}M starts with a well triangulated surface of the geometry in STL format which does not contain any identical nodes, intersections or holes. Adjusted to the surface mesh, an edge mesh must be provided to ensure that the resulting polyhedron mesh is following the contours which is illustrated in 5.2.

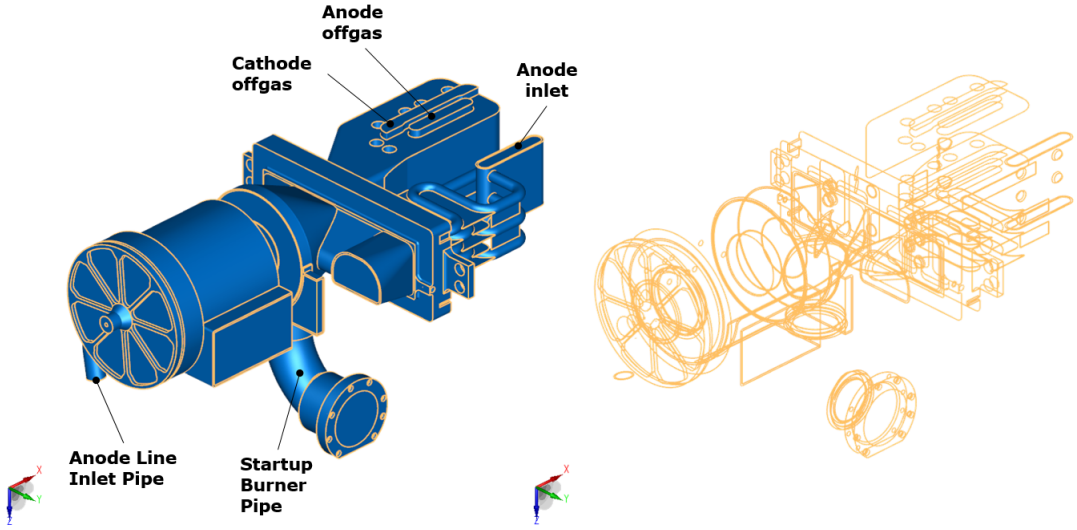

Figure 5.2: Surface and Edge Mesh of Analysis Model

5.2.1 General Mesh Settings

The meshing process starts with the surface mesh which cells have, approximately, the defined surface target cell size. Afterwards, the specified number of boundary cell layers with a certain thickness, a tetra volume mesh and finally, by use of a Delaunay triangulation, the polyhedron volume mesh is created. The general mesh settings for the gas processing unit geometry are shown in Table 5.1. The growth rate indicates the maximum size ratio of adjacent cells.

Table 5.1: General mesh settings

Property	Unit	Value
Surface Target Cell Size	mm	2
Volume Target Cell Size	mm	2
Auto Refinement	-	off
Surface Cell Growth Rate	-	1.2
Volume Cell Growth Rate	-	1.2
Number of Boundary Cells	-	2
Boundary Cell Thickness	mm	1
Boundary Cell Ratio	mm	1
Smoothing Variant	-	allegro
Decouple Multi-material Selections	-	unchecked

5.2.2 Refinements

Mesh refinements should be obtained in areas where high gradients are expected. In our case, refinements were made in the area of fuel injection (cell size 0.3 mm), the evaporator fleece (cell size 1 mm) and the stack inlet HEX (cell size 1.2mm). Also the porosities (reformer, oxidation catalyst and cathode HEX) have a smaller cell size of 1.5mm within.

5.2.3 Extrusion of Porosities and Boundaries

Because of the linear flow direction in the porosity channels, the mesh topology of the porosities has to be structured, which requires hexahedron cells. Hexahedrons

have the advantage of a low numerical diffusion in direction normal to the flow. Therefore, the mesh was extruded in this areas, namely the fuel fleece, reformer and off-gas burner catalysts and the cathode heat exchanger. The extrusion is illustrated in 5.3.

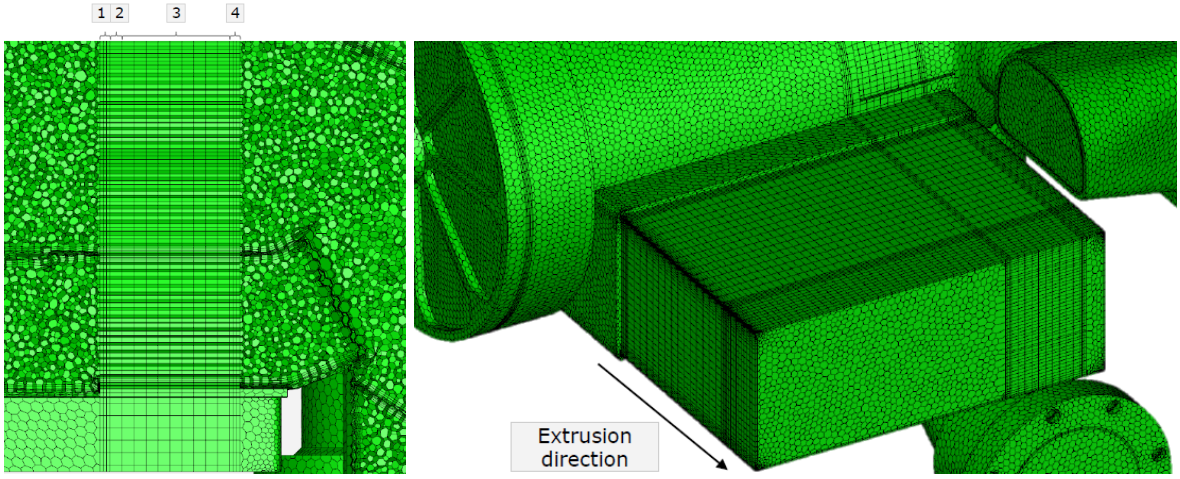

Figure 5.3: Extrusion of reformer and off-gas burner porosities (left) and cathode HEX porosity

The first three extrusion layers of each porosity were kept thin (1) because in this region a transition between channel flow in the porous medium and the adjacent 'free-flow' occurs. The following layers which represent the main porosity area, were made larger to keep the number of computational cells in the mesh low (2,3). The last three layer are, again, as thin as the first three extrusion layers to provide a smooth transition to the adjacent cells. An extrusion was also implemented at inlet and outlet boundary condition cross sections to ensure a well developed flowfield and a stable calculation. The extrusion can be seen in the final mesh in Figure 5.4.

5.2.4 Mesh Quality

At the end of the meshing process and the extrusion of porosity and inlet/outlet areas, a mesh check was made, which checks for cell quality, negative volumes, not connected areas and so on. Passing the mesh check is very important in order to have the best basis for a convergent calculation. As shown in Figure 5.4, the mesh consists of approximately 2.5 million cells, there are no negative volumes

or invalid connectivities and the geometrical requirements for computational cells were within the limits. Furthermore, the final mesh consists of approximately

- 2.34 million polyhedron cells,
- 140.000 hexahedrons and
- and 6.000 tetrahedrons.

The hexahedron cells are localized in the extruded elements explained in section 5.2.3. It is probable that the tetrahedron elements were made in areas where polyhedron elements could not be produced due to geometrical restrictions. It is known that tetra elements, mostly when located on edges, can cause convergence problems. Also [8] noticed a negative influence on the calculation results using tetrahedron elements. In this case, the tetrahedrons account for 0.24% which is a good result for an automatically generated mesh.

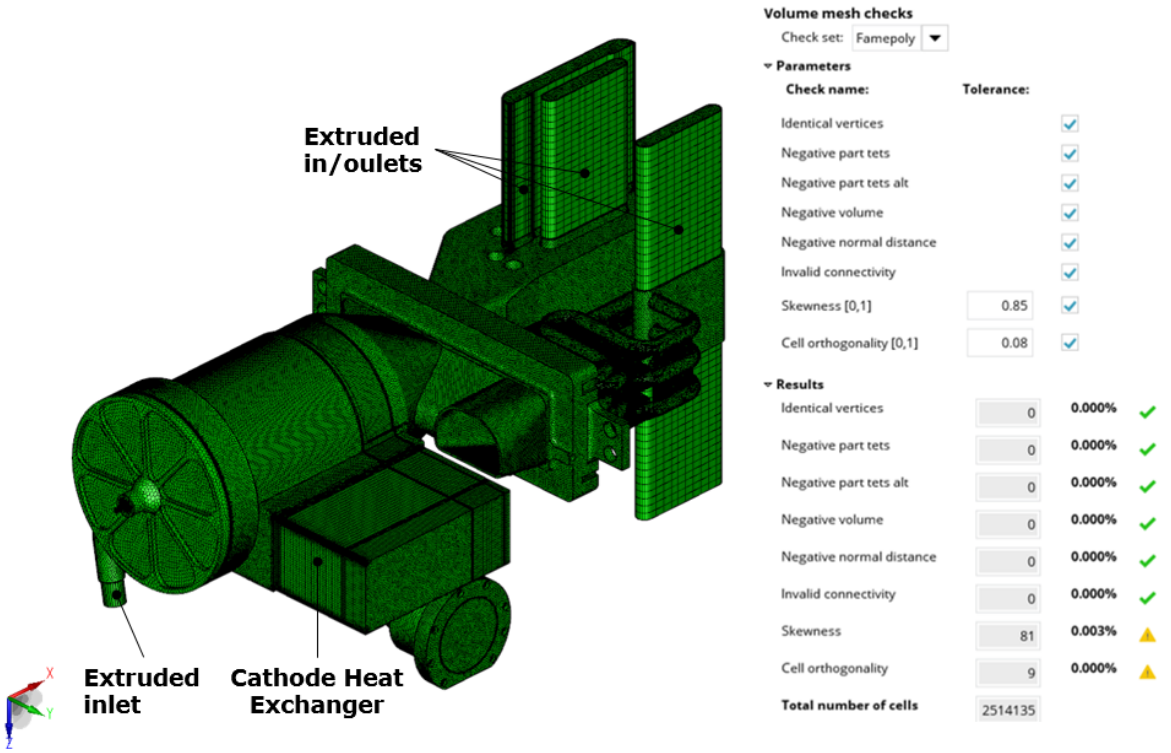

Figure 5.4: Final Mesh with Mesh Checks

5.3 Simulation

The performed simulations can be divided in two activities:

- method and parameter studies on simplified geometry
- global thermal field and heat flux assessment on full model

General simulation settings for both investigations are shown in Table 5.2.

Table 5.2: General simulation settings

FIRE^{TM} Version	2014.2
Module Activation	Aftertreatment
Module Activation	Species Transport
Turbulence Model	k-ζ-f
Two Stage Pressure Correction	SIMPLE PISO
Wall Treatment	Hybrid Wall Treatment
Heat Transfer Wall Model	Standard Wall Function
Underrelaxation Factor Energy	0.98
Boundary Condition Fluid Interface	Convective
Boundary Condition Solid Interface	Temperature

The simulations were carried out with the AVL CFD Simulation program (FIRE^{TM}) Version 2014.2 using FIRE^{TM} Aftertreatment Module to implement heat conductive porosities and Species Transport Module to take into account several different components in the gas mixture. Fluid and solid domain were coupled by their common interface. At this interface a defined set of heat transfer values using the ACCI coupling method was exchanged, explained in section 4.4.5. Therefore, a convective wall boundary condition was chosen on the fluid side of the interface and a temperature wall boundary condition on the solid side.

5.3.1 Parameter study on Simplified Model

In the AVL GPU the catalysts (modelled by porosities) are concentrically arranged and also axially aligned with each other, why the heat transfer normal to flow direction is of major importance. This new type of application was not considered

during initial software developement. Therefore, some parameter studies are performed to investigate the sensitivity on the modelling approach.
For this purpose, the porosity cells including the solid domain in between and at the outside of the exhaust line were extracted from the full model mesh. The inlet boundaries and outlet boundaries were linearly extruded, hence symmetric and uniform flow conditions can be established on both inlets. Afterwards, in order to analyze the heat transfer for this special case of a circular porosity (reformer) around a second porosity (off-gas burner), some test calculations were performed preventing the correct physical properties of both catalysts and counterflow concept.
In Figure 5.5 there is a geometry overview including the boundary conditions at the inlets and outlets of the geometrical simplified model.

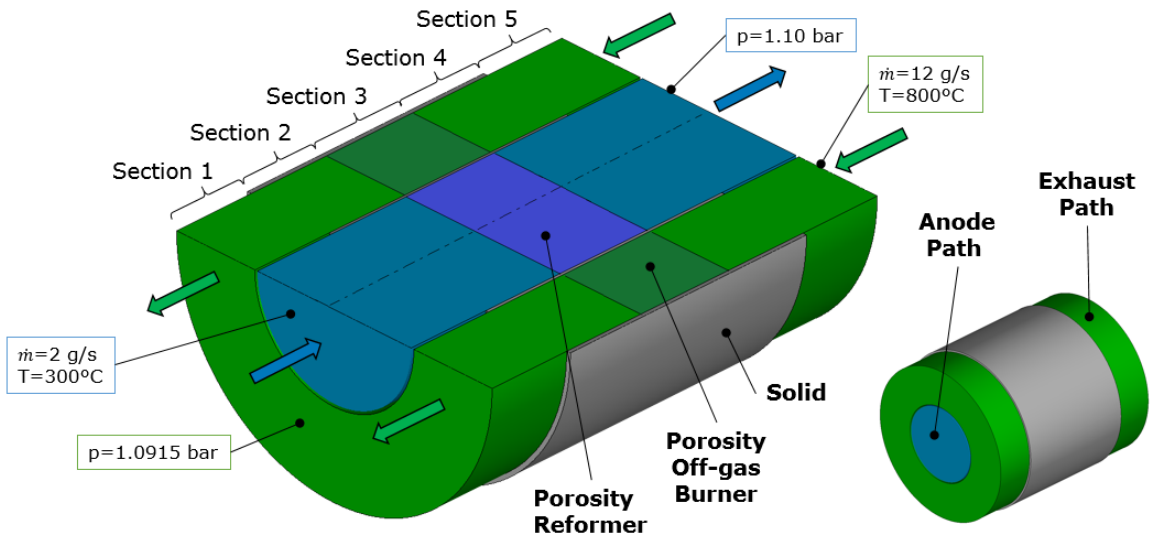

Figure 5.5: Simplified model - geometry and boundary conditions

On the simplified model the influence of two major aspects are to be investigated:

- The influence of a fluid gap between catalyst and pipe versus direct coupling
- The influence of the boundary cell mesh resolution

General settings of the calculations are listed in Table 5.2. Changing parameters regarding the simplified model can seen in Table 5.3.

Table 5.3: Changing parameters of simpified model investigation

Case Number	Boundary Cell Thickness	Gap between Porosity and Solid
01	2 layers a 0.5 mm	no
02	2 layers a 0.1 mm	no
03	2 layers a 0.5 mm	yes
04	2 layers a 0.1 mm	yes

Within the framework of the simplified model investigation the energy balance was evaluated along five sections illustrated in Figure 5.5.

Section 1: In section 1 there is no interaction between anode path and exhaust path because there is no solid pipe wall in between. The outer walls of anode and exhaust path in section 1 are separated and treated as adiabatic walls. Section 5 is equally setup as section 1.

Section 2: In section 2 there is a solid pipe wall between the two paths which leads to a heat exchange between hot and cold path through the solid material. Section 4 follows the same principle as section 2.

Section 3: Section 3 represents the most interesting section containing two porous media which exchange heat through the solid material which is in between.
The mass flows were chosen in relation to the full model of the gas processing unit and uniformly distributed over the cross section. The temperature difference between anode and exhaust line was made intentionally large to increase the heat exchange.

Motivation for parameter study

The parameter study was performed because it is not clear if the interface between porosity and solid transfers heat in a correct way. Until now, the main applications for CFD calculations containing heat conducting porosities were aftertreatment studies from where the heat transfer in radial direction was not of interest

but rather the species conversion and heat release of single or series-connected reactors. In these previous works, for instance, extremely low y^+ at porosity/wall interfaces and also non-reliable heat transfer coefficients were observed. Also because another turbulence approach is governs in the porous medium, an inaccuracy of the transferred heat is expected. In some cases, therefore, the porosity was decoupled from the wall by a fluid gap to circumvent these effects.
Therefore and, as already explained before, in these parameter study calculations, the porosities were both coupled to the wall and decoupled from the wall to determine the insulation effects of such a gas gap.
Furthermore, different mesh resolutions were analyzed in order to evaluate the mesh independence of the results.

5.3.2 Gas Processing Unit

The Gas Processing Unit investigation was performed as two different multi-domain ACCI coupling calculations on same simulation mesh which are

- a steady simulation to reach stationary conditions and
- a transient simulation in order of considering gas-phase reactions.

The transient simulation was applied, utilizing the converged results from the steady simulation, due to the fact that the gas-phase reaction steps require a temporal resolution. The timestep therefore was chosen between 0.001 and 0.005 seconds. The calculation was evaluated after an achieved time of 10 seconds which took about 400h of calculation time with the use of 45 CPUs .
An overview of the gas processing unit mesh and the boundary conditions of the calculation can be seen in Figure 5.6 where only the lower half of the solid domain is shown. At the left side the anode line including the reformer porosity is illustrated. The gas composition in the anode line was held constant through the full flow domain, which means that the respective species mole fractions at the anode line inlet are the same as for the anode line outlet. At the inlet, massflow and temperature was applied, and at the outlet a static pressure boundary condition. The data was extracted from measurement results and therefore based on calculations (see chapter 3).

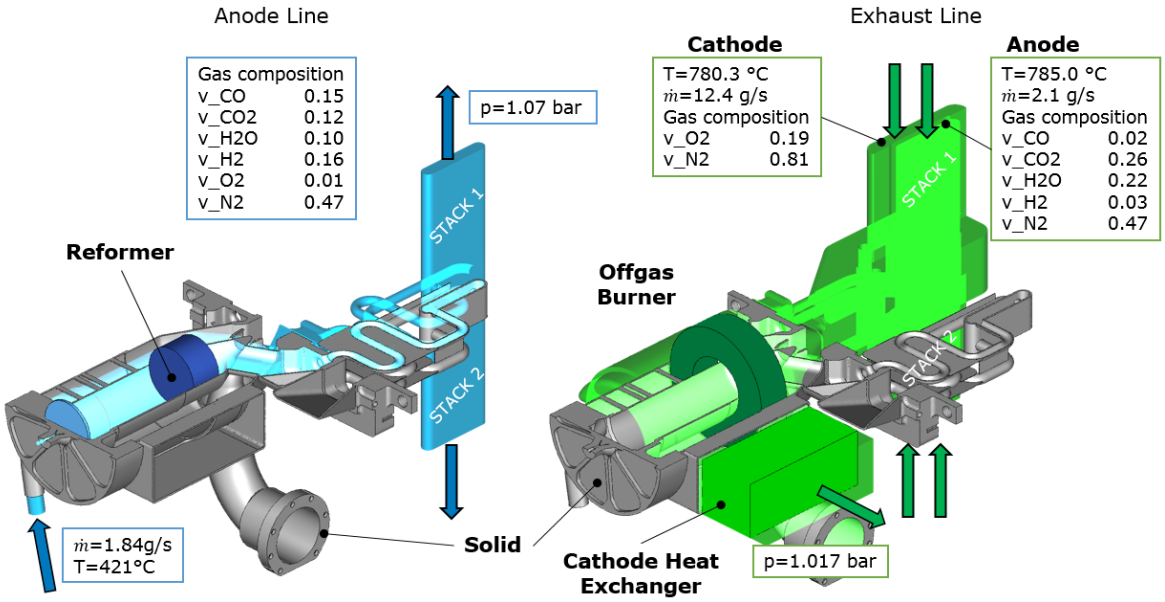

Figure 5.6: GPU - geometry and boundary conditions for anode line (left) and exhaust line (right)

Evaporation

The endothermic phase transition which occurs during the evaporation process of diesel fuel was not considered in this simulation. As an alternative a volumetric heat sink between the anode line inlet pipe and the begin of the reformer pipe was applied. The gaseous and reformed fuel was considered in the prescribed gas composition at anode line inlet. Therefore, no massflow was applied to the fuel injection inlet, located in the rear GPU housing prior to the evaporation fleece.
According to equation 4.6, a heat flux was calculated taking into account a ΔT of 12 °C (according to measurement results 3.3). Because of an introduced heat from the solid domain via heat conduction in the simulation, the volumetric heat sink was adapted in several calculation loops until the evaporation outlet temperature of 409°C according to the measurement was reached. The value of this heat sink was then 85W.
The evaporation fleece was treated as a porosity using the Forchheimer parameters ζ_i = 222 1/m and α_i = 5.1E+05 1/m². The parameters were extracted from an AVL internal database.

Reformer

The reformer was treated as a heat conducting aftertreatment porosity as discussed in section 4.4.3.
Because of no available measurement data of this component, the tube friction model was chosen as pressure drop model. Because of the quadratic shape of the monolith channels, a shape factor φ of 0.89 was chosen according to chapter 4.4.3. For the turbulent length scale of porous media C_{poro} was chosen 0.0001.
Specific catalyst and material data was provided by the supplier and by internal data sources. The reformer used in the simulation as well as in the measurement is made out of Cordierite, the specifications can be found in the appendix section B.2. As anisotropic conduction factor the FIRE^{TM} suggested value of 0.5 for monoliths (see section 4.4.3) was used. To reconstruct the heat release observed in the reformer in the measurement, a volumetric heat source formula was implemented to the reformer porosity. The amount of heat of reaction was provided by a preceding 1D matlab simulation (section 3.4) which gave 1009W.
As already mentioned, the gas composition was conserved through the whole anode line, thus also the gas composition between reformer inlet and reformer outlet did not change. This simplification was made due to high complexity of catalytic reaction and severe calibration efforts beyond of the scope of the focus of this thesis on thermal aspects.

Off-gas burner

Similar to the reformer porosity, also the porosity of the off-gas burner was handled as a heat conducting aftertreatment porosity which follows the tube friction pressure drop model.
The off-gas burner has a metallic carrier material and its channels have a triangular form. Therefore, a φ of 0.83 and a C_{poro} of 0.0001 was applied. The specifications are documented in the appendix B.2. For taking into account a reduced thermal conductivity within the porosity in radial direction, a value of 0.5 was chosen as an anisotropic conduction factor.
In contrast to the reformer porosity, a chemical reaction scheme based on the Langmuir-Hinshelwood approach (section 2.3.3) was implemented. The reaction parameters to solve the reaction rate located in the source term of the energy con-

servation equation is shown in Figure 5.7 and were extracted from an internal aftertreatment database. The reaction scheme considers an oxidation of H_2 as well as an oxidation of CO.

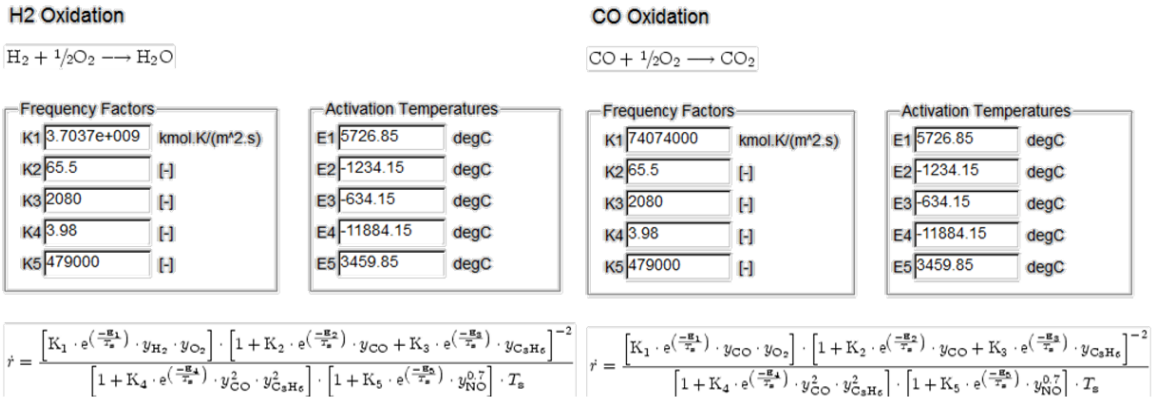

Figure 5.7: Frequency factors and activation temperatures for H_2 and CO oxidation

Cathode Heat Exchanger

The cathode Heat Exchanger is located in the exhaust line downstream of the off-gas burner and is modelled as a porosity without the ability of conducting heat, because the cathode line was not given consideration within the scope of this thesis. Special interest is therefore given to the pressure drop and effect on the flow distribution upstream. The pressure drop was modelled by the Forchheimer approach. The pressure drop parameters according Forchheimer were determined according to the measured stack outlet pressure and the assumed exhaust line outlet pressure. By several iteration loops, an inertial loss coefficient (ζ_i) of 4200 1/m and a viscous loss coefficient (α_i) of 10000 was applied to the cathode HEX volume.

Mixing Zone

The mixing chamber before the off-gas burner was modelled as flow domain including a deposited reaction scheme. The reaction scheme contains chain start reactions of the spezies H_2, CO and O_2. Regarding the chain propagation, the chemical species OH, HO_2, HCO, H_2O_2 and H_2O were considered. The reaction

scheme was derived from [26]. The, in comparison to other reaction schemes, relatively small detailed chemical kinetic mechanism for the combustion of hydrogen and carbon monoxide has been already tested for autoignition and extinction of diffusion flames and of partially premixed flames. By keeping the number of reactions steps low, it is possible to reduce the calculation time. In addition, to reduce calculation time, the multi-zone model for chemistry clustering was switched on. The complete chemical kinetic mechanism applied to the mixing chamber of the exhaust line can be found in the appendix Figure A.6.

Housing

The solid domain in the simulation is the housing of the Gas Processing Unit as well as the intermediate element between anode line and exhaust line in order to transfer heat between hot exhaust line and cold anode line. The solid is made of a non-corrosive material, which has a good resistance against oxidation at high temperatures, namely the high temperature steel X15CrNiSi25-21 (1.4841). In addition, 1.4841 shows good strength behaviour at high temperatures and is chemically stable until a temperature of 1100°C [9] [31]. Material properties of 1.4841 can be found in the appendix A.1. In the simulation, constant material properties (λ, c_p and ρ) at an expected average solid temperature of 700 °C were used.

6 Discussion of the Results

6.1 Simplified Model

The results of the investigation with the simplified model are discussed in this chapter. The four cases which were analyzed, are illustrated in 6.1.

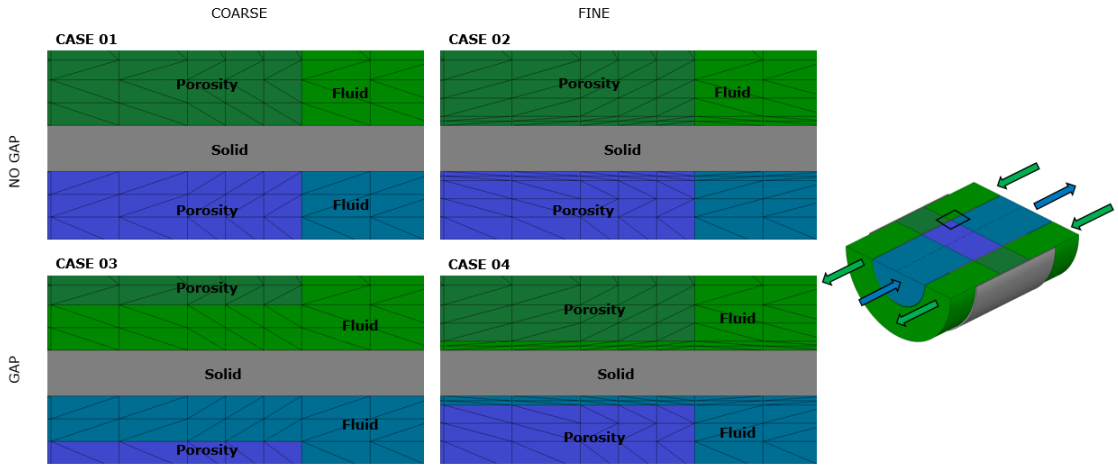

Figure 6.1: Topology details of cases of simplified model

To directly compare the four test calculations with each other, the results of each case are shown in one picture. While in the left-hand column (case 01 and 03) there are always illustrated the cases with the coarse mesh in the boundary region, in the right-hand column (case 02 and 04), the mesh in boundary layer region is finer. The two pictures in the first line (01 and 02) represent the cases where the porosity is aligning with the solid wall at the fluid/solid interface. In the second line (03 and 04) there are the cases where a gap between porosity and solid wall was implemented.

6.1.1 Convergence Check

The convergence of the simulation is evaluated with the normalized residuals. If the residual, in other words, the numerical error becomes smaller than the convergence criteria during the calculation, the solution is defined as converged. In Figure 6.2 the residuals of the four cases of the simplified model investigation are plotted. U, V and W represent the residuals for the momentum equation in the respective directions x, y and z. The variable K stands for the turbulent kinetic energy, D for the turbulent dissipation, M for the continuity equation and H is the residual for the energy equation.

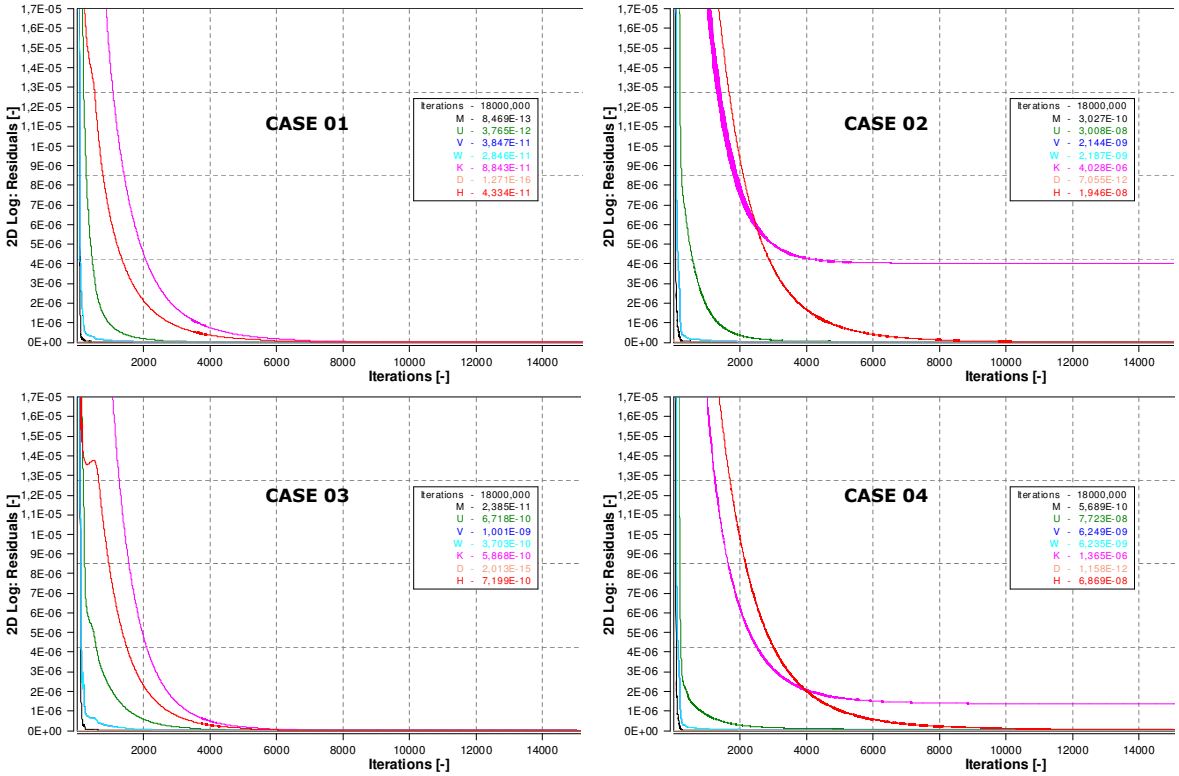

Figure 6.2: Convergence plot of simplified model calculations

All the residuals are below a value of 10^{-5} which is sufficient low and indicates a very good convergence.

6.1.2 Flow Results

Velocity Field

In Figure 6.3 the velocity distribution of the four calculation cases described in 5.3 is illustrated in a range of 0 m/s to 8 m/s. A general similarity between case 01 and case 02 can be seen. These velocity fields give an indication of the independence of the grid resolution in the near wall area. Therefore, no further refinement of the boundary layer mesh is necessary. Remarkable is the velocity field of case 03 in the

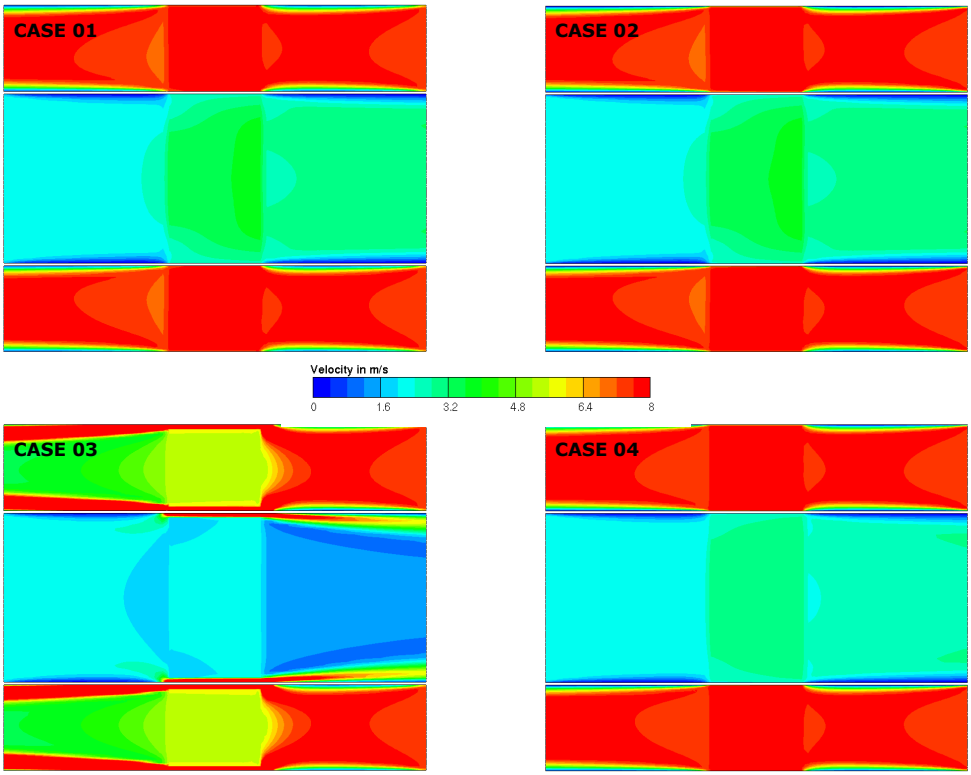

Figure 6.3: Velocity field of simplified model calculations

bottom left corner. An extremely high velocity was observed in the gap between porosity and solid wall. This is because the fluid takes the path of least resistance in the big gap and avoids the path through the porosity. This effect can be seen at both sides, the reformer porosity as well as the off-gas burner porosity. The big gap causing such an unrealistic high velocity gradient in the boundary layer

does actually not exist in reality. Therefore this case can be excluded from a more detailed analysis.
The case with a gap between porosity and solid wall but with finer cells in the near-wall area (04) shows a similar velocity field to the reference case 01 without gap. It seems that the gap size is small enough to avoid a high velocity gap flow as seen in case 03. However, there is a by-pass to the porosity and the overall velocity in the porosities is lower than in the reference case.

Temperature Field

The temperature field of the four cases is showed in Figure 6.4.

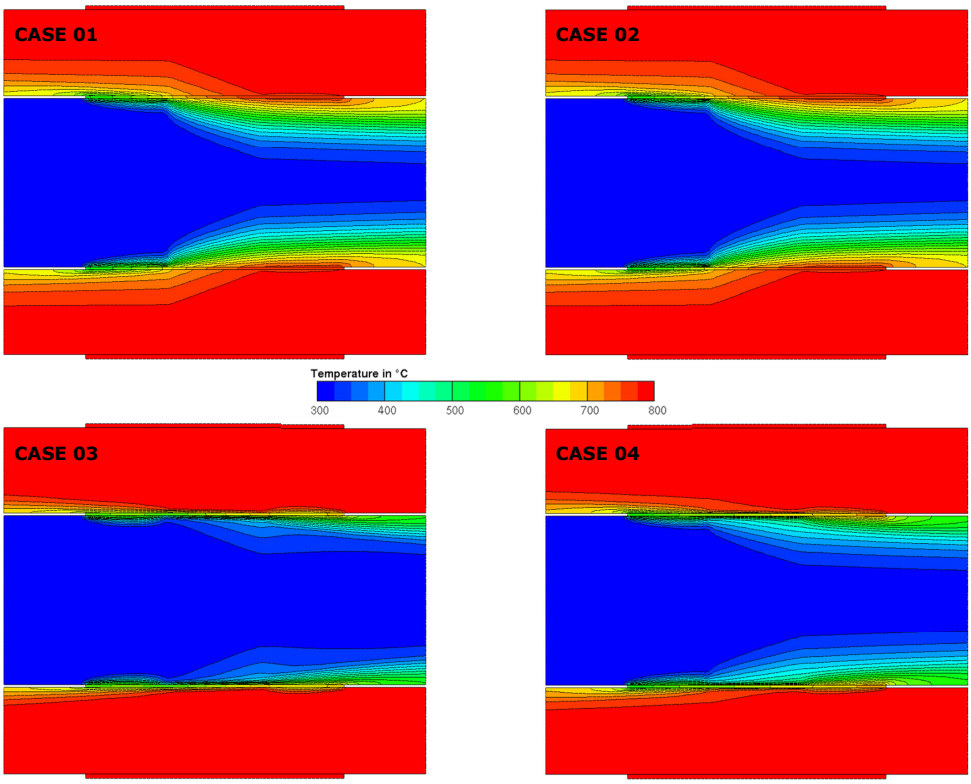

Figure 6.4: Temperature field of simplified model calculations

In general, in all cases, the highest temperature gradients were observed in the porosity itself. This effect can be explained by the increased thermal conductivity

because of the heat conducting characteristics of the aftertreament porosity.
Comparing the cases 01 and 02 without gap between porosity and solid wall first, it is detected that the temperature fields are, as already seen in the velocity fields above, very similar to each other. This indicates an unindependency of the grid resolution in the near wall region.
Compared to that, the temperatures in the cases with a gap between porosity and solid wall (case 03 and 04) are lower as in the cases without gap. The inferface seems to conduct much less heat. This may arise due to an insulating effect of the gas stream in the channel between porosity and solid. The thermal conductivity in radial direction of the porosity solid part is about 10W/mK in the off-gas burner (because of an anisotropic conduction factor of 0.5) and about 2W/mK in the ceramic reformer. The λ of the gas mixture does not exceed 0.21W/mK. Therefore, the gas gap, acts like an insulating layer.
The temperatures in case 03 are generally lower than in case 04 (with thinner gas gap) which can also come from the higher insulation effect of the faster and thicker gap flow.

6.1.3 Near-wall results

The flow and heat transfer conditions were analyzed in the near wall zone to get information about the interaction of the different domains fluid, porous medium and solid wall.

Temperature and velocity

In Figure 6.5 the radial distribution of velocity and temperature are plotted on the center cross section surface of the reformer porosity.
The length scale on the x-axis gives the distance from the wall. The scale of this distance indicates a higher value (above 60 mm) in the cases with the finer mesh, which can be explained by a different location of the evaluated cell center.
However, the respective wall temperatures of case 01 (730.09 °C) and 02 (730.4 °C) fit well to each other and also the temperatures of the core flow. The velocity in the center of the reformer porosity is 3.58 m/s in case 01 and 3.59 m/s in case 02.
The results of the cases without gap between porosity and solid wall (in the first line) agree well. The difference lies in a smoother transition from boundary area

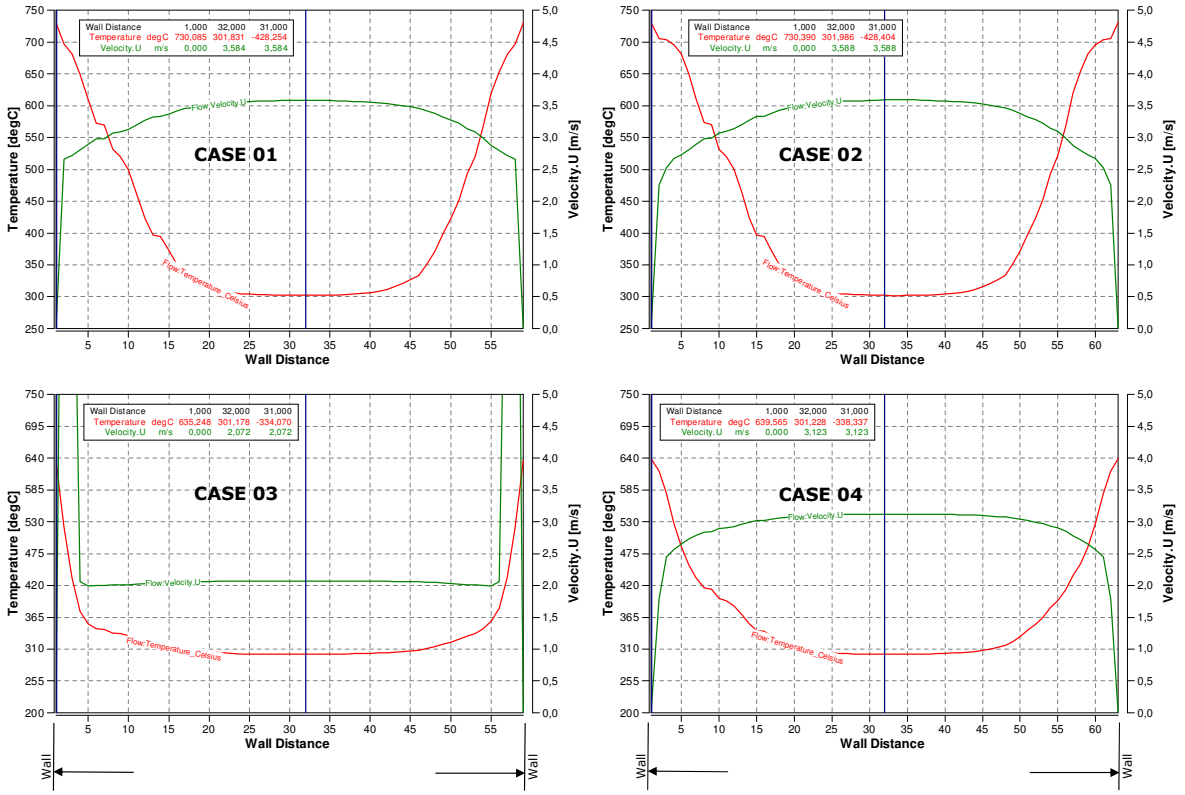

Figure 6.5: Temperature and velocity distribution along reformer middle plane

towards core flow in the case of the finer mesh. This is because each data point for the graphs was obtained at the computational cell center, so there were less data points in the case with coarser mesh and therefore an unsmooth curve results.
The velocity curve close to the wall of case 03 is again different from the other cases because of the relatively big gap size between porosity and wall. This has a large impact on the velocity distribution along the whole porosity cross section. The velocity in porosity center is only 2.07 m/s compared to about 3.6 m/s in the cases without gap. Also the wall temperature is about 95 °C lower than in the cases discussed before.
Case 04 represents a similar flow and temperature field along the reformer cross section. The transition between wall and core flow is again smoother because of the higher cell resolution in the wall area. What is remarkable is that the velocity in the core flow is about 12 % lower than in the cases without gap. Also the wall

temperature is significantly smaller and with a temperature difference of 90°C to the cases without gap comparable to the temperature field of case 03. Even though the high velocity effect which was observed in case 03 in the wall area is not existing here, the insulating effect of the gap is dominant.

Dimensionless distance to the wall

In Figure 6.6 the dimensionless wall distance (y^+) is shown on the interface between fluid and solid. This interface consists of Section 2 (interface Fluid/solid), Section 3 (interface porosity/solid) and Section 4 (interface fluid/solid) which can bee seen in 5.5.

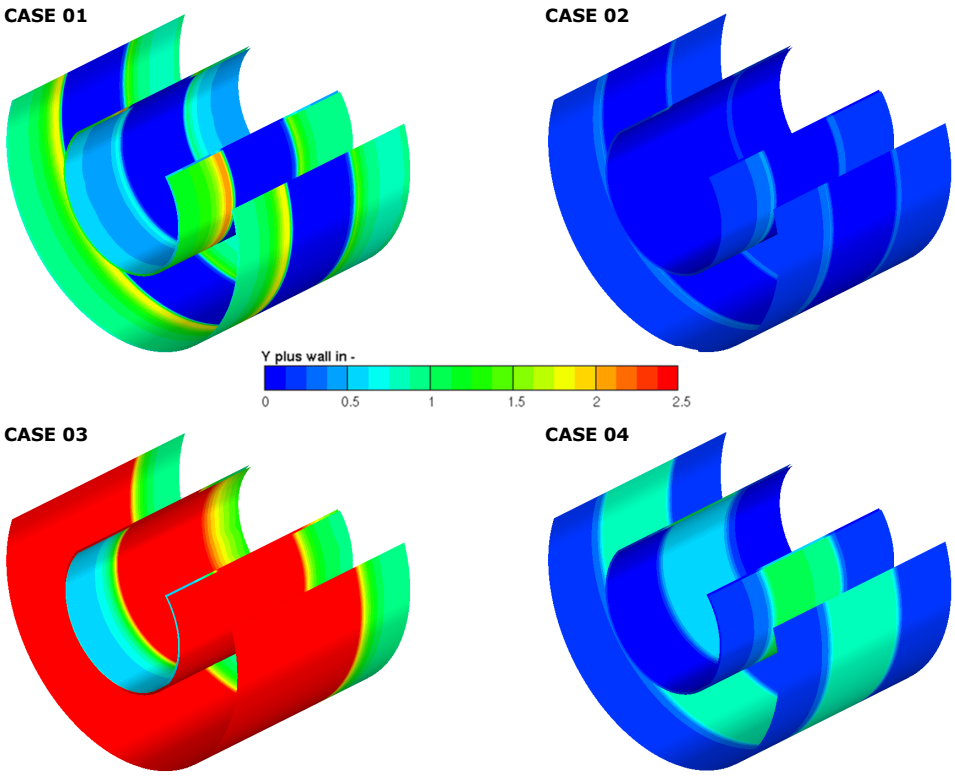

Figure 6.6: Y^+ applied onto the fluid/solid interface

A difference in the y^+ values for each case can be seen. It is observed that the y^+

is extremely low at the interface porosity/solid when the porosity is touching the solid wall. Values for y^+ on the interface reformer porosity/solid for case 01 are 0.02 and for case 02 with finer mesh 0.003.
Of course, dimensionless wall distances are lower in case of finer mesh near the wall. With the implementation of a gap between porosity and solid, the y^+ increases (in case 03: 3.66 and in case 04: 0.51). The highest values for y^+ can be seen in case 03, where the velocity is high in the near wall region because of the large gap between porosity and wall. Therefore, the y^+ of, for instance, 4.95 between off-gas burner porosity and wall, indicates a flow, which is between viscious sublayer and buffer layer according to Figure 4.2.
Comparing the cases of finer boundary layer resolution with each other shows that in section 2 and 4 (interface fluid/solid) no difference is detected as in section 3 (porosity/solid). In the anode line in the area of the reformer porosity, a face-averaged y^+s of 0.51 for case 04 and 0.003 for case 02 can be identified. This phenomenon can be attributed to the different turbulence models in the porosity and the rest of the flow domain as explained in 4.4.3.
The implementation of a gap between porosity and wall allows the usage of the $k-\zeta-f$ turbulence model in the gap flow which is more accurate. By an alignement between porosity and wall, the turbulence is governed by the turbulent length scale. As it is to see on the small y^+, in the case of the one equation turbulence model (governing in the porosity) the flow turns into strongly laminar.
The Reynolds number for a channel of the reformer catalyst is, for instance, shown in equation 6.1 which represents a laminar flow. Therefore, the turbulence approach in the porosity is approved for this application.

$$Re_d = \frac{u \cdot d_h \cdot \rho}{\mu} = \frac{3.58m/s \cdot 1.1 \cdot 10^{-3}m \cdot 0.3kg/m^3}{3.5 \cdot 10^{-05}kg/ms} = 39 \tag{6.1}$$

Convection Heat Transfer Coefficient

Analyzing the near wall results of convection heat transfer coefficient (α) in section 3 (porosity/solid), a direct connection to the dimensionless wall distance can be observed. Very high heat transfer coefficients arise only in the cases 01 and 02, as shown in Figure 6.7.
Due to consideration of metal (off-gas burner) and ceramic (reformer) conduction

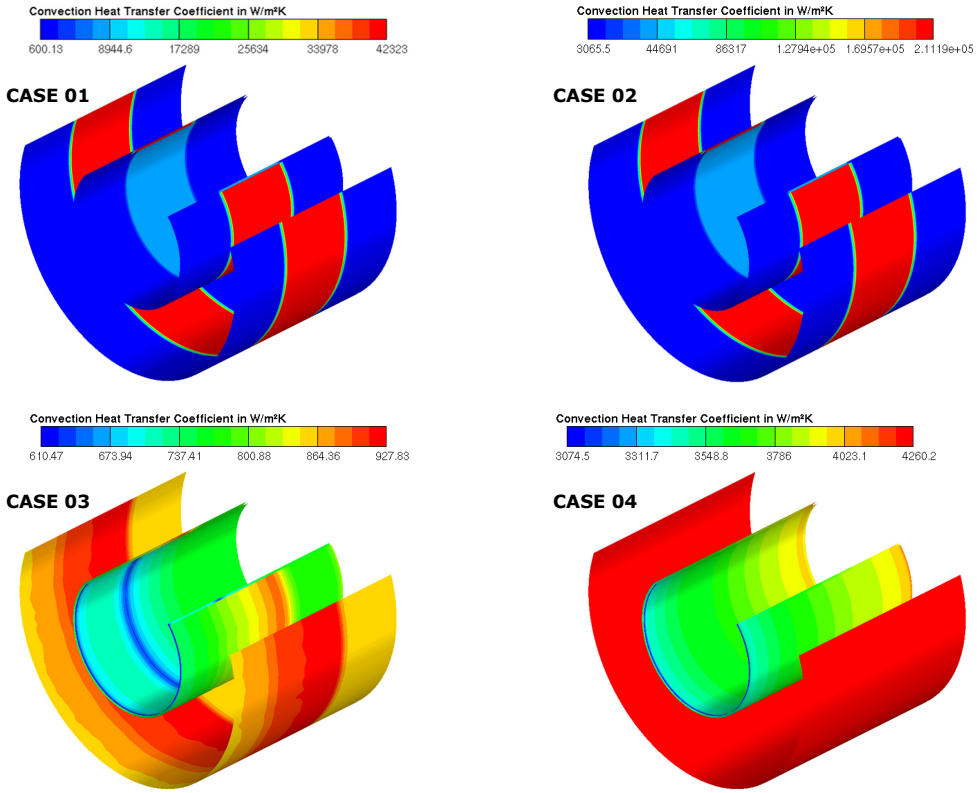

Figure 6.7: Convective heat transfer coefficient applied onto the fluid/solid interface

effect in the heat transfer of porous media cells, the derived "convective heat transfer coefficient (α)" in porous regions show very high values which seems of, but actually can not be directly compared to pure fluid cell layers without additional conduction.

The cases without gap between porosity and solid show an extremely high heat transfer coefficient, especially at the case with the finer boundary layer mesh. In general, the lower the y^+ is, the higher the α becomes. The magnitude of α is more credible when the porosity is decoupled from the wall (case 03 and 04) because the cell center is on a closer distance to the wall and deeper within the boundary sublayer. Differences between finer and coarser boundary mesh can be seen, because the temperature difference from cell to cell is smaller when the cells are smaller, so the α increases.

The Standard Wall Function (section 4.4.2) is used in these CFD calculations. As

shown in equation 4.24, the heat transfer coefficient is directly related to the dimensionless wall distance. It is obvious that the 3D result heat transfer coefficient can not be used in following calculations, also due to an uncertainty concerning how the α is calculated in the FIRE^{TM} porosity. Therefore, it is recommended to calculate the α according to equation 4.9.

Convective Wall Heatflux

The results of wall heat flux density $\dot{q}_w$ are given in Figure 6.8.

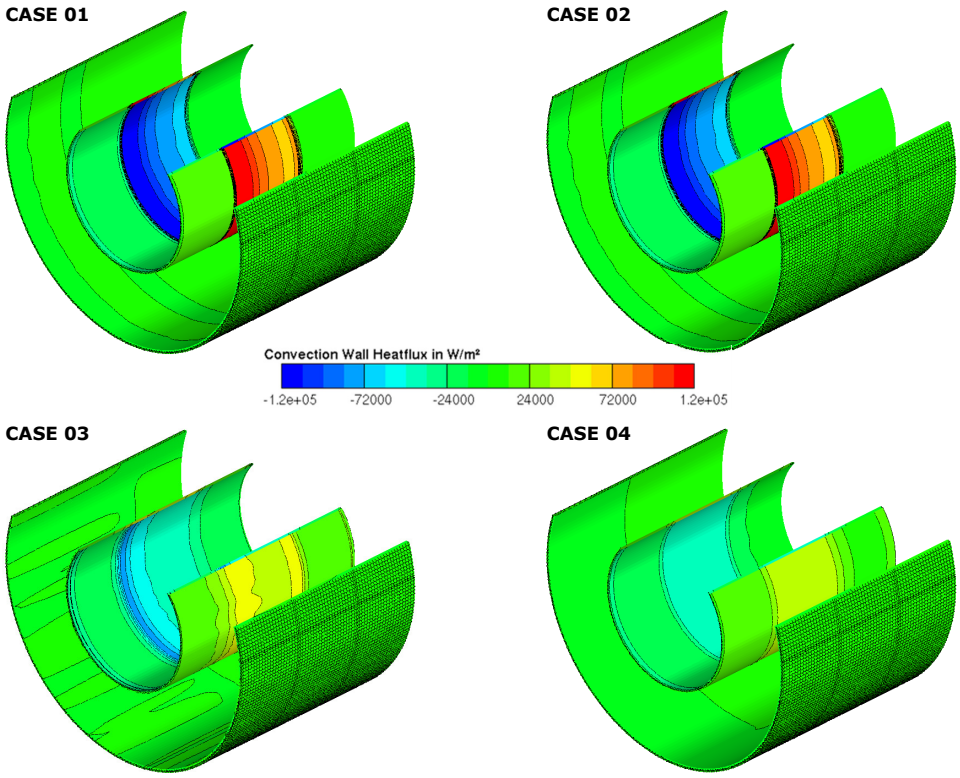

Figure 6.8: Convection wall heat flux applied onto the fluid/solid interface

There is an obvious connection between the cases without decoupled porosity from the wall (01 and 02) and the cases with gap in between (03 and 04). The heat flux density at the walls before and after porosity is more or less the same in all cases, so that these walls were not examined further.

As already noticed at the temperature distribution in section 6.1.2, the cases without gap between porosity and solid fit well to each other, also regarding the heat flux density distribution. There is a difference of about 5 W which was detected at the interface reformer porosity/solid which means a maximum deviation of 0.7 %. The heat flux ($\dot{Q}$) which is transferred from the solid to the reformer porosity in case 01 is about 646 W.
In contrast, the cases where porous medium and solid are decoupled from each other by a gas gap, the heat flux density is much lower in section 3(porosity/solid). Values for $\dot{Q}$ from the solid to the reformer porosity are 277 W for case 03 and 337 W for case 04 with finer mesh. This reduction of the wall heat flux by nearly a half in comparison to the cases without gap, is caused by the insulating effect of the gap and thus the reduced thermal conductivity between porosity and solid.

6.1.4 Energy Balance

Furthermore, at the end of the investigation of the simplified model, an analysis of the energy balance was performed. Therefore the geometry of the simplified model was divided into several sections within which information about heat flux, temperature, specific heat capacity at $p = \text{const.}$ and specific enthalpy were collected. The sections 1 to 5 which are explained in Figure 5.5 are evaluated in more detail regarding heat transfer through the walls and convective heat transfer of the fluid. The area specific values were derived after the calculation was finished using formulas as attached in the appendix (C).
Regarding energy balance, the case with coarser boundary layer and aligned porosity/solid interface (case 01) and the case with finer mesh and gap between porosity and wall (case 04) receive special attention, because of unrealistic results of case 03 and because of the similarity between case 01 and case 02.

Case 01

The energy balance result for case 01 is shown in Figure 6.9, more precisely, a temperature plot where values for both, convective heat flux and wall heat flux are given.
At first sight, energy is well balanced. The overall gain of heat in the cold path correlates with the overall introduced wall heat flux into the cold path. The same

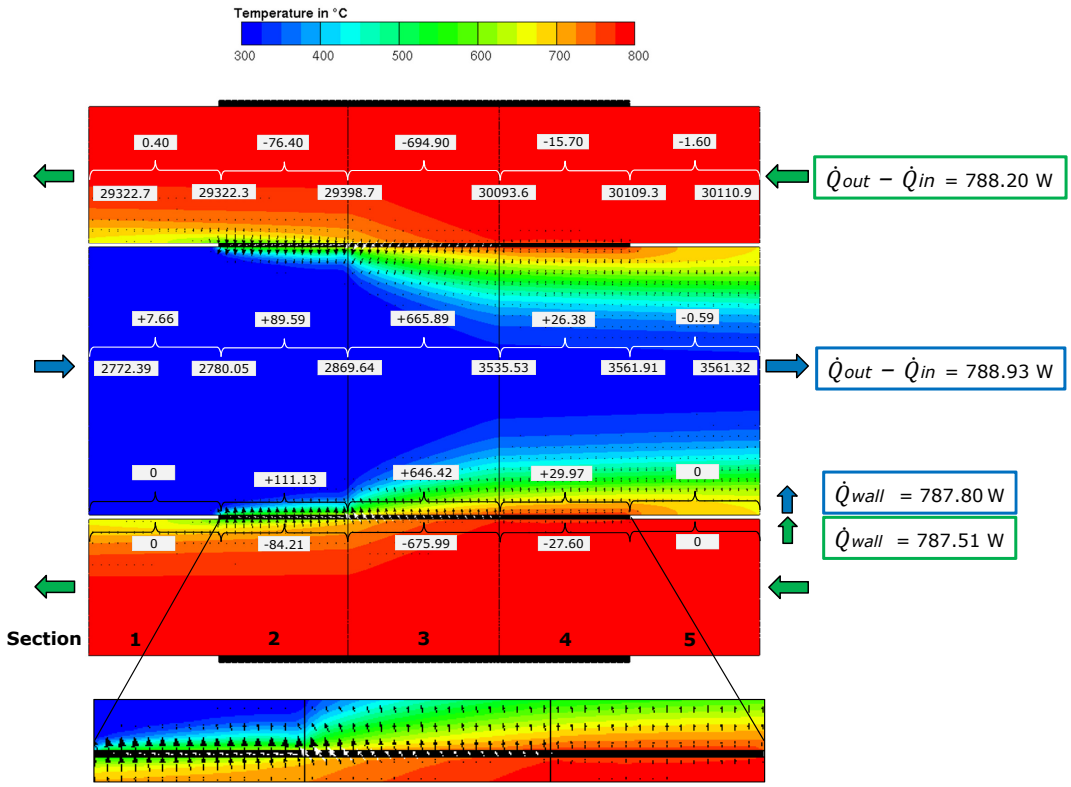

Figure 6.9: Temperature distribution with energy balance of Case 01

applies for the hot path which releases the same amout of heat which is transported to the cold path. The maximum deviation of heat flux found in the cold path where 1.13W were introduced more into the fluid than transferred through the solid which means a very satisfying deviation of 0.1%.
The adiabatic wall boundary condition of section 1 and section 5 should disable any heat transfer. It can be seen in the results of section 1 and 5 that 0W is transferred either from the hot path to the solid or from the solid to the cold path. However, in these regions from inlet/outlet cross section to the cross section, where the coupling with the solid begins, a small change in convective heat flux was observed. This may result from the heat transfer which can be seen at the edge of the solid geometry towards the flow domain right at the begin of section 2. The same applies for the other side, examining section 5.
From the point where fluid path and solid domain are coupled, heat transfer is not-

icable. In section 2, an enthalpy increase of about 90W takes place in the cold flow domain. In comparison to the porosity section 3, the heat input is much higher at 666 W. This can be explained by to the thermal conductivity of the porosity being about 10 times higher than the thermal conductivity of the gas mixture in radial direction.
After section 3 which includes the porosity, there is again a section where hot and cold path are connected via a heat conductive solid section (section 4). Here, a similar heat conductivity as in section 2 can be observed, although the heat input to the cold path and the heat release in the hot path is lower than in section 2. This is due to a lower temperature difference between hot and cold path in this area.
Comparing each section independently, one can see that heat release, heat conduction and heat input do not always correlate. For instance, in section 1, a heat flux of 84 W was conducted from the hot fluid path to the wall but almost 111 W were conducted from the wall again into the cold path. The enthalpy flux in the cold path was increased by the amount of 90W and in the hot path decreased by 76 W. These differences in heat flux are caused by an axial heat flux in the wall. This can be determined based on the white inclined heat flux arrows in Picture 6.9. Especially at the transition zone from section 2 to section 3 a big heat input to the cold path can be observed, caused by the largest temperature difference here. However, the overall energy balance is consistent.

Case 04

For calculation case 04, the temperature distribution and the energy balance are illustrated in Figure 6.10.
Similar behaviour as in the previous case can be seen, although much less heat is transferred within the porosity section. Compared to 666 W in the previous case, the introduced heat into the cold path is 305 W which is less than the half.
Comparing section 2 of both cases, no big difference can be seen. In section 4 about 30 W are transferred more which is explainable by the bigger temperature difference between hot and cold path in this section.
In sum, about 461 W of heat was exchanged between hot and cold path whereby it was 787 W in the previous case without gap between porosity and solid.
The energy is also in this case balanced. All the heat flux removed from the hot

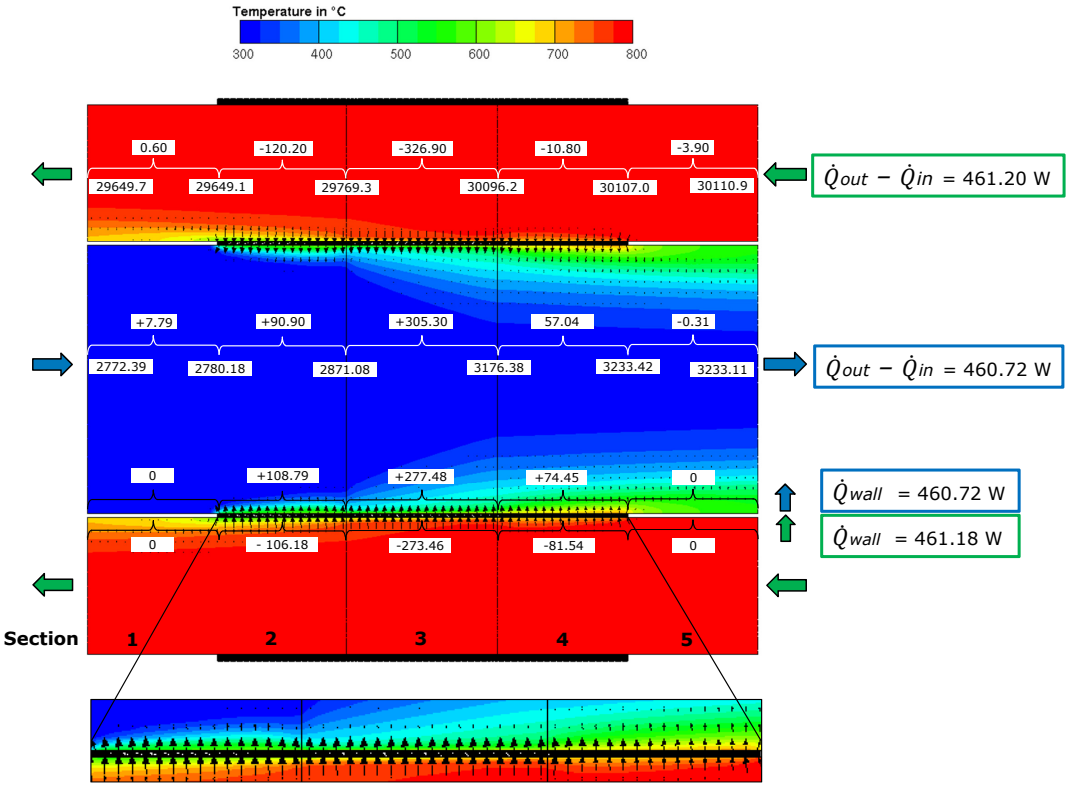

Figure 6.10: Temperature distribution with energy balance of Case 04

path was transferred through the solid domain into the cold anode path.

6.1.5 Summary and Further Procedure

The investigation of the mesh resolution showed that the calculation results are independent of the mesh size in the near-wall region. As a consequence of this finding, the calculations on the full Gas Processing Unit model were performed with a mesh with a larger cell size in the boudary layer. This reduces the overall cell number and the calculation time.
The implemented gas gap between porosity and solid wall in order to decouple the porous medium from the wall showed a big influence on the heat transfer. Even a small gas gap of 0.2 mm acts as an insulation and reduces the heat transfer nearly by the half.

Due to the fact, that in this application the flow within the porous medium is laminar, the turbulence treatment which is done in the porous media, represents a good approximation. Although the automatic **3d!** output of heat transfer coefficient has no significance as simulation output when the porosity is coupled directly with the wall, the energy balance shows coherent results. If the heat transfer coefficient is of interest, it can be calculated from the local heat flux density ($\dot{q}$) and the temperature difference between the wall and the core flow.
Therefore, for the assessement of heat transfer on full model, the coarser mesh and the approach with an aligned connection between the porosity and the solid wall were used. It has to be considered that this approach is very optimistic because perfect contact between porpous media and metal parts is assumed, which might be compromised especially at elevated temperatures due to different thermal expansion coeffcient of different materials.

6.2 Gas Processing Unit

For a better orientation, in Figure 6.2 an overview of the domains anode line, exhaust line and solid housing is illustrated in which the main components which are investigated in the following chapter are named. The evaporation area extends from anode line inlet to the begin of the reformer pipe.

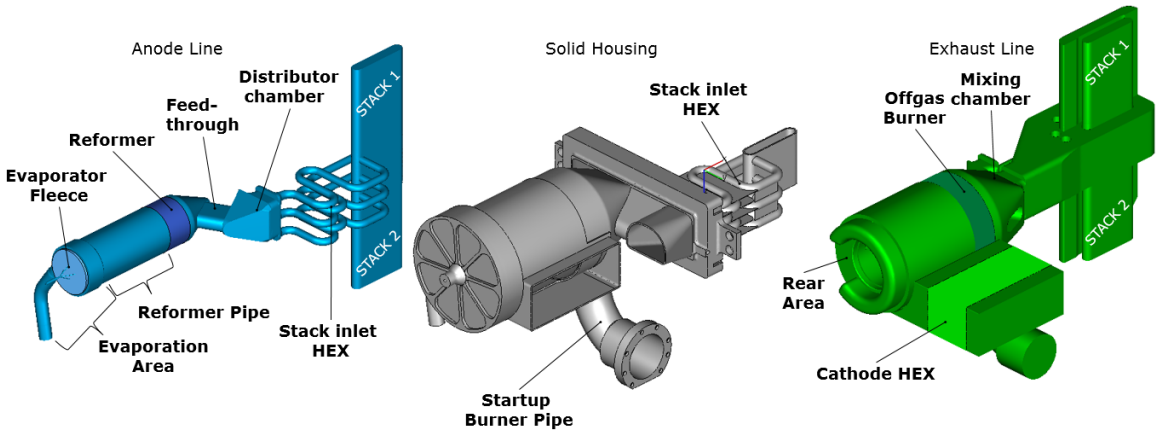

Figure 6.11: Overview of the components of the three calculation domains

In the evaporation area a heat sink was implemented corresponding to the cooling by the phase transition from liquid to gaseous state. In the reformer pipe an overheating of the anode gas mixture occurs via heat transfer from the hot exhaust line through the solid housing. The stack inlet HEX consists of five bended pipes. The mixing chamber of anode and cathode off-gas is located upstream of the off-gas burner. The startup burner pipe is part of the CAD geometry and hence considered also in the CFD mesh. It is located in the exhaust line and can be identified by a bent pipe opposite to the main flow direction from mixing chamber inlet to off-gas burner.

6.2.1 Convergence Check

In Figure 6.12 a plot of residuals from numeric solver iterations of the transient calculation can be seen. The time range lasts from 9.0 to 10.0 seconds.

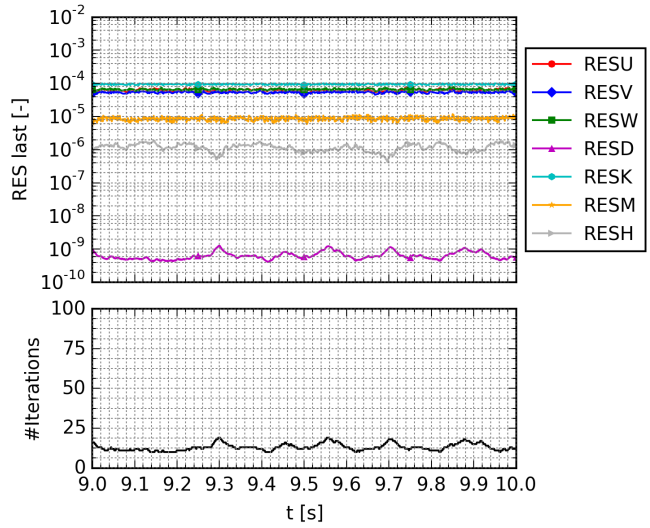

Figure 6.12: Convergence plot of Gas Processing Unit transient calculation

The convergence criterion was kept at 10^{-4} for the kinetic energy which showed the highest residuals. To fulfill this criterion, there were performed approximately 15 iterations per timestep.

6.2.2 Flow Results

Pressure Field

Calculation results for total pressure can be seen in Figure 6.13. The total pressure field of the anode line is illustrated in the left image and the exhaust line in the right image, based on a section normal to the z- and x-axis.

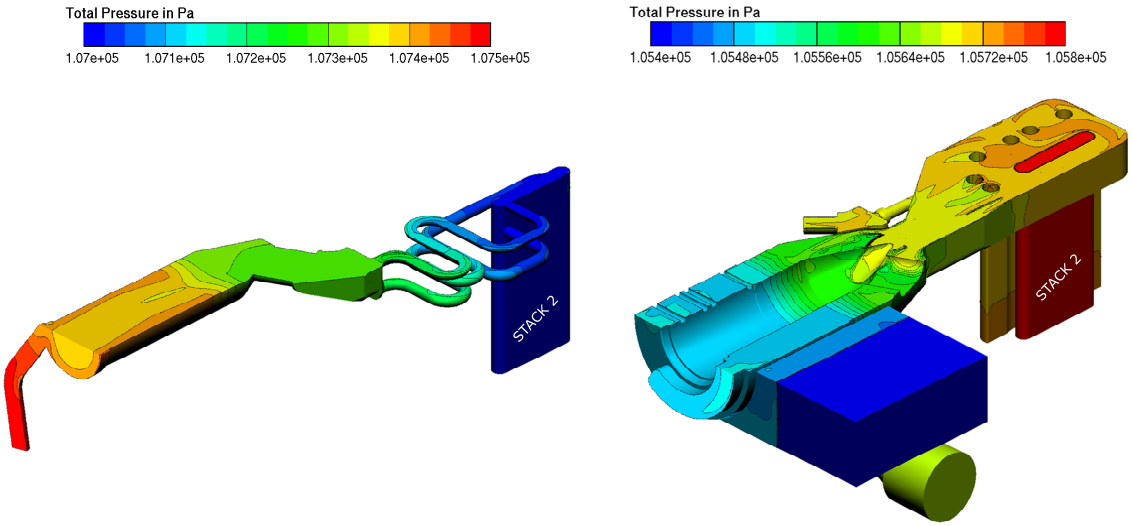

Figure 6.13: Pressure field of anode line (left) and exhaust line (right)

In general, the pressure reduces in the direction of flow from inlet towards outlet. The only exception is the reformer pipe which shows a swirling flow and therfore a radial pressure gradient.
Regarding the anode line, the inlet pressure is about 107500 Pa and the outlet pressure follows the boundary condition of 107000 Pa. This results in a global pressure drop of 5.1 mbar from inlet to outlet (at a massflow of 1.84 g/s), from which 1 mbar can be assigned to the reformer catalyst and 1.1 mbar to the inlet pipe including reformer pipe to the catalyst inlet, and the highest pressure loss, namely 3 mbar, occurs in the stack inlet HEX. The inlet pressure differs from the measured pressure at this point by 3mbar. This relatively big difference could be dedicated a possible measurement inaccuracy or an inaccuracy of the tube friction pressure drop model used for the catalytic converters. For future investigations, a Forchheimer pressure

drop model based on measurements is recommended for calibration. Also the position of the sensor could have a big influence on the measuring results due to a possible measurement of stagnation point pressure.
The pressure field of the exhaust line (at the right image) is governed by the high pressure drop in the cathode Heat Exchanger of 38.4mbar, which generates uniform inflow into the HEX and benefits the flow activity in the rear area of exhaust line. The global pressure drop from inlet to outlet is 41.9mbar at a massflow of 14.53g/s. The pressure drop of the oxidation catalyst is 1.3mbar and the rest is very small. The remaining losses can be assigned to the mixing chamber before the oxidation catalyst. An uncertainty can again be assigned to the oxidation catalyst which is based on the tube friction pressure drop model. It is probable that the pressure drop of the oxidation catalyst is bigger than calculated and the pressure drop of the cathode HEX should be lower by accordingly this amount.
The anode line of the stack module features a pressure drop of 12 mbar from stack inlet to stack outlet flange.

Velocity Field

In Figure 6.14, the streamlines of the anode line and the exhaust line are illustrated in an isometric view. The colour of the streamlines corresponds to the local flow velocity.
Regarding the anode line, an intense swirl is to identify in the reformer pipe before the reformer catalyst, caused by the inlet pipe, which is positioned eccentrically (tangential to reformer pipe). The swirl flow homogenizes along the reformer pipe and then continues in the reformer catalyst where it is straight through the monolith channels. After the reformer outlet, the flow is accelerated in a feedthrough and passes through a distributor chamber into the five stack inlet HEX pipes which show an uniform velocity field.
Compared to the anode line, the exhaust line represents a more undistributed flow field. It can be seen that the velocity reaches its maximum in the mixing chamber before the oxidation catalyst, where anode and cathode outlet of the stack are mixed. The flow in the mixing chamber seems to be more irregluar than in other areas. In addition, a backflow before the porosity is identified, which will be further discussed. In the rear section of the flow area downstream of the off-gas burner (at

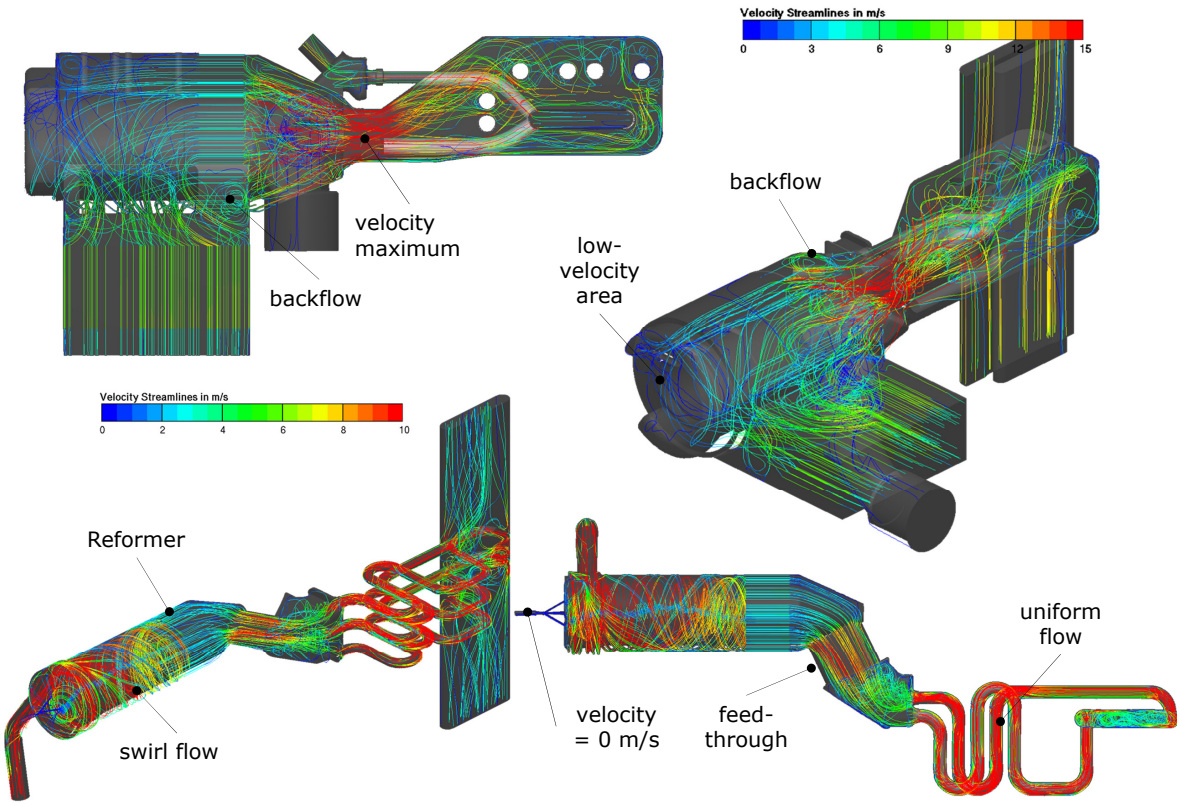

Figure 6.14: Streamlines of anode line (bottom) and exhaust line (top)

the left of the exhaust line picture), there can be seen a relatively large low-velocity area. The flow turns towards the exhaust outlet already before reaching the rear area of the exhaust line. In this area of low velocity, a lower heat transfer can be expected and therefore, it could be improved by rerouting the flow or, seen from another perspective, saving space by reducing this inactive region.
The pictures in the top left and the bottom right of Figure 6.14 show the same results but from a different view. It is to recognize in the anode line, that the velocity of the fuel inlet (at the left of the right picture) is zero, as specified in the boundary conditions. In addition, a low-velocity field can be found in the center of the reformer pipe, which is a consequence of the intense swirling flow.
In the exhaust line plot at the right of Figure 6.14, the low-velocity area in the rear is shown again. A backflow area is located before the oxidation catalyst at the right and before the cathode HEX. In general, there is to see a preference of the flow to

choose the shortest route.

Figure 6.15: A more detailed view gives Figure 6.15 which is a velocity magnitude plot in the xy-plane.

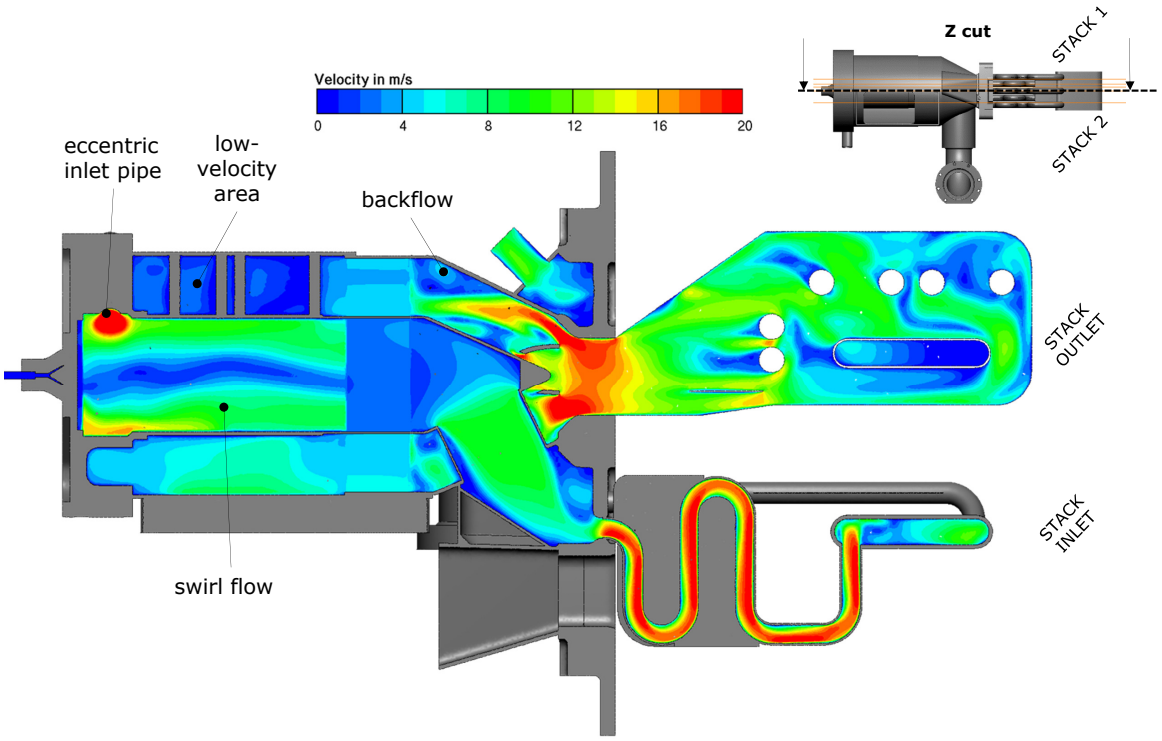

Figure 6.15: Velocity field of the GPU (plot in the xy-plane)

At the left side in the anode line is to recognize the eccentric inlet pipe with a velocity of about 17 m/s which causes a swirl flow containing a low velocity core flow. This swirl flow should ensure a good mixing of fuel and recirculated anode off-gas and air mixture and thus an uniform flow within the reformer catalyst. The flow in the reformer catalyst looks well distributed, which indicates a good design of the anode line inlet and the reformer pipe length.
In contrast, the velocity field of the exhaust line looks more irregular than the velocity field of the anode line. The velocity decreases in the rear section of the

exhaust line and the design of the mixing chamber results in a backflow before the oxidation catalyst and in a flow unevenness within the oxidation catalyst.

In Figure 6.16 another velocity plot in the xy-plane through the lower anode outlet pipe of the stack is shown.

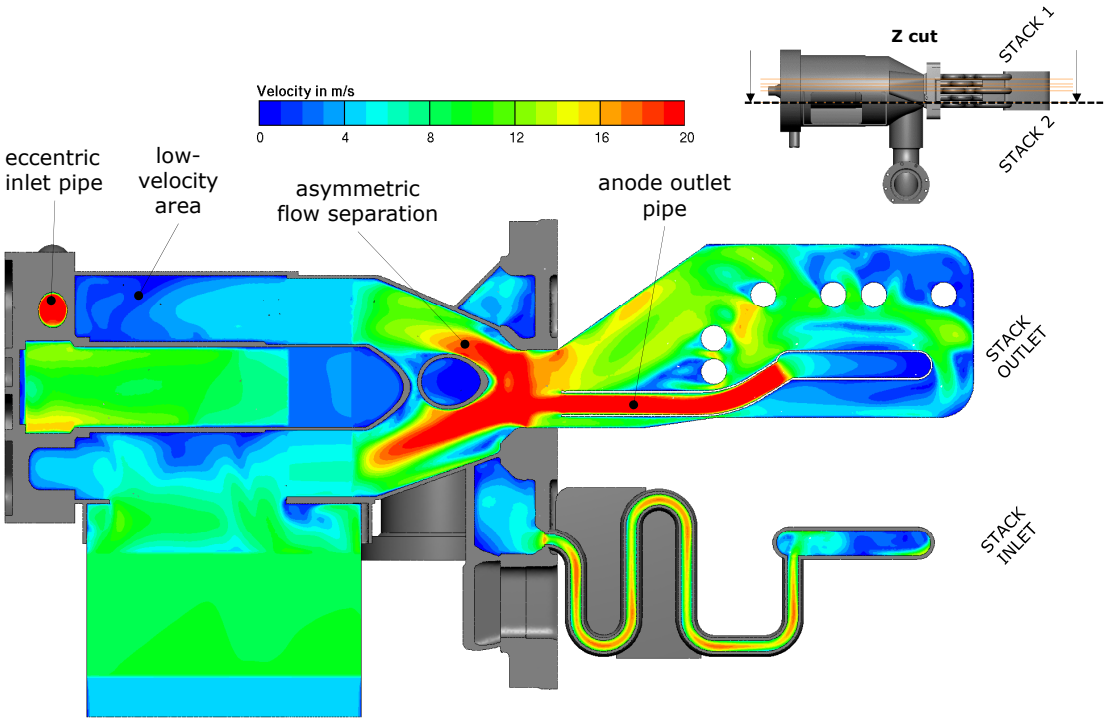

Figure 6.16: Velocity field of the GPU (plot in the xy-plane)

Because of an eccentrical arrangement of the anode pipes, an asymmetric flow separation occurs caused by the starter burner cone. This constitutes an uneven flow distribution in the oxidation catalyst which can be seen better in this picture.

Figure 6.17: Another view to represent more explicitly the effects of the two anode pipes on the velocity field of the exhaust line is shown in Figure 6.17.
The backflow at the top area in the mixing chamber before the catalyst is caused by the geometry of the anode pipes and the step in the solid interface right after

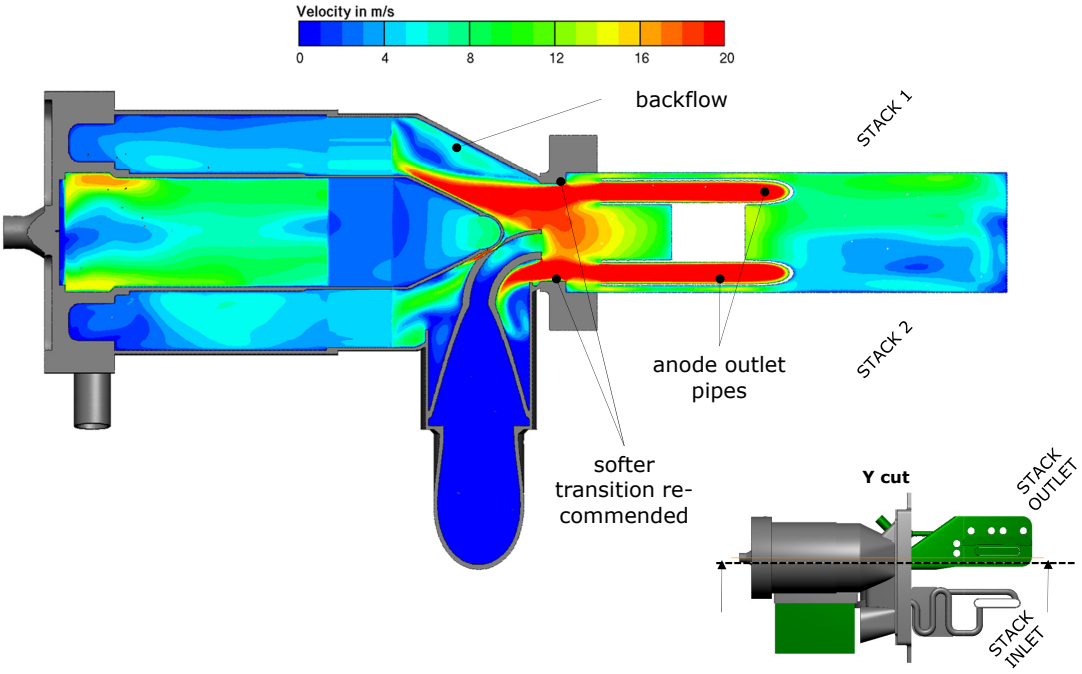

Figure 6.17: Velocity field of the GPU (plot in the xz-plane)

the anode pipes. This backflow can be reduced by implementing a softer transition between anode pipes and oxidation catalyst. Despite that, the high velocity stream towards the anode line caused by the upper anode pipe, is generating an efficient heat transfer in this area.
The starter burner pipe, which is located at the bottom of the mixing chamber, is not used in the continuous operating condition. It shows a low-velocity area because there is no flow within (also according to measurement).

Figure 6.18: In order to illustrate the velocity conditions within the gas processing unit, Figure 6.18 shows velocity plots of the assembly in planes normal to the main flow direction.

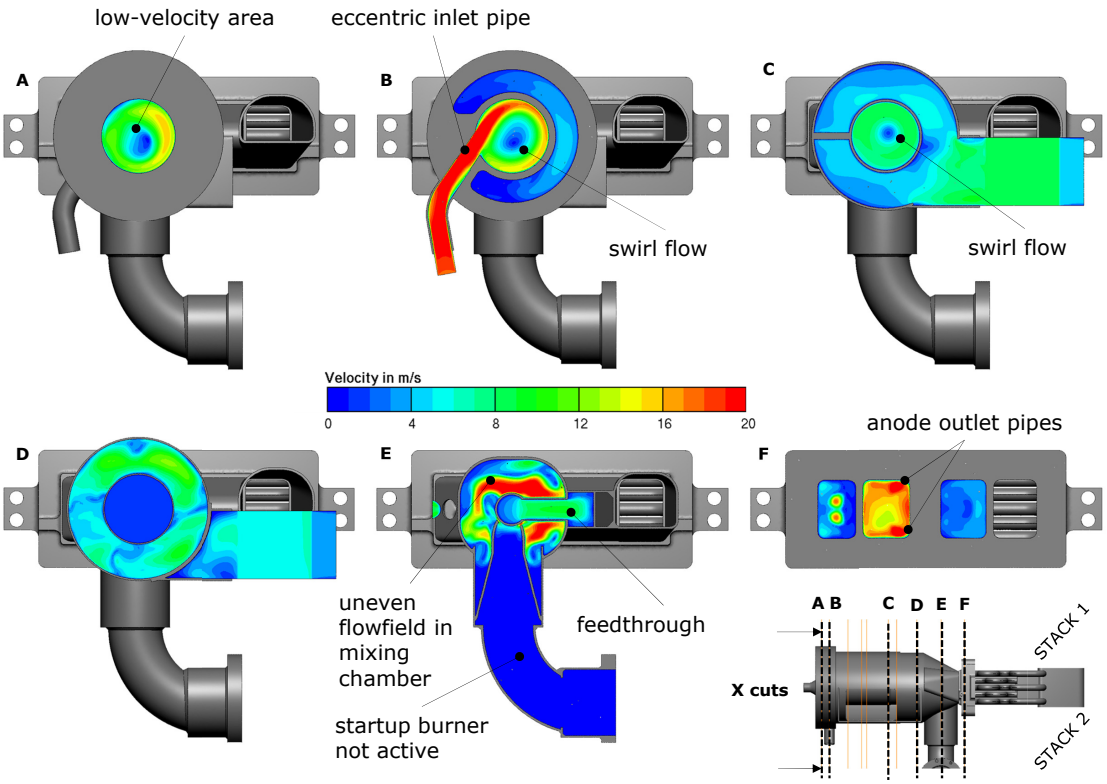

Figure 6.18: Velocity field of the GPU (plots in the yz-plane)

Cut A shows the velocity at the rear of the GPU, more precisely at the plane of the evaporator fleece. Right at this plane, the diesel fuel is applied by four bores inside of the metal housing. These bore holes can also be seen in Figure 6.14 at the left of the anode line picture. The opening angle of the fuel lines is so small that the fuel is introduced at a low-velocity area. By bringing the inlet pipe closer to the fleece, a higher velocity could be achieved at the fuel inlet area, therefore the heat transfer and thus the evaporation could be improved.

CUT B: In Cut B the inlet pipe of the anode line is illustrated. The swirl flow with the low-velocity core is clearly evident as well as the moderate flow of the exhaust line rear area.

Cut C pictures the velocity field of the gas processing unit downstream of the oxidation catalyst in the exhaust line and upstream of the reformer catalyst in the anode line. The reformer catalyst demonstrates a more or less even flow field at inlet, which is still swirling intensively, except of a small zone near the core which shows flow close to stagnation.

Cut D: In Cut D the same as in Cut C is illustrated but upstream of the oxidation catalyst and downstream of the reformer catalyst. The flow out of the reformer is not swirling any more, and hence features significantly lower flow velocity.

Cut E once more illustrates the velocity distribution within the mixing chamber before the oxidation catalyst. The high velocity area above the center results from the anode pipes from stack (primarily the upper pipe) and the constriction of the flowfield by the anode line feedthrough. The velocity maximum in the lower right corner of the exhaust line is most probably caused by the lower anode pipe. In general, the reason of the uneven flowfield in this section is shown in the previous Figure 6.17 within the mixing chamber. However, high velocity zones near an adjacent component such as in this case the anode line, deliver a good heat transfer. Therefore, the heat transfer should be considerably better in this areas and should be improved at the left side of the center. The horizontal passage in the center is the feedthrough passage from anode downstream the reformer towards the stack.

CUT F: In order to complete the velocity field disrtibution of the gas processing unit, Cut F shows a cut through the stack manifold/GPU interface. It consists of 4 sections. At the left, there is the recirculated flow path which is led to the recirculation blower. The second flow field from the left shows the inlet into the mixing chamber, including the two velocity maxima of the anode pipes, which are a reason for the continued flow irregularity towards the oxidation catalyst. The third flow field shows the anode line which leads to the stack inlet and the section at the right is the cathode inlet of the stacks, which was not modelled.

Uniformity & Centricity Index

The velocity distribution in the third cell layer evaluated within the third cross section cell layer of each porosity is illustrated in Figure 6.19.

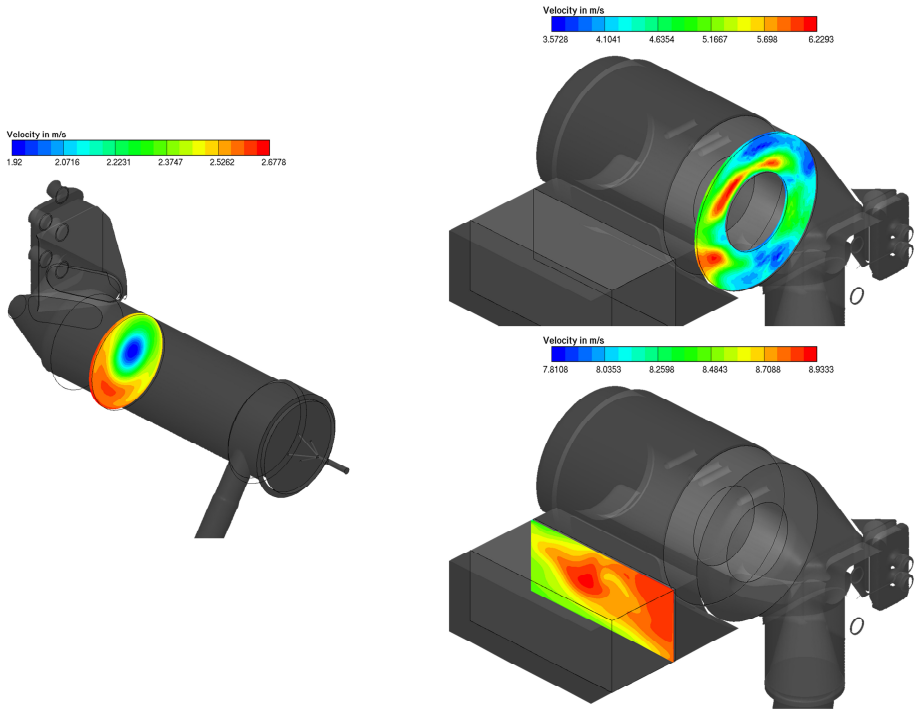

Figure 6.19: Velocity field in 3rd cell layer of reformer catalyst (left), oxidation catalyst (top right) and cathode HEX (bottom right)

The velocity distribution of the **reformer catalyst** (top left picture) shows the consequences of the swirled flow in the reformer pipe which was to be expected from the preceding velocity plots. The velocity scale in Figure 6.19 ranges just from 1.92 m/s to 2.68 m/s which is a deviation from the average velocity (2.3 m/s) of -/+ 17% which is an acceptable difference.
In the velocity field of the **oxidation catalyst** (at the top right in the picture) there are to see once again the effects of the stack anode outlet pipes and the anode line feedthrough expressed by the velocity maxima. The low-velocity area at the top results from a backflow in this field and at the bottom it is caused by the starter burner cone which deflects the flow towards at the oxidation catalyst. The more inhomogenuous velocity field at oxidation catalyst can also be the effect of the

premature combustion. The scale of the oxidation catalyst velocity plot shows an average value of 4.9 m/s and a deviation between the average velocity and the minimum/maximum of -/+ 27%.
Regarding the **cathode HEX**, the velocity scale ranges from 7.8 m/s (-7%) to 8.9 m/s (+7%), at an average of 8.4 m/s, even though a low velocity area at the left of the plot can be recognized due to the low-flow areas in the rear of the GPU. The result can be a better heat transfer from exhaust line to cathode line within the cathode HEX in the areas with higher velocities.
Good criterions for the quality of a flow are the uniformity and the centricity index and a criterion for the porosity durability is the tangential pressure gradient which are explained in section 2.2.2.
Results for uniformity, centricity index and tangential pressure gradient can be seen in Table 6.1. Also included are the company internal guidelines.

Table 6.1: Evaluated uniformity, centricity indices & tangential pressure gradient in comparison to AVL guidelines

Porosity	Uniformity Index	Centricity Index	Tangential Pressure Gradient
	-	-	bar/m
AVL Guideline	> 0.95	> 0.85	< 15
Reformer	0.96	0.97	0.03
Oxidation Catalyst	0.94	0.92	0.24
Cathode HEX	0.99	0.98	18.7

The uniformity index and the centricity index of the reformer catalyst achieve good values and also the tangential pressure gradient is negligibly small, which is explainable by the well distributed flowfield and the reformer pipe, which is long enough. In contrast, the uniformity index for the oxidation catalyst lies below the limit with a value of 0.94. The centricity index and tangential pressure gradient are again within the permitted range. The velocity indices for the cathode HEX are within the limits but the value of the cathode HEX is above the limit for metal substrates. Channel damaging due to material erosion could therefore be the consequence. However, it is to consider that the cathode HEX is not a substrate but a plate HEX and therefore has a larger wall thickness (around 1mm) which are more

robust than the walls of a metal catalyst.

6.2.3 Temperature Distribution

In Figure 6.20 the temperature in a xy-plane cut can be seen which corresponds to the velocity contours in Figure 6.15.

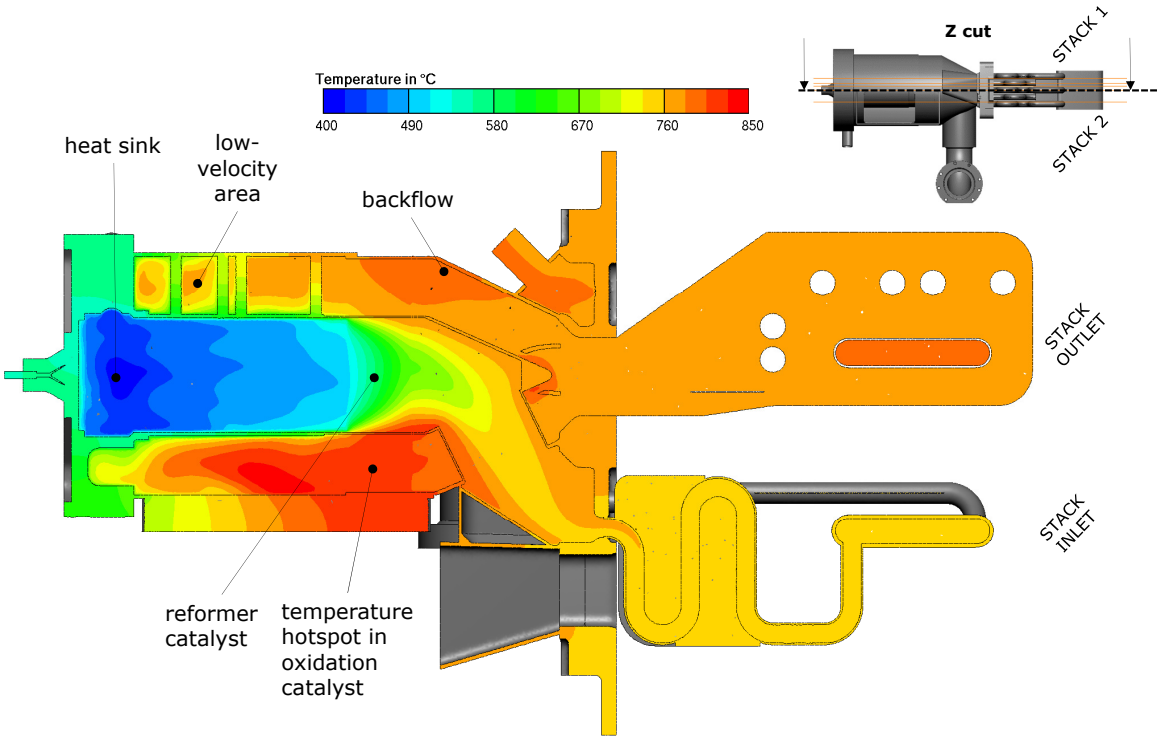

Figure 6.20: Temperature field of the GPU (plot in the xy-plane)

Regarding the anode line, at the left side the heat sink can be seen, which was implemented in the CFD calculation to the inlet area in order to represent an endothermic evaporation reaction.
The anode line, which starts at a temperature of about 410°C, is heated up along the reformer pipe about 100 °C due to the heat transfer from the hot exhaust line through the solid.
The refomer catalyst can be easily recognized through the strong rise in temper-

ature from 534 to 743 °C (cross section averaged) due to the additional heat conduction of the ceramic monolith and due to the added heat source that was implemented to consider an exothermic catalytic reforming reaction, which was determined by the measurement and the following matlab calculations.
The anode line gas mixture is further heated up slightly by the slightly hotter exhaust line until it reaches the stack manifold/GPU interface with a temperature of 750°C. The temperature in the stack inlet HEX pipes does not change anymore due to a lack of temperature difference.
In the operation mode under real conditions, the anode line within the stack inlet HEX pipes is cooled by the air supply for the cathode which is not considered in the simulation.
Regarding the exhaust line a temperature hot spot in direction of the cathode HEX can be seen. Likely, this is the outcome of the exothermic catalytic combustion happening in the oxidation catalyst (off-gas burner). At this point and towards the anode line, an increased heat conduction can be expected because of the higher temperature difference.
A temperature increase is also determined in the exhaust line towards the recirculation pipe. This can result from the backflow determined in the velocity view in Figure 6.15. In general, the heat transfer in the rear GPU area from exhaust line to the solid is just moderate due to low velocities. A higher velocity would lead to a higher local exhaust gas temperature and hence a higher solid housing temperature. Therefore a higher heat input into the anode line evaporation area could be achieved. Although, the evaporator fleece on the rear end is also heated from exhaust gas via the solid housing.

In Figure 6.21 the temperature field in a xy-plane cut through the lower anode pipe will be analyzed.
Due to the increased heat release in the mixing chamber, it is obvious that a premature combustion located right after the mixing of stack anode off-gas and stack cathode off-gas happens. The dark red area in the picture indicates a temperature above the range of 400-850°C. In this case, the maximum flame temperature is about 903°C.
Another heat release, although the temperature increase is smaller than in the gas phase combustion, occurs in the oxidation catalyst. It seems that the gas mixture is

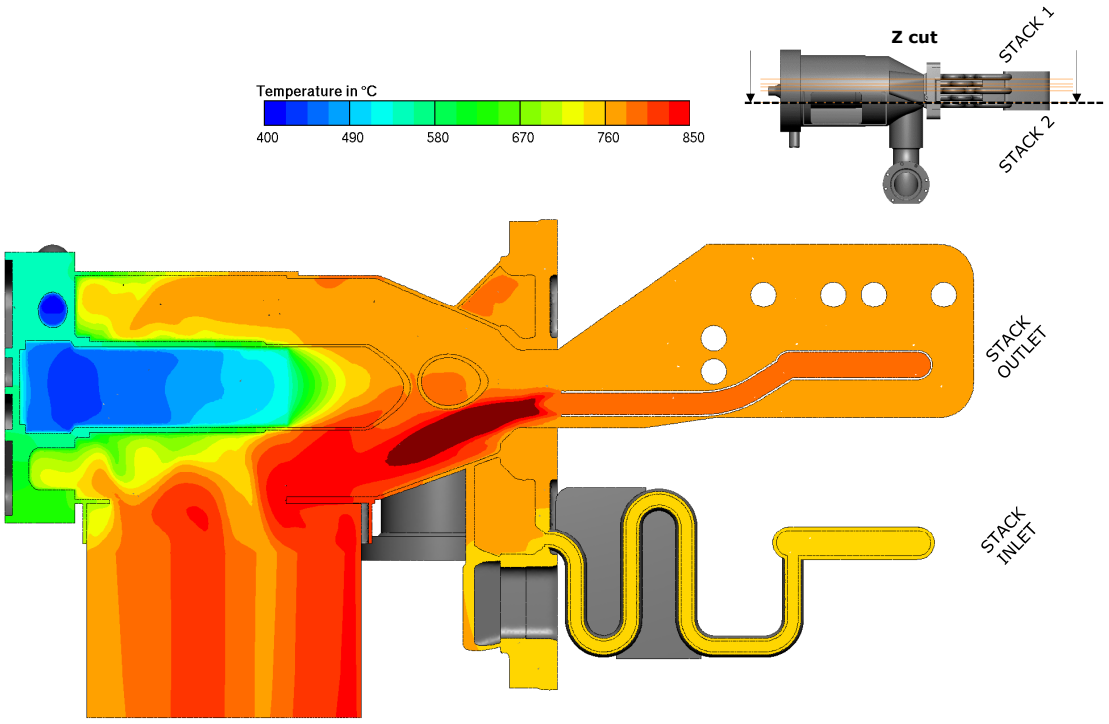

Figure 6.21: Temperature field of the GPU (plot in the xy-plane)

not fully burnt yet, so that the residues can be burnt in the downstream oxidation catalyst. An uneven heat transfer happens to the reformer, because of the uneven combustion in the exhaust line, mainly in regions closer to the cathode HEX. However, the temperature within the reformer should be as uniform as possible to ensure a homogenuous fuel conversion.
The low-velocity field and thus the low heat transfer in the rear of the GPU exhaust line has the negative effect of a visible gas temperature decrease in this area. In contrast to the temperatures in the upstream exhaust line, the temperatures are about 200°C lower and match with the slow flow in Figure 6.16. That means that stagnated exhaust gases are cooled down. The heat input into the anode line could be improved with a, for instance, continuous constriction of the cross section in the rear or by rerouting the flow towards this area.

Figure 6.22 illustrates the temperature results in a plot in the xz- plane in order to illustrate the effect of the stack anode outlet pipes.

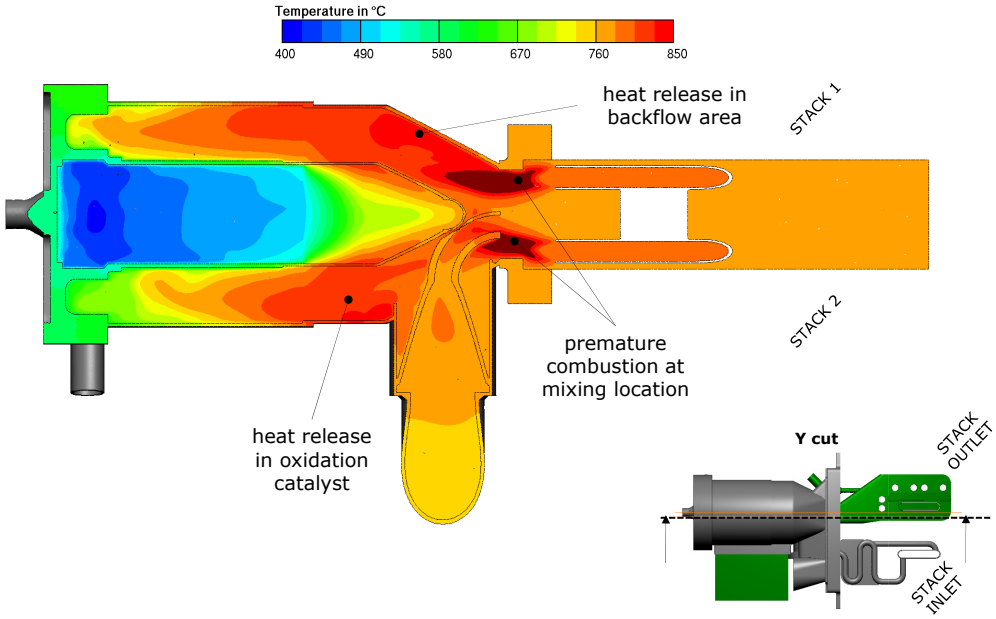

Figure 6.22: Temperature field of the GPU (plot in the xz-plane)

According to the considerable temperature increase, a combustion of H_2 and CO already happens at the interface between stack manifold and GPU. Again, the dark red areas point out a temperature above 850°c.
In relation to the velocity field of Figure 6.17, a heat release can also be determined in the area of backflow in the upper wall area. This effect is investigated later on.
A noticable heat release occurs also in the oxidation catalyst (off-gas burner) which will be further transferred into the reformer and the reformer pipe.

Figure 6.23: The temperature plots corresponding to the velocity plots shown in 6.18 can be seen in Figure 6.23.
The continuous heat loss in the exhaust line is visible in the reducing temperature from Cut F till Cut B.

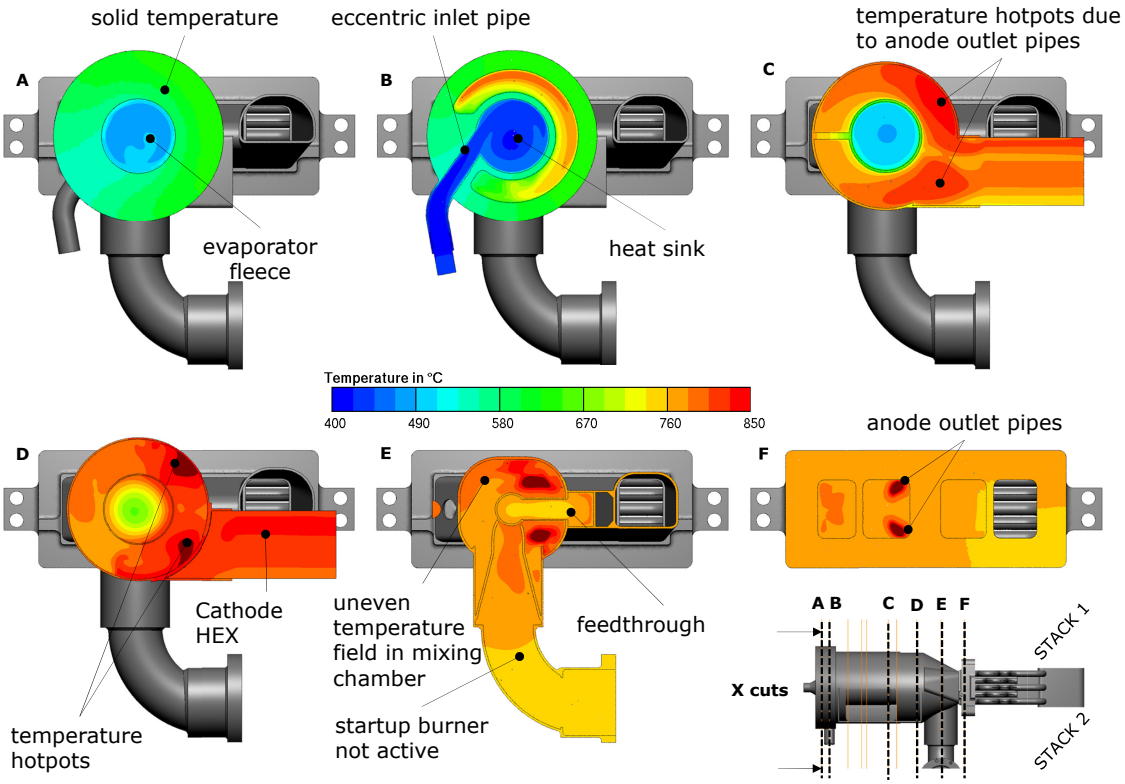

Figure 6.23: Temperature field of the GPU (plots in the yz-plane)

In the anode line, there is to see a continuous temperature increase from Cut B to Cut F. Cut A is closer to the heated fleece, which is not intensively touched by the inflow from inlet pipe, and therefore hotter because heated from the fleece.

In Cut A the temperature of the anode line at the evaporator fleece area can be seen as well as the solid temperature of the housing. As mentioned above, the solid temperature could be increased by a flow improvement in the rear GPU section.

Cut B points out the heat transfer from the exhaust line through the solid housing into the anode line in the rear GPU area. The temperature in this section has its maximum at 760°C which is located in the upper area. The temperature distribution could be improved by a geometry adjustment to current flow conditions. Furthermore, the implemented heat sink in order to model an evaporation process

can be seen.

Cut C shows a temperature cut in the yz-plane located downstream the reformer towards feedthrough and upstream the oxidation catalyst (off-gas burner). In the exhaust line, an uneven temperature distribution can be noticed which is influenced by the premature combustion located near the fuel cell stack anode outlet pipes in Cut F.

In Cut D a slightly uneven temperature distribution can be seen in the anode line because of the premature combustion near the two anode pipes which are arranged eccentrically so that higher temperatures can be reached towards the cathode HEX. Furthermore, there can be seen that the temperature hot spots moved to the outside at the zones of highest velocity shown in Cut D of Figure 6.18.

6.2.4 Conversions

To illustrate the chemical conversion due to the exothermic reactions occuring in the exhaust line, concentration plots in the xz-plane are shown in Figure 6.24, which confirm the expectations based on measurements.
According to section 2.3.3, an indication of a combustion of H_2 in the gas phase can be the production of interrim product hydroxyl (OH). In the upper right corner of Figure 6.24, the concentration of OH is shown. It is obvious, that the gas mixture within the anode pipes out from the stack does not contain any OH. The mole fraction of OH increases as soon as oxidant is added to the anode line. A topology as shown in Figure 2.7 can be determined in the CFD results in in the form of an elevated diffusion flame which results from lateral addition of oxidant to the fuel. The formation of the diffusion flame, more precisely, the area where the OH mole fraction reaches its maximum, is located after a certain distance from the mixing point which can be seen as lifting height.
Another spot of high OH concentration, even if the amount is lower, can be determined along the upper housing of the exhaust line. In this region a backflow was already detected in the velocity CFD results of the same view (Figure 6.17) and also a remarkable temperature increase according to Figure 6.22. This effects are most probably closely connected to each other. It can be said that the chemical chain

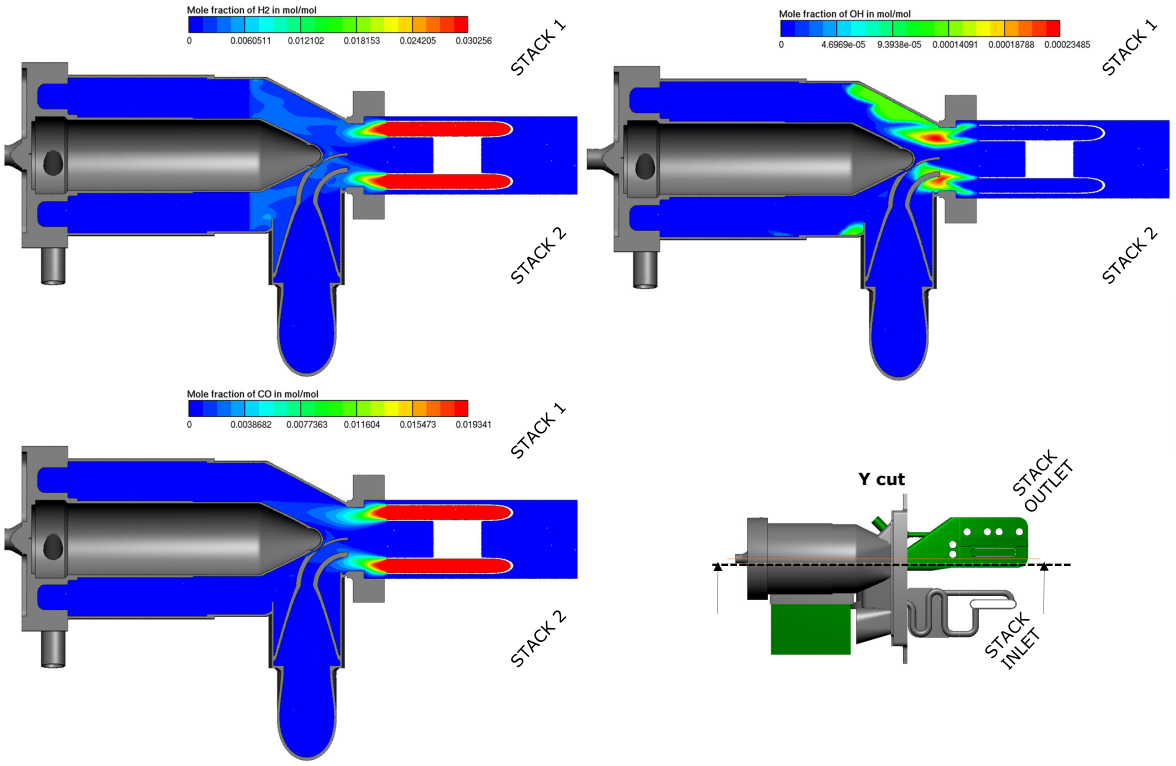

Figure 6.24: Concentrations of hydrogen (top left), carbon monoxide (bottom left) and hydroxyl (top right) of exhaust line (plot in xz-plane))

reactions, which were producing the radical OH, are following an exothermic reaction and result therefore in a heat release.
Another backflow area is clearly evident in the corner between oxidation catalyst and starter burner pipe, which results in an increase of OH and therefore in an increase of temperature.
At the left upper corner of Figure 6.24 a plot in the xz-plane of the H_2 concentration is shown. The H_2 mole fraction of the stack anode outlet gas mixture counts about 3.03% which will firstly be diluted with oxidant and secondly converted to H_2O by oxidation of H_2. Comparing the mole fractions of OH and H_2 shows that they behave strictly opposite because of a combustion.
As soon as the gas mixture reaches the oxidation catalyst, a sudden conversion of the remaining H_2 occurs, most of it already in the first cell layer. In the temper-

ature field in Figure 6.22 it can be seen that the temperature remains unchanged downstream along the oxidation catalyst which can be the result of the additional heat conduction happening in the metallic catalyst.
At the bottom of Picture 6.24 the concentration of CO is plotted. In contrast to H_2, CO seems to be converted even faster and is already nearly totally converted when the gas reaches the oxidation catalyst.

6.2.5 Heat Transfer

The focus of heat transfer assessement is on the anode line in order to have a better overview of the results. The resulting heat transfer at the counterparty, which is the exhaust line, was already confirmed as identical during the test calculations on the simplified model. Therefore, for now just the anode line will be examined.
In Figure 6.25 CFD results for evaluating the heat transfer are shown.
As already noticed at the simplified model in sections 6.1.3 and 6.1.3, at the Gas Processing Unit, the y^+ is, again, very small at the interface porosity/solid and therefore, this heat transfer coefficient is again drastically higher in the reformer due to conductivity effects compared to the pure fluid wetted surfaces. Nevertheless, the temperature field reaches acceptable values.
In the figure the wall heat flux density, the temperature, the dimensionless wall distance (y^+) and the heat transfer coefficient (α) of the anode line are illustrated.
Starting with the heat flux density ($\dot{q}$), a hot spot of heat input can be located at the anode inlet pipe in the evaporation area. The heat flux has, most probably, a peak in this area because of the highest temperature difference between anode and exhaust line in the rear. The anode reformer gas mixture starts at 421°C and will be warmed up continuously by the about 150°C warmer solid domain, shown in Figure 6.20. Right at the top of the evaporation area in the $\dot{q}$ plot, there is a maximum which can be explained by a velocity maximum due to the swirled inlet flow. The heat input there could be homogenized by variation of the inlet pipe inclination.
However, it has to be pointed out that the heat flux, which is transfered through the wall into the anode line for gas conditioning, is well distributed along the reformer pipe on the way to the reformer catalyst which should result in an even temperature increase during the mixing length.
The heat input in the near of the reformer catalyst is about twice as high as in the

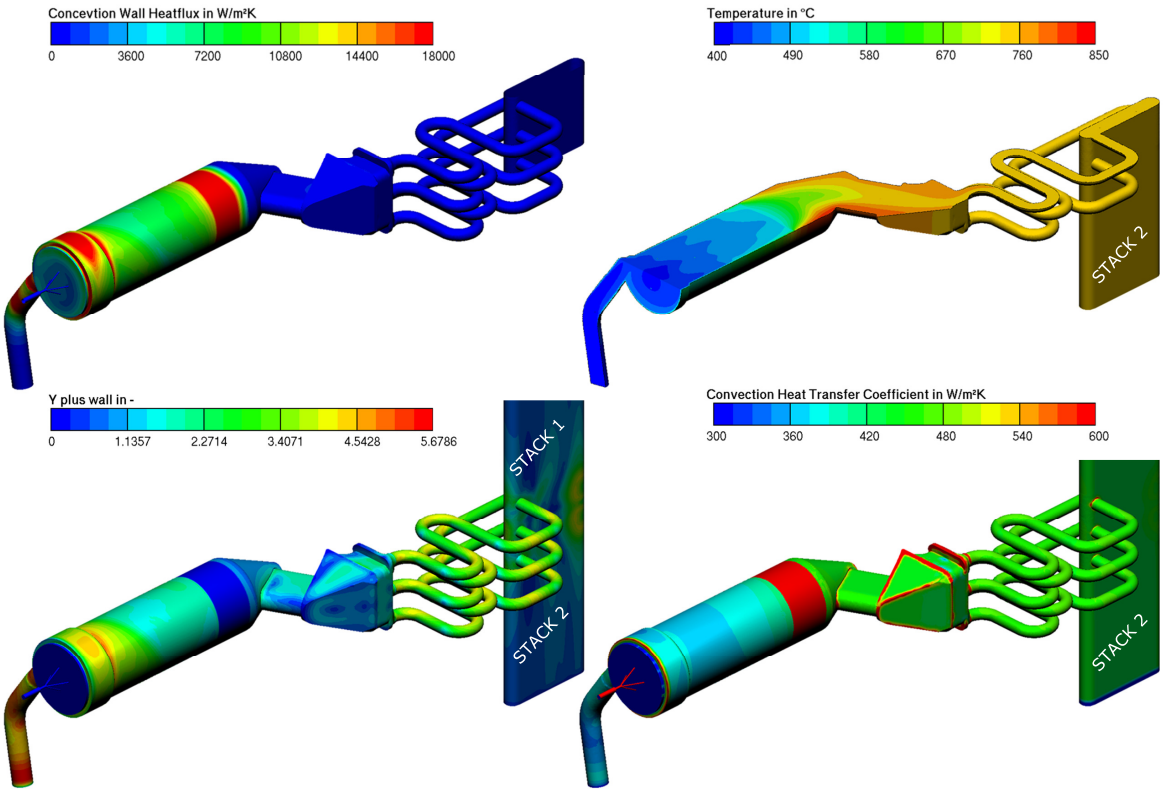

Figure 6.25: Convection wall heat flux (top left), temperature (top right), dimensionless wall distance (bottom left) and heat transfer coefficient (bottom right) of anode line

reformer pipe. This can again result from the increased temperature difference as well as from the increased heat conduction due to a solid component within the porosity channels. Also the temperature field at the right shows the largest temperature increase within the reformer catalyst. This is because of both, the heat release of the exothermic reforming reaction, and the heat conduction happening in the ceramic monolith. In the temperature plot the heat sink of the evaporation is visible in the front at the inlet section.
Right after the reformer catalyst in downstream direction the temperatures are similar with the solid and exhaust line so that there is no noticable heat flux density between anode and exhaust line. In this area there is also no remarkable velocity close to the wall to support the convective heat flux.

The cooling effect of the heat transfer of the cathode line towards the stack inlet HEX was not modelled in this investigation, so this local heat flux density provides no desirable information. In reality, there may happen a heat transfer to the colder cathode line and the temperature field within the stack inlet HEX may be lower as shown in the results.
Face averaged values for wall heat flux and α are listed in 6.2.

Table 6.2: Evaluated wall heat flux and heat transfer coefficient in anode line

	Heat Flux Density	Wall Heat Flux	Heat Transfer Coefficient
	W/m^2	W	W/m^2K
Evaporation Area	8337.9	135.1	450.6
Reformer Pipe	9184.1	214.0	377.8
Reformer	32779.5	223.3	183.4
Feedthrough	-351.6	-9.1	477.7

The highest $\dot{q}$ is determined at the interface solid/reformer because of the additional heat conduction of the catalyst ceramic sustrate. The heat input to the reformer is therefore 223.3 W.
The face averaged $\dot{q}$ from the reformer pipe to the anode line gas stream achieves a good value, too. The heat flux is very uniform along the whole reformer pipe which is generated by the swirled flow due to the eccentric inlet pipe.
The evaporation area shows a lower average $\dot{q}$ value because of lower heat flux through inlet pipe and fleece.
Through the feedthrough there is no remarkable $\dot{q}$ anymore, because a slow convection without a big temperature difference.
The face averaged heat transfer coefficient at the reformer is evaluated according to formula 6.2. The gas core temperature T_∞ was extracted from the temperature field in 6.26, the face averaged wall temperature T_w as well as the face averaged wall heat flux density $\dot{q}$ were derived from 3D result output formulas (Appendix C).

$$\alpha = \frac{\dot{q}}{(T_w - T_\infty)} = \frac{32779.5 W/m^2}{(782.5 - 583.2)^\circ C} = 183.4 W/m^2K \tag{6.2}$$

In comparison to the temperature and velocity distribution along the reformer middle plane of the simplified model (6.5) the velocity of the core in the reformer of

the GPU shows lower values due to the swirled flow in the reformer pipe. Also the temperature is not symmetrically to the reformer axis because of an uneven temperature distribution in the exhaust line.

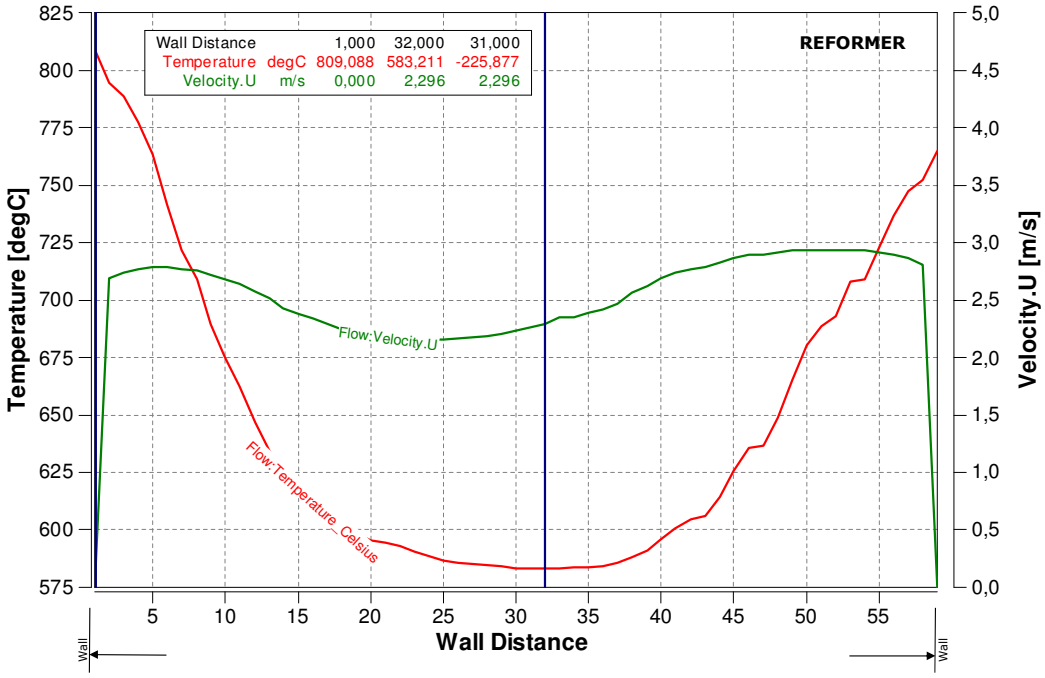

Figure 6.26: Temperature and Velocity distribution along reformer middle plane

7 Conclusions

7.1 Summary

In this thesis, two different investigations were performed. Before the full Gas Processing Unit was analyzed, a parameter study was performed on a simplified model.

Simplified Model: The simplified model, consisting of two flow domains including porous media and a solid body in between, was investigated in order to check the plausibility of a coupled simulation, using the FIRE^{TM} aftertreatment module. For the simplified model, the velocity and temperature distribution were analyzed, as well as wall results like the dimensionless wall distance (y^+), the heat transfer coefficient (α) and the heat flux density.

Gas Processing Unit: The second part deals with the full model of the GPU developed by AVL, applying the selected modelling approach from simplified model and containing the same porous media within a more complex geometry. According to Auxiliary Power Unit (APU) system test data, the boundary conditions for the CFD simulation were determined with help of certain pre-calculations and 1D simulations. In the full model, catalytic combustion reactions were implemented in the off-gas burner and gas-phase reactions in the mixing chamber before the off-gas burner to determine an efficient exhaust gas aftertreatment. The focus of the GPU analysis was placed on pressure, velocity and temperature distributions. In addition, the species conversions in the exhaust line were discussed.

7.2 Conclusions

The simplified model predicted **extremely low** dimensionless wall distances and **extremely high** heat transfer coefficients at the interface porosity/solid wall. If α is of interest, it is recommended to calculate the heat transfer coefficient from the heat flux and the temperature difference between wall and core.
An **implemented gas gap between porosity and solid wall** prevented these effects, but caused an interruption of the thermal conductivity in the outer layer of the porosity towards the wall and therefore acts as an insulation. This becomes evident by the observerd higher wall heat flux in the case of no gas gap between porosity and wall. Therefore, this modelling approach can be seen as a possibility to calibrate the simulation result towards reduced heat transfer of measurement results.
Concerning the **energy balance**, all the heat leaving the hot path is recovered in the cold path. All the analyzed sections show a good correlation of enthalpy flux and wall heat flux.

The analysis results of the Gas Processing Unit reflect the assumptions of the measurement regarding **premature combustion** of stack exhaust gas already in the mixing chamber before the off-gas burner. This mixing chamber flow is controlled by an inhomogenuous velocity distribution caused by the design of the stack anode outlet pipes.
A relatively large area in the rear of the exhaust path shows low velocity because the flow chooses shorter pathways which is adversely affecting the convective heat transfer in the region of evaporation and gas preparation before the reformer.
The swirl flow in the reformer pipe causes an uniform flow distribution along the reformer pipe wall, which homogenizes the heat transfer. By bringing the inlet pipe closer to the evaporation fleece, a higher gas velocity could be achieved at the fuel inlet area.
Porosity specific evaluation criteria show good results for the reformer catalyst, borderline results for the oxidation catalyst. A high tangential pressure gradient was observed in the cathode HEX. Here, it is recommended to improve the incident flow, i.e. by guiding ribs, in order to avoid damages.
Altogether, the heat transfer betweeen exhaust line and anode line is good, though

the local premature combustion of stack anode and cathode off-gas with its relatively small combustion zone causes an inhomogenuous temperature field in the mixing chamber. By avoiding a combustion already in the mixing chamber or by moving the anode outlet pipes to the center of the flow field, the oxidation catalyst could be operated more consistent.
The species conversion results demonstrate an almost completed combustion of exhaust gases before the oxidation catalyst which could therefore be dimensioned smaller in case of premature combustion.

7.3 Outlook

This thesis represents a step towards a multi-material CFD flow simulation with Species Transport and chemical reactions in the gas-phase or in a catalyst including heat transfer. This was demonstrated for the GPU of a mobile fuel cell system.
In order to improve the quality of the prediction, a **phase transition from introduced fuel to gas** could be implemented and **catalytic reforming reactions** to the reformer. The fuel evaporation was modelled very simplified in this CFD model. A further improvement step is to investigate the fuel mixture with the recirculated anode gas.
The gas composition was conserved through the whole anode line. A **detailled calibration based on systematic measurements** would enable a modelling in greater detail.
The CFD model is prepared also for **investigations of start operation** or other operating points, therefore it is suggested also to use the opportunity to derive improvement suggestions.
In general, for further invesigations, more concrete measurements, especially gas species measurements, more detailled temperature measurements and a higher number of pressure measurements are necessary, at least before and after the catalysts. This would enable a better calibration of the models applied.

Bibliography

[1] S. Ahmed and M. Krumpelt. Hydrogen from hydrocarbon fuels for fuel cells. *Int. J. Hydrogen Energy*, 26(4):291–301, 2001.

[2] Raimund Almbauer. *Numerische Methoden in der angewandten Thermodynamik*. Lecture notes, Graz University of Technology, 2009.

[3] AVL List GmbH. Aftertreatment Module - AVL FIRE ® VERSION 2014.2 ©, 2014.

[4] AVL List GmbH. FIRE CFD Solver - AVL FIRE ® VERSION 2014.2 ©, 2014.

[5] AVL List GmbH. Porosity Module - AVL FIRE ® VERSION 2014.2 ©. 2014.

[6] AVL List GmbH. Species Transport Module - AVL FIRE ® VERSION 2014.2 ©. 2014.

[7] Stefania Carmen Bobaru. *High pressure STM studies of oxidation catalysis*. PhD thesis, Leiden University, 2006.

[8] Fabian Denner. *Vergleich und Validierung verschiedener CFD-Codes*. Project thesis, Stuttgart University, 2008.

[9] Deutsche Edelstahlwerke GmbH. *X15CrNiSi25-21 1.4841*. Material data sheet.

[10] Inc. EG&G Technical Services. *Fuel Cell Handbook*, volume 7 Edition. U.S. Department of Energy, 2004.

[11] Helmut Eichlseder. *Thermodynamik*. Lecture notes, Graz University of Technology, 2008.

[12] Helmut Eichlseder and Manfred Klell. *Wasserstoff in der Fahrzeugtechnik*. Vieweg +Teubner, Graz, 2 edition, 2012.

[13] Nadine P. R. Frank. *Umsetzung von Kohlenwasserstoffen in SOFCs*. PhD thesis, Munich University of Technology, 2009.

[14] M. Goswami, R. J.M. Bastiaans, A. A. Konnov, and L. P.H. De Goey. Laminar burning velocity of lean H2-CO mixtures at elevated pressure using the heat flux method. *Int. J. Hydrogen Energy*, 39(3):1485–1498, 2014.

[15] M Grote and C Mengel. Autotherme Reformierung von flüssigen Brennstoffen für den Einsatz in Brennstoffzellenanwendungen. *Chemie Ing. Tech.*, (75):1089–1090, 2003.

[16] Christoph Hochenauer. *Numerische Verfahren in der Energietechnik, Vorlesung*. Lecture notes, Graz University of Technology, 2015.

[17] Christoph Hoßfeld and Rolf Kaiser. Schadensprävention am motornahen Katalysator durch Einsatz der CFD-Simulation. *MTZ*, (04):278–285, 2003.

[18] Stephan Kabelac, Matthias Kind, Holger Martin, Dieter Mewes, Karlheinz Schaber, and Peter Stephan. *VDI-Wärmeatlas*. Springer Berlin Heidelberg, 2013.

[19] Peter Kurzweil. *Brennstoffzellentechnik*. Springer Fachmedien Wiesbaden, Wiesbaden, 2 edition, 2013.

[20] M. L Rightley and F. a. Williams. Structures of CO Diffusion Flames Near Extinction. *Combust. Sci. Technol.*, 125(1-6):181–200, 1997.

[21] Jochen Lehmann and Thomas Luschtinetz. *Wasserstoff und Brennstoffzellen*. Springer Berlin Heidelberg, Esslingen, Stralsund, 2014.

[22] Bettina Lenz. *Untersuchungen zur autothermen Reformierung von Kerosin Jet A-1 zur Versorgung oxidkeramischer Festelektrolyt-Brennstoffzellen (SOFC)*. PhD thesis, Universität Duisburg-Essen, 2011.

[23] N. Peters. *Technische Verbrennung*. Lecture notes, RWTH Aachen, 2010.

[24] Peter Priesching. *Explanation of the Specific Heat and the Meaning of its different Formulations in CFD Calculations*. Avl internal report, AVL List GmbH, 2012.

[25] Wolfgang Sanz. *Computational Fluid Dynamics*. Lecture notes, Graz University of Technology, 2017.

[26] Priyank Saxena and Forman A. Williams. Testing a small detailed chemical-kinetic mechanism for the combustion of hydrogen and carbon monoxide. *Combust. Flame*, 145(1-2):316–323, 2006.

[27] Florian Scharf. *Strömungsmechanische Modellierung eines Brenngaserzeugungssystems*. PhD thesis, Forschungszentrum Jülich GmbH, 2012.

[28] Volkmar Schröder. Explosionsgrenzen von Wasserstoff und Wasserstoff/Methan-Gemischen. Technical report, Bundesanstalt für Materialforschung und -prüfung, 2002.

[29] D Shekhawat, J J Spivey, and D A Berry. *Fuel Cells: Technologies for Fuel Processing*. Elsevier, 2011.

[30] Subhash C. Singhal and Kevin Kendall. *High Temperature Solid Oxide Fuel Cells*. Springer Berlin Heidelberg, 2013.

[31] Marlene Spittel and Thilo Spittel. *Advanced Materials and Technologies Volume 2 Materials Subvolume C Metal Forming Data*. Springer Berlin Heidelberg, 2009.

[32] GmbH VDM Metals. *Aluchrom YHf*. Material data sheet, 2008.

[33] Stefanie Wahl. *Verfahrenstechnische Optimierung und Leistungsskalierung eines Festoxid-Brennstoffzellensystems mit Hilfe multiphysikalischer Modellierung und experimenteller Daten*. PhD thesis, Universität Stuttgart, 2015.

[34] Friedemann Sebastian Winkler. *Mathematical Engineering LRT - Grenzschichten*. Web page (http://me-lrt.de/warme-stoff-transport-grenzschichten-temperatur-geschwindigkeit), 2018.

Appendix

A Calculations

A.1 Matlab Calculation

Stack Simulation

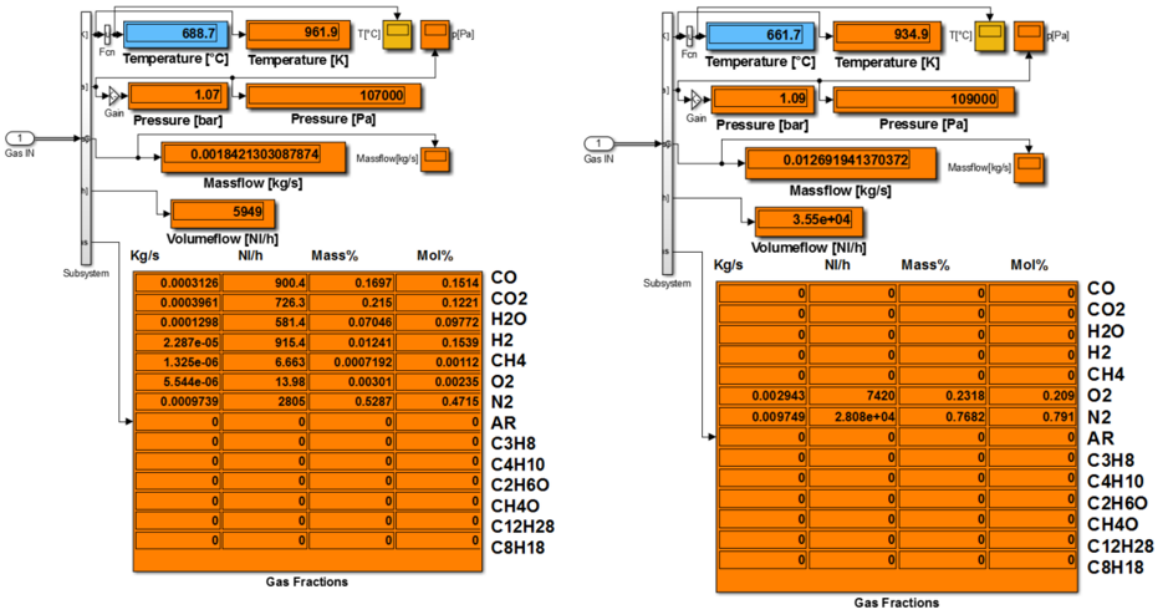

Figure A.1: Input data for stack simulation: anode (left) and cathode (right)

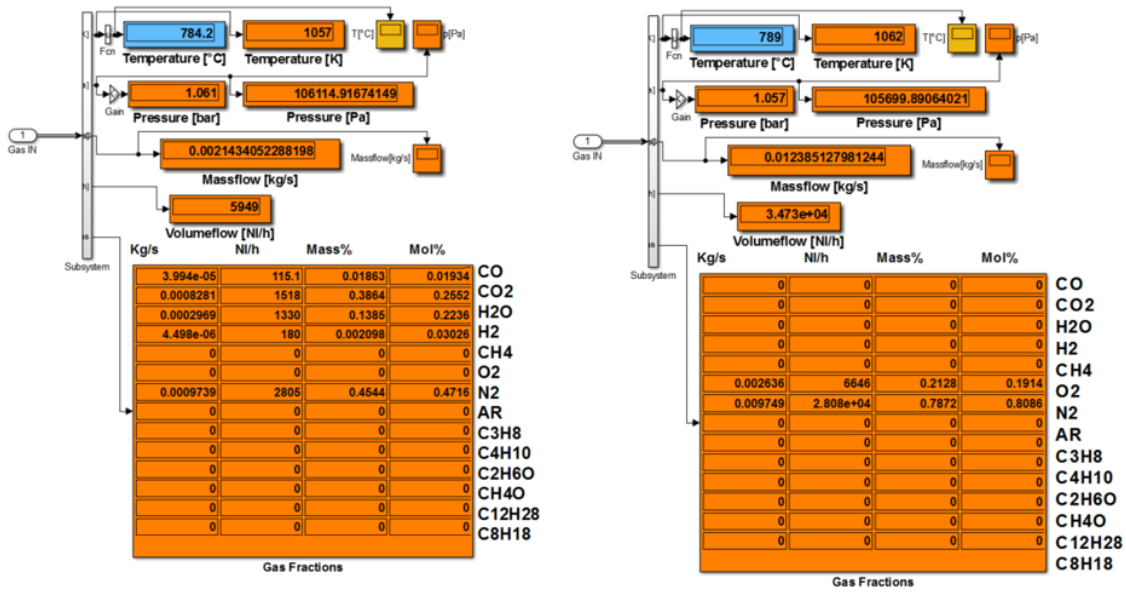

Figure A.2: Output data from stack simulation: anode (left) and cathode (right)

Reformer and Evaporator

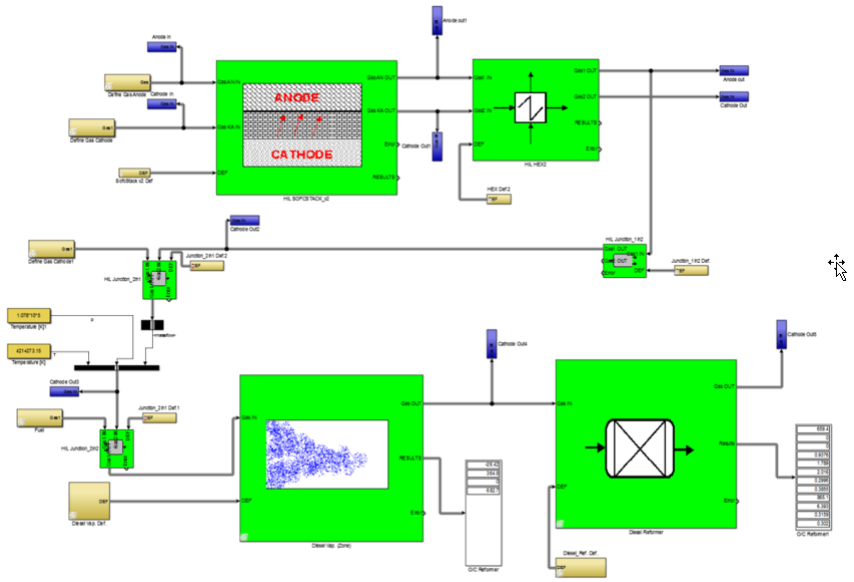

Figure A.3: Overview of stack model with evaporator and reformer module

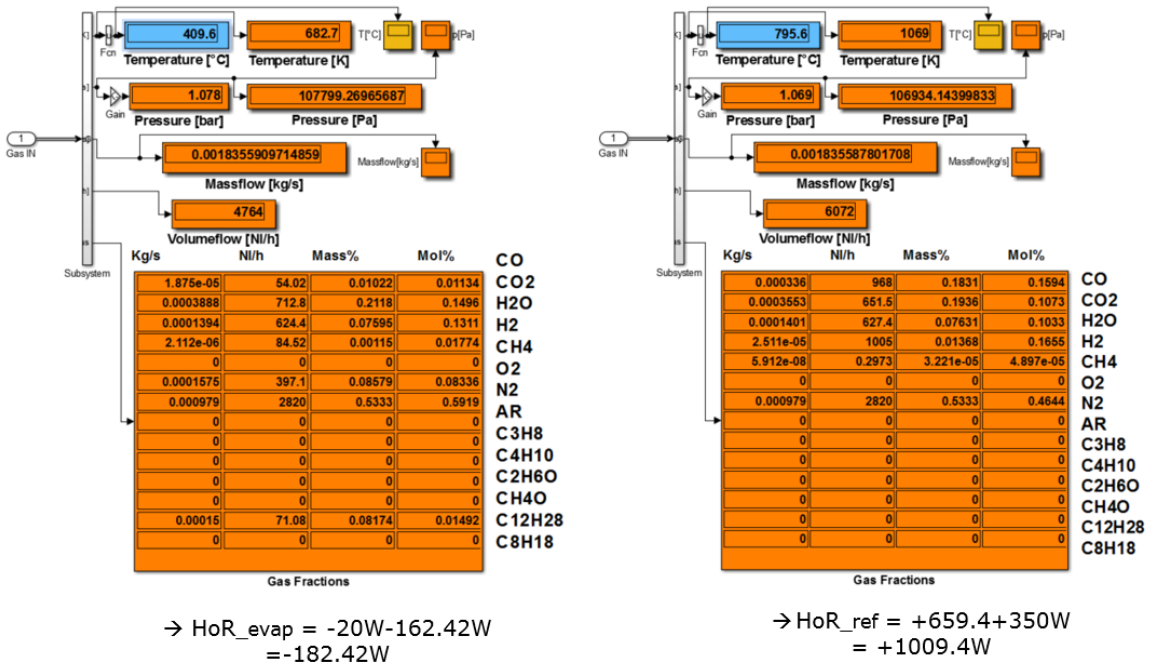

Figure A.4: Output data from evaporator and reformer simulation to use in CFD simulation

Balance calculation for gas composition

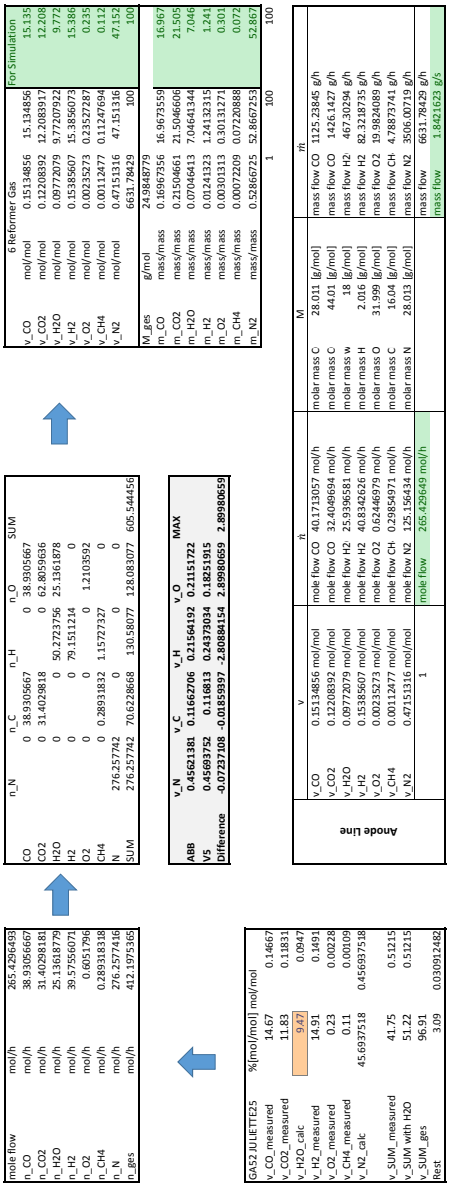

Figure A.5: Calculation of wet gas composition at measuring point after reformer

B Materials and Properties

B.1 Solid Domain

Table A.1: Physical Properties of High Temperature Steel 1.4841 [31]

temperature	**thermal conductivity**	**specific heat capacity at p = const.**	**density**
t	λ	c_p	ρ
°C	W/(m K)	J/(kg K)	kg/m^3
20	11.53	493.31	7520.8
100	13.83	500.10	7483.0
200	17.10	508.73	7442.7
300	18.46	517.50	7405.6
400	19.79	526.43	7367.2
500	21.14	535.51	7318.7
600	22.53	544.74	7274.0
700	23.97	554.14	7227.9
800	25.48	563.69	7180.3
900	27.05	573.42	7131.1
1000	28.70	583.31	7080.2
1100	30.43	593.37	7027.8
1200	32.26	603.60	6973.6

B.2 Catalysts

Reformer Catalyst

Table A.2: Physical Properties of Ceramic Reformer Catalyst used in CFD Investigation

Catalyst Support			**Ceramic**
material			Mg2Al4Si5O18
channel shape			quadratic
diameter	d	mm	60
length	l	mm	35
density	ρ	kg/m³	420
porosity	ε	%	35
cell density	$cpsi$	1/inch²	400
wall thickness	t_{w}	mil	6.5
specific heat capacity at $p = \text{const.}$	c_p	J/(kg K)	1050
thermal conductivity	λ	W/(m K)	4.19
open frontal area	OFA	%	66.4
geometric surface area per catalyst volume	GSA	m²/m³	2566.6
hydraulic diameter	d_{h}	mm	1.1
Washcoat			
material			Al_2O_3
washcoat thickness	δ_{wc}	mm	30-40
Active Component			
precious metal			Rh
catalyst loading	m_{Cat}	g/cm³	0.122

Table A.3: Physical Properties of Mg2Al4Si5O18

temperature	**thermal conductivity**	**specific heat capacity at p = const.**	**density**
t	λ	c_p	ρ
°C	W/(m K)	J/(kg K)	kg/m³
-	4.19	1050	420.0

Oxidation Catalyst

Table A.4: Physical Properties of Oxidation Catalyst used in CFD Investigation

Catalyst Support			**Metallit-S**
material	Nr.	-	1.4767
channel shape			triangular
outer diameter	d_a	mm	127
inner diameter	d_i	mm	64
length	l	mm	35
density	ρ	kg/m³	4160
cell density	$cpsi$	1/inch²	400
wall thickness	t_w	mm	0.05
specific heat capacity at p = const.	c_p	J/(kg K)	table A.5
thermal conductivity	λ	W/(m K)	table A.5
open frontal area	OFA	%	90.33
geometric surface area per catalyst volume	GSA	m²/m³	3025.61
hydraulic diameter	d_h	mm	1.22
Active Component			
precious metal			Pt/Pd [1/1]
catalyst loading	m_{Cat}	g/cm³	0.016

Table A.5: Physical Properties of High Temperature Steel 1.4767 [32]

temperature	**thermal conductivity**	**specific heat capacity at p = const.**	**density**
t	λ	c_p	ρ
°C	W/(m K)	J/(kg K)	kg/m³
30	9.80	490.00	
100	10.90		
200	12.40		
300	13.90		
400	15.50	640.00	
500	16.90		7160
600	18.20		
700	19.70		
800	21.10		
900	22.50		
1000		670.00	

B.3 Heat Exchanger

Table A.6: Physical Properties of Cathode Heat Exchanger used in CFD Investigation

Cathode Heat Exchanger			
material		-	high temperature steel
channel shape			rectangular
area	A	mm²	71 x 167
length	l	mm	71
porosity	ε	%	50
hydraulic diameter	d_h	mm	0.95
pressure drop	Δp	mbar	23 @44.28kg/h

C FIRE Formulas

Enthalpy heat flux

```
double tref = 994.15;
double cpref = 2338.18;
double den, vel[3], temp, cp;
$$init
Bind("ElementData : Flow : Temperature : K", temp);
Bind("ElementData : Flow : Density : kg/m^3", den);
Bind("ElementData : Props : Specific_Heat : J/kgK", cp);
Bind("ElementData : Flow : Velocity.U : m/s", vel[0]);
Bind("ElementData : Flow : Velocity.V : m/s", vel[1]);
Bind("ElementData : Flow : Velocity.W : m/s", vel[2]);
$$formulas
return -den * (vel . n) * (0.5 * (vel . vel) + (temp - tref) * cp);
```

Wall heat flux

```
double heatflux;
$$init
Bind("ElementData : Flow : Convection_Wall_Heatflux : W/m2", heatflux);
$$formula
return |n|* heatflux;
```

Temperature

```
double temp;
double den;
$$init
Bind("ElementData : Flow : Temperature : K", temp);
Bind("ElementData : Flow : Density : kg/m^3", den);
$$formula
divisor += den*|n|;
return den*|n|*temp;
```

General Gas Phase Reaction


```
ELEMENTS
N AR HE H O C
END
SPECIES
N2                AR                HE                H                 O2
OH                O                 H2                H2O               HO2
H2O2              CO                CO2               HCO               CH3
CH4               CH2O              T-CH2             S-CH2             C2H4
CH3O              C2H5              C2H6              CH                C2H2
C2H4OOH           OC2H3OOH          C2H3              CH2CHO            C2H4O
HCCO              CH2CO             C2H               CH2OH             CH3OH
CH3CHO            CH3CO             C2H5OH            CH2CH2OH          CH3CHOH
CH3CH2O           C3H4              C3H3              C3H5              C3H6
C3H8              I-C3H7            N-C3H7            C3H6OOH           OC3H5OOH
C4H10             PC4H9             SC4H9             C4H8              SC4H9O2
C4H8OOH1-3        NC4KET13
END
!
REACTIONS
!
H+O2<=>OH+O                             3.520e+16   -0.700  17069.79
H2+O<=>OH+H                             5.060e+04    2.670   6290.63
H2+OH<=>H2O+H                           1.170e+09    1.300   3635.28
H2O+O<=>2 OH                            7.000e+05    2.330  14548.28
2 H+M<=>H2+M                            1.300e+18   -1.000      0.00
AR/0.50/ H2/2.50/ H2O/12.00/ CO/1.90/ CO2/3.80/
H+OH+M<=>H2O+M                          4.000e+22   -2.000      0.00
AR/0.38/ H2/2.50/ H2O/12.00/ CO/1.90/ CO2/3.80/
2 O+M<=>O2+M                            6.170e+15   -0.500      0.00
AR/0.20/ H2/2.50/ H2O/12.00/ CO/1.90/ CO2/3.80/
H+O+M<=>OH+M                            4.710e+18   -1.000      0.00
AR/0.75/ H2/2.50/ H2O/12.00/ CO/1.90/ CO2/3.80/
H+O2(+M)<=>HO2(+M)                      4.650e+12    0.440      0.00
AR/0.70/ H2/2.50/ H2O/16.00/ CO/1.20/ CO2/2.40/
     LOW  /  5.750e+19   -1.400      0.00 /
     TROE/     0.5    1e-30     1e+30        /
HO2+H<=>2 OH                            7.080e+13    0.000    294.93
HO2+H<=>H2+O2                           1.660e+13    0.000    822.90
HO2+H<=>H2O+O                           3.100e+13    0.000   1720.84
HO2+O<=>OH+O2                           2.000e+13    0.000      0.00
HO2+OH<=>H2O+O2                         2.890e+13    0.000   -497.00
2 OH(+M)<=>H2O2(+M)                     7.400e+13   -0.400      0.00
AR/0.40/ H2/2.00/ H2O/6.00/ H2O2/6.00/ CO/1.50/ CO2/2.00/
     LOW  /  2.300e+18   -0.900      -1697 /
     TROE/    0.57    1e+30     1e-30        /
2 HO2<=>H2O2+O2                         3.020e+12    0.000   1386.00
H2O2+H<=>HO2+H2                         4.790e+13    0.000   7958.90
H2O2+H<=>H2O+OH                         1.000e+13    0.000   3585.09
H2O2+OH<=>H2O+HO2                       7.080e+12    0.000   1434.03
H2O2+O<=>HO2+OH                         9.630e+06    2.000   3991.40
CO+O(+M)<=>CO2(+M)                      1.800e+11    0.000   2384.08
AR/0.70/ H2/2.50/ H2O/12.00/ CO/2.00/ CO2/4.00/
     LOW  /  1.550e+24   -2.790   4190.97 /
     TROE/       1        1     1e+07     1e+07 /
CO+OH<=>CO2+H                           4.400e+06    1.500   -740.92
CO+HO2<=>CO2+OH                         6.000e+13    0.000  22944.55
CO+O2<=>CO2+O                           1.000e+12    0.000  47700.05
HCO+M<=>CO+H+M                          1.860e+17   -1.000  17000.48
H2/1.90/ H2O/12.00/ CO/2.50/ CO2/2.50/
HCO+H<=>CO+H2                           1.000e+14    0.000      0.00
HCO+O<=>CO+OH                           3.000e+13    0.000      0.00
HCO+O<=>CO2+H                           3.000e+13    0.000      0.00
HCO+OH<=>CO+H2O                         5.020e+13    0.000      0.00
HCO+O2<=>CO+HO2                         3.000e+12    0.000      0.00
END
```


Figure A.6: Reaction mechanism in the gas phase for oxidation of H_2 and CO